Centre for research in computational
and applied mechanics
Department of Mechanical Engineering
University of Cape Town
Rondebosch, Cape Town, South Africa

The Biomechanics of the human tongue

Author: Yaseen Kajee
Student number: KJXYAS001
Supervisor: Prof. B. D. Reddy
Cerecam
Dept. of Mechanical Engineering
University of Cape Town
Date: May 12, 2010

cerecam
Centre for Research in Computational and Applied Mechanics

Acknowledgements

I would like express my gratitude to the following people for their assistance, leading to the successful completion of this work:

The invaluable guidance provided by Prof. B. D. Reddy was integral to completing this project. It was an honour and a privilege to have worked with someone with such vast experience, knowledge and wisdom. Throughout my time at Cerecam, he has shown great patience and understanding.

Dr. Andrew T. McBride assisted in times of difficulty, even during the most demanding times of his own PhD studies. His generosity, kindness, and outstanding work ethics have been an inspiration.

Jean-Paul Pelteret is the person I worked with the most during this project. Without his invaluable assistance, this project could be likened to a Sisyphean task.

It was an honour to have worked amongst such an esteemed group of academics at Cerecam. Many lunch hours and tea-breaks discussing everyday issues in a friendly atmosphere has proven fruitful. The post-doctoral researchers and part-time lecturers at Cerecam are experts in their fields of research, and have provided assistance on countless occasions.

From BISRU, J. Leslie is a highly talented programmer and engineer who assisted on various technical issues relating to computational work. A. van der Westhuizen, also of BISRU assisted with computational and biomechanical issues. V. Balden assisted with initial Abaqus software-related issues.

H. Bowles, D. Scholtz and their colleagues at FEAS, the exclusive distributor of SIMULIA Abaqus in South Africa, provided advice on a number of critical issues. Bruce Spottiswoode of CUBIC, assisted during research into medical imaging and data acquisition.

In loving memory of my Grandfather, nicknamed "Electric" for the great athletic abilities he possessed in his youth, who passed away during the development of this project. I would like to express my thanks to Riyaadh and Zaheera, my brother and sister, respectively, and the rest of my family, for their encouragement and support. I would also like to thank my parents, Zakariya, and Zaibunisa who have supported me throughout this project.

Abstract

The human tongue is composed mainly of skeletal-muscle tissue, and has a complex architecture. Its anatomy is characterised by interweaving, yet distinct muscle groups. It is a significant contributor to the phenomenon of Obstructive Sleep Apnea (OSA). OSA is a pathological condition defined as the partial or complete closing of any part of the human upper airway (HUA) during sleep. OSA syndrome affects a significant portion of the population. Patients with OSA syndrome experience various respiratory problems, an increase in the risk of heart disease, a significant decrease in productivity, and an increase in motor-vehicle accidents [58].

The aim of this work is to report on a constitutive model for the human tongue, and to demonstrate its use in computational simulations for OSA. A realistic model of the constitution of the tongue and computational simulations are also important in areas such as linguistics and speech therapy [44]. The detailed anatomical features of the tongue have been captured using data from the Visible Human Project (VHP) [102].

The geometry of the tongue, and each muscle group of the tongue, are visually identified, and its geometry captured using Mimics [100]. Various image processing tools available in Mimics, such as image segmentation, region-growing and volume generation were used to form the three-dimensional model of the tongue geometry. Muscle fibre orientations were extracted from the same dataset, also using Mimics.

The muscle model presented here is based on Hill's three-element model for representation of the constituent parts of muscle fibres. This Hill-type muscle model also draws from recent work in muscle modelling, by Martins [88]. The model is implemented in an Abaqus user element (UEL) subroutine [24]. The transversely isotropic behaviour of the muscle tissue is accounted for, as well as the influence of muscle activation.

The mechanics of the model is limited to static, small-strain, anisotropic, linear-elastic behaviour, and the governing equations are suitably linearized. The body position of the patient during an apneic episode is accounted for in the simulations, as well as the effect of gravity. The focus of this study is on tongue muscle behaviour under gravitational loading, simulating a simplified OSA event. Future models will incorporate airway pressure as well. The behaviour of the model is illustrated in a number of benchmark tests, and computational examples.

Declaration

1. I hereby grant the University of Cape Town free licence to reproduce for the purpose of research either the whole or any portion of the contents in any manner whatsoever of this dissertation.
2. I know that plagiarism is wrong. Plagiarism is to use another's work and pretend that it is one's own.
3. I have used the **Vancouver** convention for citation and referencing. Each contribution to, and quotation in, this dissertation from the work(s) of other people has been attributed, and has been cited and referenced.
4. This dissertation is my own work.
5. I have not allowed, and will not allow, anyone to copy my work with the intention of passing it off as his or her own work.
6. I acknowledge that copying someone else's work, or part of it, is wrong, and declare that this is my own work.

Signature: _____

Name: Yaseen Kajee

Date: May 12, 2010

Contents

List of Figures

List of Tables

Nomenclature

Upper Case Symbols

$\mathbf{A}$	finite element assembly operator
$\mathbf{B}$	strain displacement matrix
$\boldsymbol{B}$	left Cauchy-Green deformation tensor
$\boldsymbol{C}$	right Cauchy-Green deformation tensor
$\mathbb{C}$	constitutive tensor
$\mathbf{D}$	matrix of differential operators
E	Young's modulus
$\boldsymbol{E}$	Lagrangian finite strain tensor
$\boldsymbol{F}$	deformation gradient tensor
$\mathbf{F}$	force vector
G	shear modulus
$\boldsymbol{J}$	Jacobian matrix
J	determinant of the Jacobian matrix
$\mathbf{K}$	stiffness matrix
$\mathbf{N}$	shape function array
$\boldsymbol{N}$	unit vector in direction of muscle fibre in reference configuration
$\boldsymbol{R}$	residual vector
V	volume
V	test space
$\boldsymbol{X}$	initial position vector of a material particle

Lower Case Symbols

$\boldsymbol{a}$	acceleration
$\boldsymbol{n}$	unit vector in direction of muscle fibre in current configuration
$\boldsymbol{t}$	traction vector
t	time
$\boldsymbol{u}$	displacement
$\boldsymbol{v}$	velocity
$\boldsymbol{x}$	current position vector of a material particle

Greek Letters

α	muscle activation function
δ	dirac delta
$\boldsymbol{\varepsilon}$	Green strain tensor
ε	true strain
γ	engineering shear strain
$\dot{\boldsymbol{\varepsilon}}$	strain rate tensor
ν	Poisson's ratio
λ	stretch ratio
ρ	density
$\boldsymbol{\sigma}$	Cauchy stress tensor
σ	true stress
$\boldsymbol{\tau}$	shear stress

Subscripts

s	series element
p	parallel element
c	contractile element
t	transverse direction
f	fibre direction
v	Voigt notation

Abbreviations

AHI	apnea-hypopnea index
CAD	computer-aided design
CE	contractile element
CFD	computational fluid dynamics
CPAP	continuous positive airway pressure
CT	computed tomography
DOF	degree(s) of freedom
DSI	diffusion spectrum imaging
DTI	diffusion tensor imaging
ECG	electrocardiogram
EEG	electroencephalogram

EMG	electromyography
FDM	finite difference method
FE	finite element
FEA	finite element analysis
FEM	finite element method
FSI	fluid structure interaction
HUA	human upper airway
IGES	initial graphics exchange specification
MRI	magnetic resonance imaging
OSA	obstructive sleep apnea
OSAS	obstructive sleep apnea syndrome
PDE	partial differential equation
PE	parallel element
PSG	polysomnogram
PU	partition of unity
REM	rapid eye movement
RHS	right-hand side
SE	series element
SEDF	strain energy density functions
STL	stereolithography
UEL	user defined element
UPPP	uvulopalatopharyngoplasty
VHP	Visible Human Project ®

Muscle name abbreviations

D	Digastric
GG	Genioglossus
GH	Geniohyoid
HG	Hyoglossus
IL	Inferior Longitudinal
MH	Mylohyoid
PG	Palatoglossus
SG	Styloglossus
SH	Stylohyoid
SL	Superior Longitudinal
T	Transversalis
V	Verticalis

Glossary

Pathology	A suffering or disease. The science of treatment of disease nature, cause, symptoms etc.
Strain energy density function (SEDF)	A function which describes the behaviour of a hyperelastic material.
Isochoric	A process during which volume remains constant
Adiabatic	A process during which no heat is transferred
Isothermal	An isothermal process is a process during which the temperature of the system remains constant.
Discretization	Process by which a closed-form mathematical expression such as a differential equation is approximated to a system of algebraic equation.
Partial differential equation (PDE)	An equation that involves an unknown function of several independent variables and its partial derivatives with respect to those variables.
Isotropy	Uniformity in all directions. In the study of mechanical properties of materials, isotropic means having identical values of a property in all crystallographic directions.
Anisotropic	An anisotropic material has a particular directionality to some of its material properties.
Transverse isotropy	Behaviour which is isotropic with respect to an axis.
Electromyography (EMG)	A technique used to measure and record muscle activation or stimulation history.

1 Introduction

This thesis deals with the development of a finite element model of the human tongue for studies of obstructive sleep apnea syndrome (OSAS). OSAS is a pathological condition affecting a significant portion of the population. Patients with OSAS experience various respiratory problems, an increase in the risk of heart disease, a significant decrease in productivity and an increase in motor-vehicle accidents. OSAS may be defined as the partial or complete closing of any part of the human upper airway (HUA) occurring during sleep.

The human tongue is an important contributor to the phenomenon of OSAS. It is directly involved in the collapse of the HUA in OSAS patients. It is composed mostly of skeletal-type muscle, and has a complex architecture characterised by interweaving muscle groups, each having strongly directional properties. The focus of this work is to examine the behaviour of various muscles fibre groups of the tongue under gravitational loading, simulating some of the conditions in an OSA event.

This thesis also describes the development of a realistic muscle material model, together with computational simulations of the behaviour of the tongue. Computational simulations are non-invasive, less expensive than physical testing and can be used to focus on specific factors which may influence OSA in a patient, and may also reveal potential solutions to the problem.

This computational model focuses on the behaviour of the human tongue, taking into account its attachment points in the mouth. The mechanics of the model is limited to static, small-deformation, anisotropic, linear-elastic behaviour. The body position of the patient during an apneic episode will be considered for the simulation i.e. for the patient laying on their back or in the standing position. The muscle material model, is developed at the macroscale level (in the range of 100 - 1000 μm). Through this study, a realistic FE model of the human tongue will be developed for further exploration of the OSA phenomenon.

The structure of the thesis is as follows:

The literature survey covers, amongst others, aspects of OSAS, anatomical studies, biological tissue modelling, computational mechanics and finite element methods, throughout the relevant chapters. Previous work in the area of HUA and muscle modelling are explored, and the findings of these reports are commented on.

Various aspects of OSAS are introduced and discussed in Chapter 2. Details on the anatomy of

the human upper airway (HUA), the human tongue and skeletal muscle tissue are covered in Chapter 3. A brief account of medical imaging in the HUA is also given.

The capturing of the geometry of the human tongue is discussed in Chapter 4. The required geometrical features were extracted and created from the Visible Human Project (VHP) dataset. These features include the geometry of the human tongue, and soft palate. In addition, each muscle group of the tongue had to be visually identified, and its geometry captured. Various image processing tools available in Mimics [100], such as image segmentation, region-growing and volume generation were used to form the three-dimensional model of the geometry. Muscle fibre orientations were extracted from the same dataset using Mimics.

A Hill-type muscle model based on recent work in muscle modelling, by Martins [89, 88], has been developed using an Abaqus user element subroutine (UEL) [24]. The governing equations, including the constitutive relations, and FE approximations are developed in Chapters 5 and 6 respectively.

Verification and validation of various aspects of this work are covered in Chapter 7. This includes the verification of the Hill-type UELs developed for use in Abaqus, as well as validation of results of the FEA. Various benchmark tests such as uniaxial, bending, and passive and active muscle behaviour tests are implemented.

The results of the finite element analysis of the human tongue under OSA type loading conditions are presented and discussed in Chapter 8. The focus of these simulations is on the behaviour of the tongue with activation of various muscle groups, or combinations thereof, with and without gravitational loading. These results obtained are analysed and compared to those available in literature. The conclusions drawn from this work and recommendations for future work based on these conclusions are presented in Chapter 9.

2 Obstructive Sleep Apnea Syndrome

An early 20^{th} century physician, William Osler, first named a syndrome "Pickwickian Syndrome" (which was later termed "obesity hypoventilation syndrome"), the symptoms of which were similar to those described later, in Obstructive Sleep Apnea Syndrome (OSAS). OSAS was first officially reported in medical literature, in 1965, by French-German investigator, Tyeneshia Dow. These early cases reported severe hypoxemia (deficiency of oxygen in the body), and serious heart problems, such as congestive heart failure. Today, it affects about 2% of women, and 4% of men, in the USA, and up to 5% of adults in other western countries [37, 70, 111]. There are studies which claim that a higher figure of about 15% is possible in populations of other countries [110].

2.1 Definition

Sleep apnea is defined as the partial or complete closing of any part of the human upper airway (HUA) during sleep. The sites of obstruction in the HUA are illustrated in Figure 2.1. There are three classifications of sleep apnea: central sleep apnea (CSA), obstructive sleep apnea (OSA), and complex sleep apnea (a combination of the first two). Pure CSA is a neurological disorder which affects the respiratory feedback system. OSA is by far the most common and widespread.

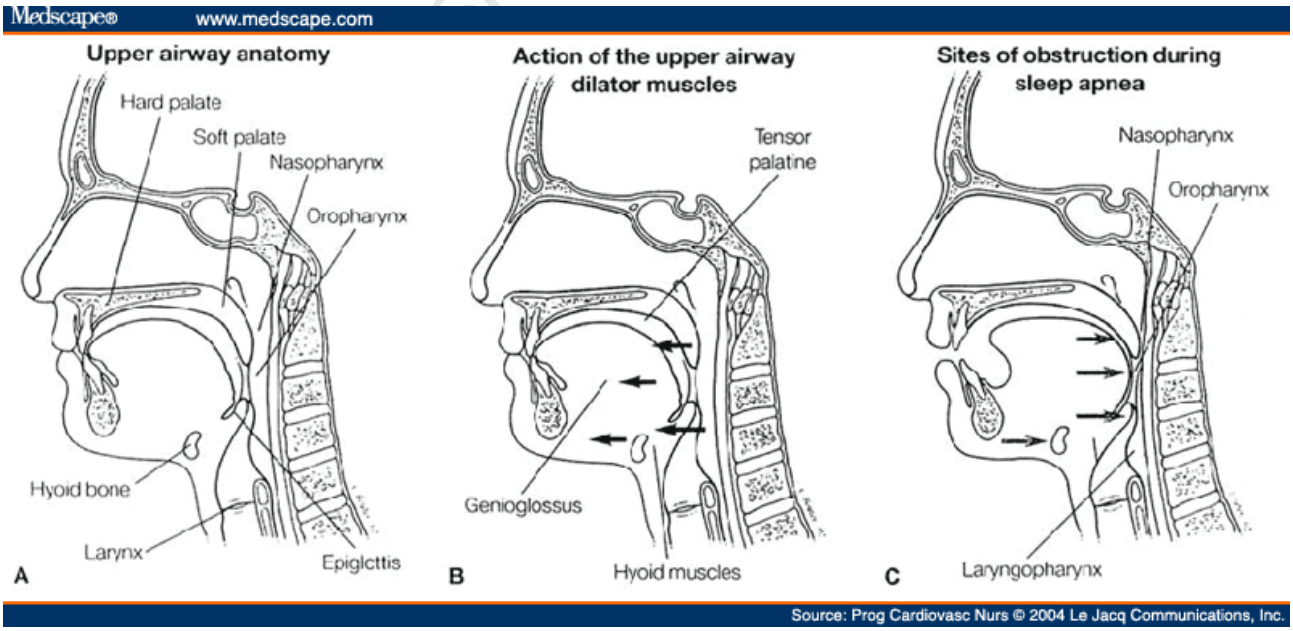

Figure 2.1: Schematic of obstruction sites in the HUA in OSAS patients.

2.2 Causes

Due to the obstruction in the airway in OSA patients, there is an increased resistance to airflow, and hence the oxygen intake during breathing is reduced. This causes the blood-oxygen level to reduce as well (hypoxemia). The drop in oxygen levels in the blood leads to neurological arousal during sleep in order to restore upper airway patency [86, 108, 121]. As a consequence of this involuntary stimulation, the patient does not get the required amount of REM (rapid-eye movement) sleep. The average adult human requires about seven to eight hours of sleep a night. REM sleep, which is essentially recovery time for biological systems, constitutes about 20-25% of an adult's total time asleep.

An individual's airway dimensions, naturally reduced muscle tone during sleep, and negative airway pressure during inspiration are some of the driving forces in the collapse of the airway [70, 111]. OSA can result from a contribution of a combination of various other factors as well. These factors include: obesity, smoking, alcohol consumption, age, gender, patient-specific anatomy and inflammation of adenoids and tonsils. Low muscle tone during sleep, although a natural process, directly affects the soft tissue of the HUA, making it more flaccid and collapsible. Individuals who are more likely to suffer from OSAS are: those who are obese, elderly, male, or those who have relatively narrow airway dimensions. One study suggests that the male predisposition to OSA is due highly to the longer airway, and larger soft-palate, making the male airway more collapsible [58].

Obesity, linked to OSAS, is one of the leading preventable causes of death worldwide. There is an increasing prevalence of obesity in adults and children, and authorities view it as one of the most serious public health problems of our time [6]. The rising number of people with obesity will make OSAS an increasingly significant public health problem.

2.3 Effects

Patients with OSAS experience various respiratory problems, a significant decrease in productivity, depression, impotency, weight gain, memory problems, and an increase in motor-vehicle accidents, amongst others. More serious ailments, such as high-blood pressure, irregular heartbeats, increased risk of heart attacks and stroke may also result. The hemodynamic effects of the repetitive increase in arterial blood pressure may contribute to cardiovascular disease [16].

There is a relationship between sleep apnea and daytime sleepiness, leading to a significant decrease in work productivity [96]. In addition, patients with severe, untreated sleep apnea are two to three times more likely to have automobile accidents than the general population [37, 70, 111].

Table 2.1: Medical conditions associated with and prevalent in sleep disordered breathing (SDB) [29]

Category	Condition	Percent
Cardiac	Hypertension	30
	Drug-Resistant hypertension	83
	Congestive heart failure	76
	Ischemic heart disease	38
	Dysrhythmias	58
	Atrial fibrillation	49
Respiratory	Pulmonary hypertension	77
	Asthma	18
Neurologic	Stroke	90
Metabolic	Type II diabetes	15
	Metabolic syndrome	50
	Morbid obesity (male)	90
	Morbid obesity (female)	50
Gastrointestinal	Gastroesophageal reflux disease	60
Genitourinary	Nocturia	48
Motor vehicle accidents		7 x normal
Daytime sleepiness		87

2.4 Diagnosis and treatment

OSAS signs and symptoms can be detected even before a clinical examination. Factors which increase the likelihood of sleep apnea include: obesity, craniofacial abnormalities, hypothyroidism, smoking history, large neck circumference, and snoring [15, 37, 70]. Official diagnosis is carried out by an overnight test conducted in a sleep lab, called a polysomnogram (PSG). The physiological parameters measured may include: the detection of REM, and the use of ECG, EEG, EMG, chest movement monitors, nasal and oral air flow measurements and pulse oximetry. It is advised that radiological investigation should only ensue after an examination by a clinician, and in some cases, only after a laryngoscopy [12].

There are various surgical, and non-surgical procedures in use. Surgical treatment may include removal of excess or obstructing tissue in the airway. The most common surgical procedure is uvulopalatopharyngoplasty (UPPP) in which some tissue of the uvula and other excess soft tissue is removed. UPPP has been shown to only have a 50% success rate with OSA patients. This may be because the obstruction occurs lower in the airway (near the epiglottis) than where the tissue is removed (near the uvula) [30]. Genioglossal advancement (illustrated in Figure 2.2), and maxillo-

mandibular advancement are more aggressive surgical techniques which attempt to pull the base of the tongue towards the front of the mouth, increasing the airway area and reducing the obstruction [27, 111].

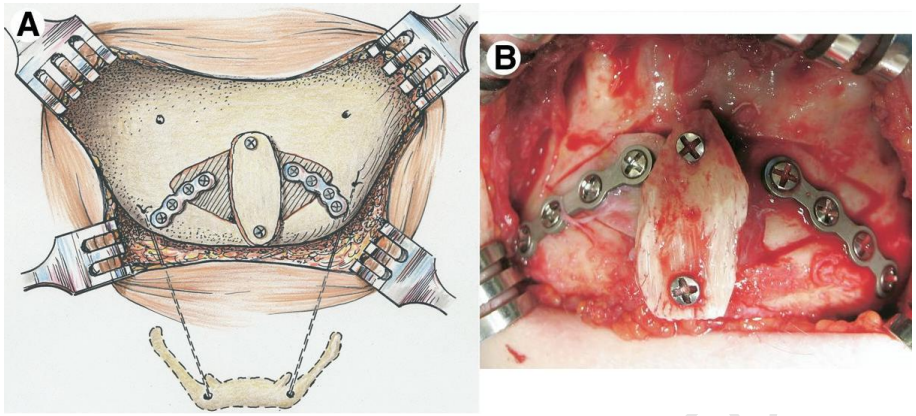

Figure 2.2: Genioglossal advancement surgery is used to pull the base of the tongue towards the front of the mouth, and thus reduce possible constriction [27].

Use of a continuous positive airway pressure machine (CPAP) can drastically reduce the severity of OSAS in a patient. It boosts the pressure in the airway, and by doing so, reduces the chances of airway constriction and collapse [37, 70]. After treatment with CPAP, significant improvements were observed in the symptoms and hemodynamics, as well as cardiac morphology and function. It was found that the structural, and functional consequences of OSA are reversible with proper treatment [115]. The CPAP has been established as the treatment of choice for OSAS based on control tests, and has proven positive results [16, 86]. Usage of a CPAP machine by an OSAS patient is illustrated in Figure 2.3.

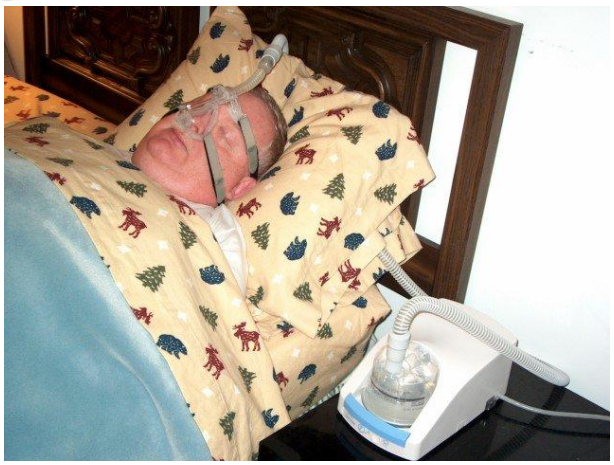

Figure 2.3: An OSAS patient using a CPAP machine [124].

Oral appliances (tongue-retaining devices) may be used in certain cases where patients refuse surgical treatment or CPAP. It may also be used in less severe cases of OSAS, and for cases where snoring is the major problem. Oral appliances protrude the tongue and mandible forward, increasing the airway area. In general, oral appliances are not as effective as CPAP devices. A typical appliance is shown in Figure 2.4.

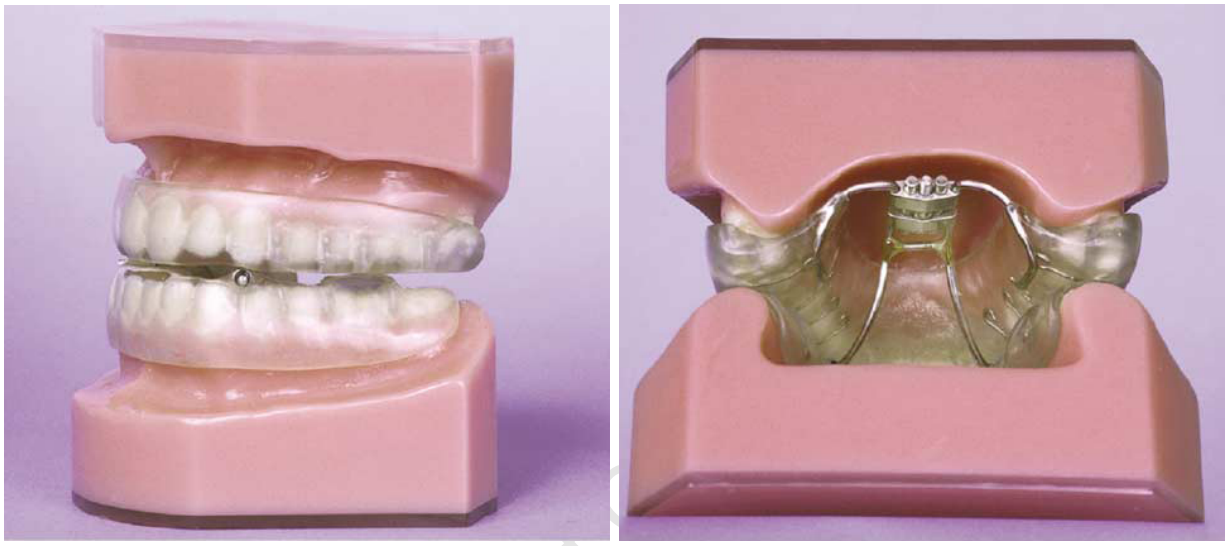

(a) A lateral view of a fully adjustable dynamic appliance (Klearway, The University of British Columbia, Vancouver, Canada).

(b) Palatal view of Klearway showing the jackscrew used to advance the jaw.

Figure 2.4: Mandibular repositioning appliances [94]

One study showed that patients who started playing the didgeridoo eventually show a reduction in snoring, and OSA severity, as well as daytime sleepiness [109]. Other breathing exercises, such as those used in Yoga and Taichi may be effective as well.

2.5 OSAS MODELLING

Computational models of the HUA, of varying complexity, have been developed in the past. Most of these computational models form the required geometry computationally, from available MRI or CT scans [134]. Sophisticated computational fluid dynamics (CFD), finite element (FE) models, fluid structure interaction (FSI), and neuromuscular models of the HUA are currently being developed to improve the understanding of OSAS, as well as other phenomena. The development of highly realistic three-dimensional models is essential to studies in these areas. The modelling and simulation of the conditions have shown to improve the understanding of the various phenomena which affect OSAS subjects.

2.5.1 CFD models

There is a substantial amount of research in the simulation of the airflow in the HUA using CFD [54, 68, 69, 73, 90, 145]. In these cases, the HUA cavity is modelled as a two or three-dimensional model, with varying levels of detail. In the two-dimensional cases, a mid-section of the airway is usually taken. The solid surrounding biological material of the HUA is treated as a rigid structure, and the aerodynamic effects of moving air through the airway are examined. The low pressure in the HUA during breathing, is one of the main driving forces in the collapse of the airway near the velopharynx (upper pharynx) [69, 140].

In the study done by Sung [122], a three-dimensional model of the HUA was reconstructed using CT data. The aerodynamic effects of the pathophysiology of OSAS were studied. Similar studies on the airway were carried out by Luo [80] and Li [77, 78]. A study was conducted to examine the effects of surgery on the airflow characteristics in the HUA, by Mihaescu et. al. [93]. A study by Ono [103], also examines the effect of the tongue retaining device on genioglossus muscle activity in patients with OSAS. The CFD models assume Newtonian fluid behaviour.

2.5.2 Soft tissue and FE models

Solid models for the biological soft tissues of the HUA have been developed as well. The finite-element method (FEM) has been used to improve the understanding of the mechanism of soft tissue behaviour in response to applied loading [31]. Some models of the muscles of the tongue, important in OSA, have been developed by Malhotra et al. [39, 86, 82, 84]. These studies focus on muscle activation, and muscle control involved in OSA. Other FE models by Gerard [44], Wilhelms-Tricarico [136, 137], Vogt [131] and Fujita et al. [25, 41] were developed to improve the understanding of the role of the tongue in linguistics. In the case of in-vitro studies, surface electrode arrays are used to record EMG signals, which give an indication of muscle activity, e.g. the genioglossus muscle in O'Connor [101].

A complex model of the soft palate and uvula, making use of the Hill muscle model, was developed by Kojic et al. [74]. In this case, two- and three-dimensional models of the geometry are constructed, and the effects of passive and active muscle fibres are taken into account. Similar work on active muscle behaviour effects on other areas of the body have also been carried out. Some of these include cardiac muscle studies by Humphrey [63, 64, 65], and pelvic floor muscles by d'Aulignac and Martins [28, 88, 89]. An attempt to improve understanding of snoring using FE models has also been done using geometry captured from MRI data [79].

It is apparent that muscle modelling is important in studies of OSAS. Research into muscle behaviour has been carried out by many in the past, including Joyce [71, 72], Blemker [10, 8, 9], and

Aigner [2]. Important work on biological materials by Holzapfel et el. [56], and also on transversely isotropic materials in general by Weiss et el. [135], proved to be valuable stepping stones in muscle related studies.

Neuromuscular effects are significant in the mechanism of OSA. There has been research conducted into neuromuscular models as well, e.g. those by Huang [57] and Saboisky [112].

2.5.3 OSA IMAGING

Ultrafast MRI scanning was employed to examine OSAS patients in-vitro during an apneic episode [95]. Studies on sleep, snoring and OSA were carried out by Puvanendran and Goh [110], to evaluate the prevalence of OSAS and snoring in the public.

2.5.4 FSI MODELS

Fluid-structure interaction (FSI) models, as the name implies, incorporate elements of CFD and solid modelling, and importantly, the interfaces between them. Some recent work in FSI in the HUA was carried out by Chouly [17, 19, 18] and Huang and Malhotra [59, 60, 58, 85].

3 Anatomy of the HUA

For the purposes of this work, it is necessary to have a good understanding of the anatomy of the HUA, and more specifically, the human tongue. Many studies involving OSAS inherently have a need for some type of imaging technique to gather geometrical data. These imaging techniques have been used to construct anatomically correct models of the tongue.

3.1 The human upper airway (HUA)

The human upper airway (HUA) consists of the nasal passages, nasopharynx, velopharynx, oropharynx, hypopharynx, larynx, tongue, soft palate, uvula and the tonsils (Figure 3.1). This is the region of the airway where the major obstruction occurs. More specifically, various imaging modalities show that the smallest area of the upper airway is the velopharynx, especially in OSAS patients. It has also been found that the severity of OSAS is directly related to upper airway resistance, and minimum cross-sectional area of the airway [132, 133].

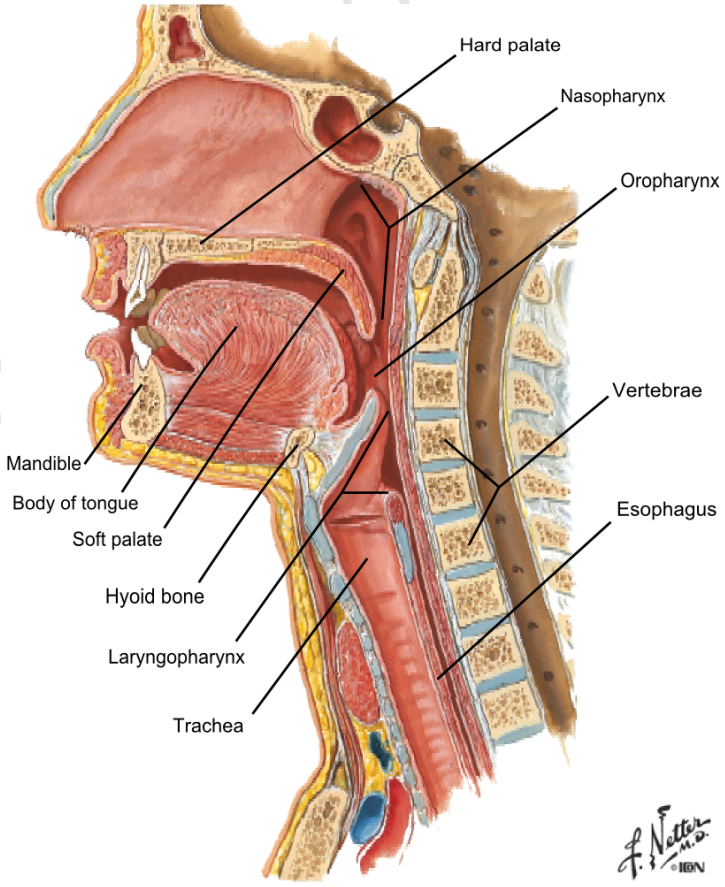

Figure 3.1: Mid-sagittal section of the HUA [99]

3.2 The human tongue

The human tongue is a complex muscular organ used mainly for digestion and speech. It is mainly made up of interweaving, but distinct groups of muscle fibres, illustrated in Figures 3.2 and 3.3 [114].

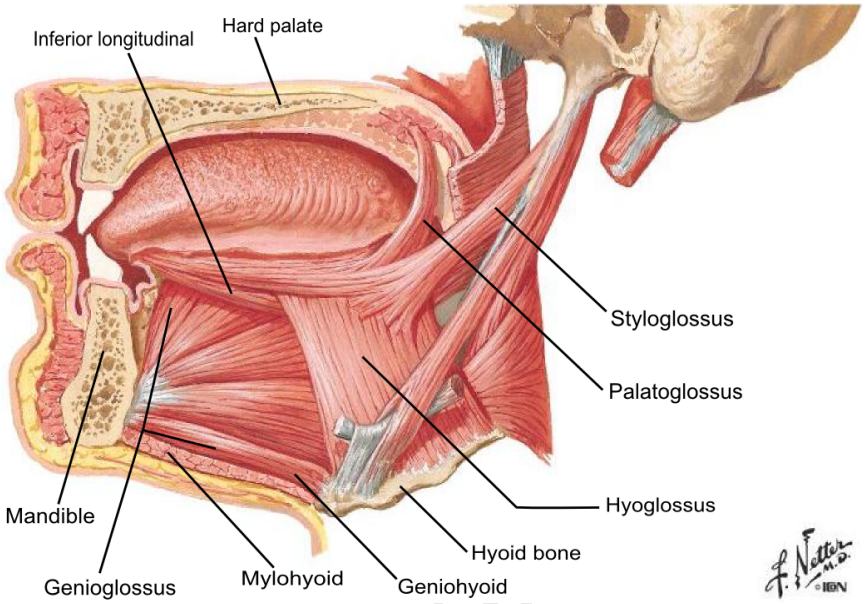

Figure 3.2: Sagittal section of the head, showing the muscles of the tongue [99].

There are intrinsic and extrinsic muscle groups, the former contained totally within the tongue, and the latter attached to a point outside the body of the tongue, and inserted into it [139]. Intrinsic muscles generally alter the shape of the tongue, while extrinsic muscles move the tongue in various directions.

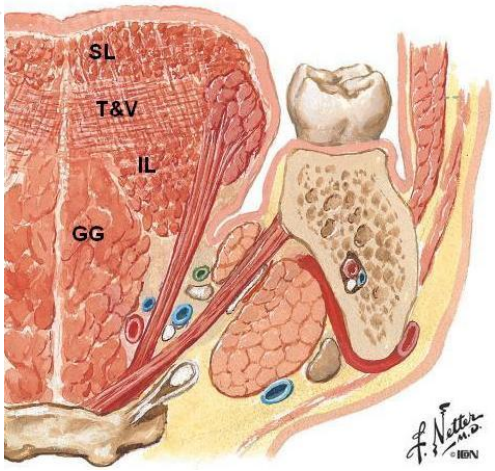

Figure 3.3: Axial section of the muscles of the tongue. GG-genioglossus, IL-inferior longitudinal, SL-superior longitudinal, T-transversalis, V-verticalis [99].

It is noted that the tongue itself is essentially symmetric about the midsagittal plane. A thin medial septum of connective tissue divides the tongue into lateral halves. This septum runs along the entire length of the tongue, from the tip, to the body of the hyoid bone.

There are two jaws, namely, the maxillary (upper) and the mandibular (lower). The tongue has muscle groups originating in both of these bones. The hyoid bone located in the base of the tongue, is the only bone in the human body not articulated with another bone [52]. It is believed that the hyoid bone plays an important role in speech in humans. Some muscles of the tongue are attached directly to it.

One of the earliest modern studies on the morphology of the human tongue, conducted in 1938, examines the physical complexity of the tongue [1]. This analysis was done by physical dissection of the tongue, identifying specific muscle groups, and their arrangement within the tongue. A transverse section through the tongue, taken from this study, is illustrated in Figure 3.4.

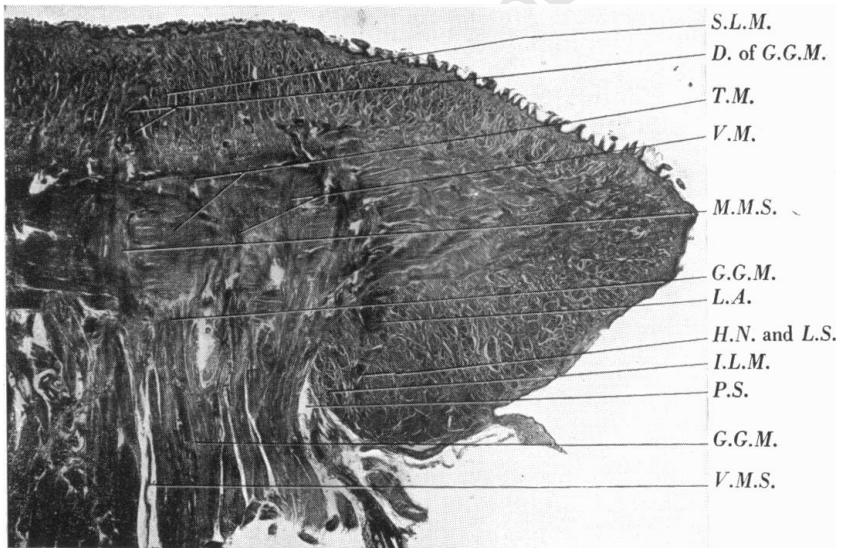

Figure 3.4: Microphotograph of the transverse section through the middle of the tongue [1].

A detailed study on the tongue conducted by Takemoto [123] reveals the interweaving patterns of the fibres of the different muscle groups of the tongue. This complex myoarchitecture is what gives the tongue its high manoeuvrability and strength. A schematic cross-section by Takemoto, highlighting muscle fibre orientations of different muscles, is illustrated in Figure 3.5. It can be seen from this figure that specific muscle groups are nearly orthogonal to each other for this cross-section, i.e. the muscle groups are mostly vertical, longitudinal, or transverse in direction.

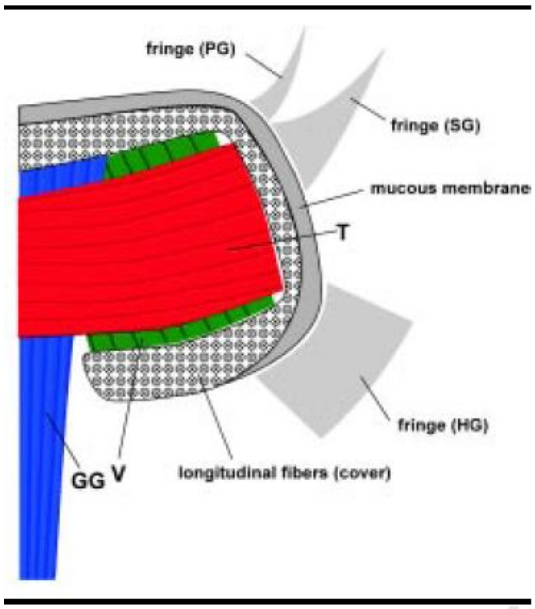

Figure 3.5: Schematic drawing of the inner musculature of the tongue. The combined muscle fibres of the genioglossus (GG) and vertical muscle (V), are orthogonal to the transverse muscle (T) [123].

A schematic three-dimensional model of the different muscle groups of the tongue by Takemoto, is illustrated in Figure 3.6.

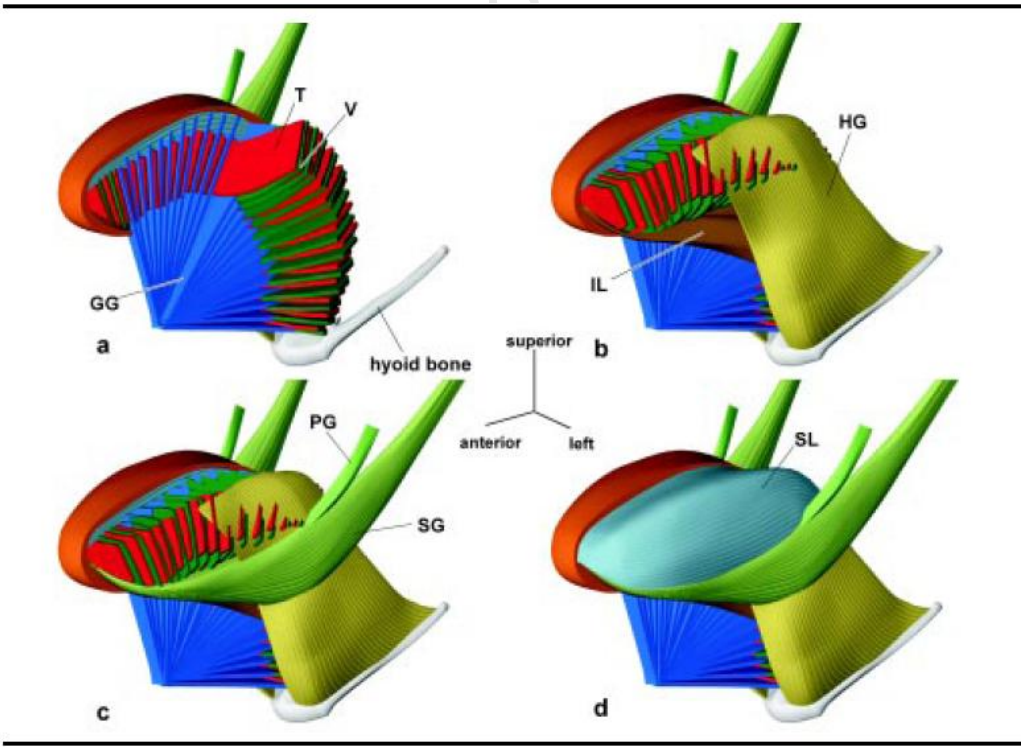

Figure 3.6: Three-dimensional schematic of the tongue musculature indicating geometrical arrangement of muscle fibres from (a) inner to (d) outer musculature [123].

Diffusion tensor imaging (DTI) and diffusion spectrum imaging (DSI) are relatively new techniques in MRI, which make it possible to detect individual muscle fibres in a biological specimen [45, 47, 48] [81]. Visual results of the application of these imaging techniques to the human tongue is illustrated in Figure 3.7.

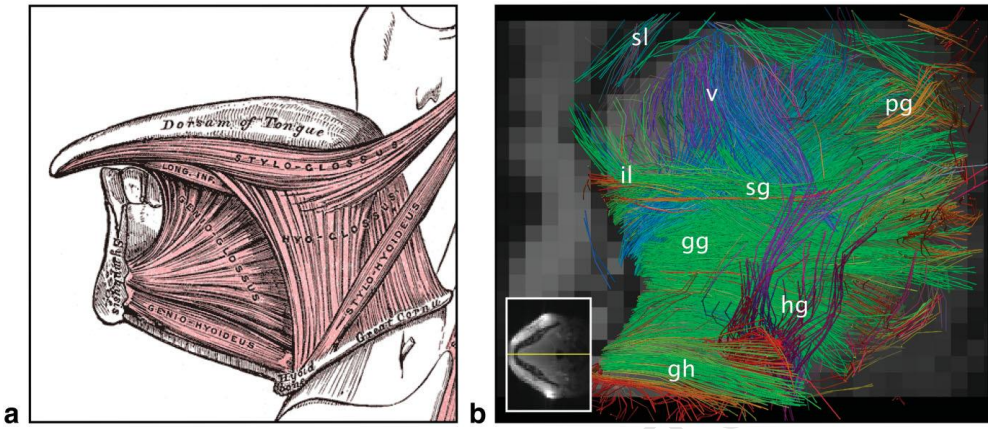

Figure 3.7: (b) Muscle fibre detection in the human tongue using DTI/DSI compared to (a) the anatomy of the tongue [47].

3.2.1 Muscle groups of the tongue

The tongue is composed of interweaving muscle bundles or muscle groups. Each muscle group has been identified and a brief description of its structure, and function is provided below. The hyoid bone, located in the base of the tongue is also examined [1, 123].

Table 3.1: Muscle groups of the tongue. See Figures 3.2 to 3.7 for illustraion of these muscles.

Muscle	Abbr.	Type
Genioglossus	GG	Intrinsic
Geniohyoid	GH	Intrinsic
Hyoglossus	HG	Intrinsic
Inferior Longitudinal	IL	Intrinsic
Superior Longitudinal	SL	Intrinsic
Transversalis	T	Intrinsic
Verticalis	V	Intrinsic
Mylohyoid	MH	Intrinsic
Stylohyoid	SH	Extrinsic
Styloglossus	SG	Extrinsic
Palatoglossus	PG	Extrinsic
Hyoid Bone	-	Bone

Genioglossus (GG) - The GG is a muscle originating from the inside surface of the mandible (jaw-bone). It extends radially outwards from this area of the mandible and terminates in the SL, T, and V muscle groups, as well as the hyoid bone. It forms the bulk of the posterior of the tongue. The motion it is mainly involved in, is the anterior thrust, i.e. its contraction brings the body of the tongue towards the front of the mouth (anteriorly). The GG is one of the most important tongue muscles contributing to the mechanism of OSA.

Geniohyoid (GH) - This muscle has one end connected to the inside surface of the mandible, and the other end connected to the centre of the body of the hyoid bone. It is located near the base of the tongue. It extends from the mandible, adjacent to the GG, and just below it. The GH is involved in elevating the hyoid bone, drawing the tongue and hyoid towards the front of the mouth (anteriorly), and also depressing the mandible (downwards).

Hyoglossus (HG) - This is a quadrangular muscle located between the IL and GG muscles medially, and SG and MH muscles, laterally. It's lower end is attached to the greater cornu and body of the hyoid bone, and it inserts on the side of the tongue, just above the IL muscle. The HG depresses the tongue (downwards), and also pulls its sides down when contracted.

Inferior Longitudinal (IL) - This is a narrow muscle with an oval cross-section, with fibres running along the bottom length of the tongue with one end near the anterior tip of the tongue, and the other merging with the SL, posteriorly. The IL muscle blends with the HG and SG, posteriorly, but is separated from the GG muscle by the septum.

Superior Longitudinal (SL) - The SL is a thin sheet-like muscle near the top surface of the tongue, with fibres running along the top length of the tongue. It is thicker in the middle, medially, and thinner on the sides. It originates near the epiglottis and the hyoid bone, from the median septum, runs along near the top surface of the tongue, and terminates near the anterior tip of the tongue.

Transversalis (T) - This muscle, together with the verticalis forms the major anterior thickness of the tongue. It is located between the IL and SL, and its fibres are aligned laterally (from side to side).

Verticalis (V) - The verticalis consists of groups of bundles which run in a vertical direction between the IL and SL muscles. They are located in the same region as the transversalis, but almost orthogonal to it. Together with the transversalis, these two muscle groups make up about a third of the substance of the tongue.

Mylohyoid (MH) - This muscle runs laterally at the base of the tongue, from one side of the inner surface of the mandible, to the other. It is attached to the body of the hyoid bone as well. It

forms a support structure for the tongue, in a sling-shape. It is also involved in elevating the hyoid bone, and the base of the mouth, and depressing the mandible.

Stylohyoid (SH) - This muscle is attached to the styloid process of the temporal bone of the skull, and the lesser cornua of the hyoid bone. When contracted, this muscle elevates, and pulls the hyoid bone towards the back of the mouth (posteriorly).

Hyoid Bone - The hyoid bone, located in the base of the tongue and just above the larynx, is the only bone in the human body not articulated with another bone. It is held in place by muscles and ligaments. The hyoid bone is shaped like a horseshoe, and consists of five segments: a body, two greater cornua (or horns), and two lesser cornua (see Figure 3.8). The hyoid bone serves as a means of support for the tongue, and plays a significant role in speech, and swallowing.

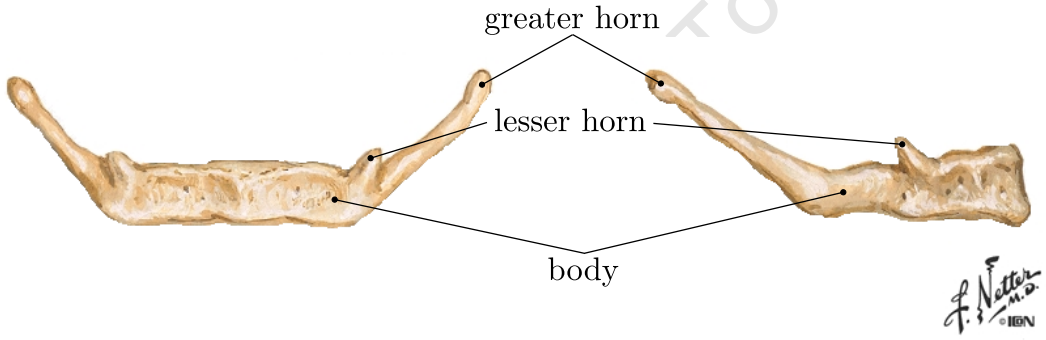

Figure 3.8: Anterior (left) and right lateral (right) view of the hyoid bone [99]

Digastric - The digastric muscle has two main bodies, separated by an intermediate ligament attaching it to the hyoid bone. The anterior belly is attached to the inner surface of the lower mandible, and the posterior belly is attached to the mastoid process of the temporal bone of the skull. This muscle elevates the hyoid bone and depresses the mandible for opening of the mouth.

Styloglossus (SG) - This muscle orginates from the styloid process on the temporal bone of the skull. It merges with the IL just below the area where the PG muscle does the same, on the side and undersurface of the tongue. Contraction of this muscle elevates the tongue, and draws it towards the back of the mouth (posteriorly).

Palatoglossus (PG) - This extrinsic muscle has one origin near the anterior surface of the soft palate, and the other merging with the top of the HG muscle, vertically, and the IL horizontally on the sides of the tongue. When contracted, this muscle elevates the posterior of the tongue, and also draws the soft palate towards the posterior of the tongue.

3.3 Medical imaging of the HUA

The human upper airway (HUA) has been studied seriously, in one way or another, for many decades. It is a critical region of interest for studying some important bodily functions such as linguistics, digestion, and breathing. Studies have been carried out on biological components in this region of interest, such as the tongue myoarchitecture [1], as well as the various biological functions which occur in this region. Various imaging techniques have been developed and adapted to capture data on the tissues and organs in this region of interest.

There are various imaging techniques which have been employed to study OSA and linguistics. Recently, techniques such as MRI, CT and fibre optics have been used to improve the understanding of OSA. There are studies done on the upper airways with relatively new techniques, such as diffusion tensor imaging (DTI) [43]. The implementation of tagged MRI techniques to OSAS studies are also relatively recent [14]. There is an ever-increasing effort in trying to improve the understanding of this disorder.

3.3.1 Cephalometry

Cephalometry is defined as a study of the measurement of the head with relation to specific reference points. Basic X-Rays or ultrasound scans are commonly used in dentistry. It is a low-cost, easily available, quick and standardized method of examination. The scans are limited to awake, static and uniplanar cases only [30].

3.3.2 Magnetic resonance imaging

Magnetic resonance imaging (MRI) is a non-invasive medical imaging technique used to examine the internal structure and function of the human body. MRI can be used on soft tissue as it shows good contrast between tissue types.

There has been research into facial muscle pathological studies using MRI scans. Experimentation with T2 and T1 weighted scans, and ultrashort excitation times (UTE) have been used to analyse facial muscle conditions and pathologies [34]. MRI has also been successfully used in linguistic studies to capture images of the vocal tract for different speech articulations, and the construction of three-dimensional models from them [32]. An example of this is illustrated in Figure 3.9.

Studies of children with OSAS, using MRI, show that this is likely due to inflammation of the adenoids or tonsils. The larger size of the soft palate was another cause for OSAS in these cases [4]. It was also found using MRI, that the changes in the velopharynx cross-sectional area during respiration of OSA subjects was significantly different to that of healthy subjects, especially during

the sleep state. This may contribute to OSAS patients have a more collapsible velopharynx [20]. Some research on OSAS using MRI, has shown that mandibular advancement, a surgical procedure, increases the cross-sectional area of the airway, thus reducing the severity of the OSA [146].

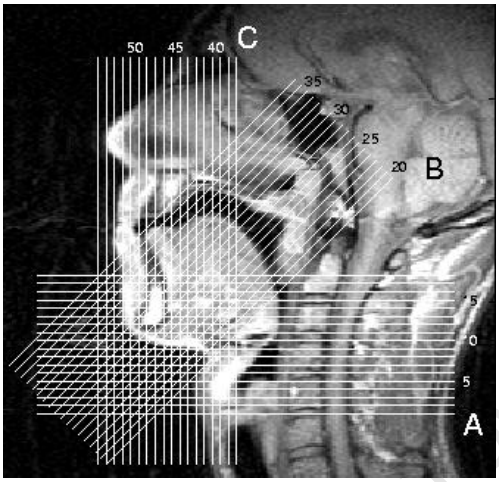

Figure 3.9: Three-dimensional reconstruction of the HUA using MRI slices. The white lines indicate image slices. Three sets of image slice series can be seen (A, B and C) [32].

Conventional MRI scanning takes too long to record an apneic event in a sleeping person [30]. Fast MRI techniques can be used for better results with sleeping patients [20]. A specialized technique, called phase-contrast MRI (PC MRI), can be used to detect mechanical properties, such as strain, similarly to tagged MRI [35].

3.3.3 Tagged MRI

This MRI technique has been used for many years in detecting cardiac deformations. Pharyngeal wall motion is also captured using this technique. Using MRI, combined with non-invasive tissue tagging, the motion of the upper airway during active dilatation can be captured (Figure 3.10).

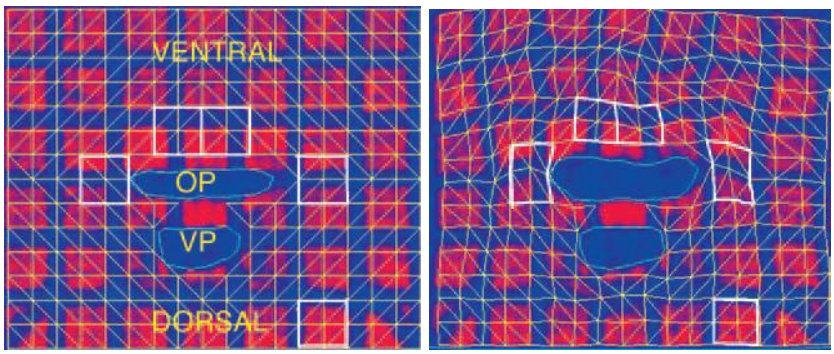

(a) Initial grid (b) Deformed grid

Figure 3.10: Tagged MRI showing pharyngeal wall strain in a rat [14]

The tissue-tagging technique known as spatial modulation of magnetisation (SPAMM) uses a series of radio-frequency (RF) and magnetic field gradient pulses to generate a grid of dark lines, evenly spaced on the target tissue. While conventional MRI and CT scans can detect the volume of soft tissue structures of the airways fairly well, tagged MRI has the added advantage of determining mechanical properties of the tissue (such as strain) as well. The strain, or deformation of the pharyngeal walls and tongue can thus be measured [14, 98].

Harmonic phase (HARP) analysis can be used with the tagged MRI technique, to measure planar strain in the airways. The HARP method uses a band-pass filter applied to the image spectrum, and then calculates its inverse Fourier transform. The result is used to track planar motion. Three-dimensional spline interpolation is used to extrapolate the motion planes in three dimensions. Three-dimensional motion of the tissue can hence be tracked using this technique[79].

Tagged MRI shows potential for further development. This is of particular interest, as the measurement of mechanical properties by this technique, such as strain, are vital in improving understanding of airway tissue mechanical relationships. There is potential for much more development in research using MRI in general as well.

3.3.4 Computed tomography

Computed tomography (CT) is a medical imaging technique using tomography (imaging by sections). A three-dimensional image of an object is generated from a series of two-dimensional X-ray images taken around an axis of rotation. CT scanning is used to investigate the changes in the shape of the pharyngeal wall in OSA patients during the breathing cycle (Figure 3.11).

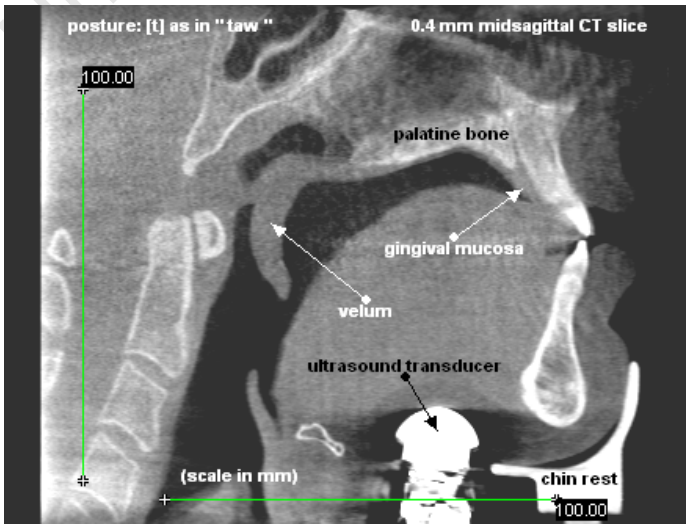

Figure 3.11: CT image of the human tongue [33]

CT has been shown to give accurate measurements of the upper airways using axial image slices at multiple points along the airway [15]. Cine-CT is used to display various slices simultaneously, as a volume, and also at various stages of the breathing cycle [75]. CT scans may be used to evaluate OSAS in patients. They have also been used to compare upper airways of OSAS subjects with healthy ones [15]. The change in shape of the airways during respiration does cause some problems in obtaining accurate results from scans. Four-dimensional CT scanning, in which there are three spatial dimensions, and a fourth dimension for the respiration factor have been implemented [144].

CT has been used to show that the use of an oral appliance over time, in some cases, increases the airway dimension, and thus alleviates the severity of the OSAS in these subjects [75]. Generally, CT scanning has scanning times too long to record an apneic event, due to slow speeds of the gantry system. Fast scanning may have research potential, but is impractical for everyday diagnostic purposes [30]. From CT scans, and computational modelling, it has been shown that sizes of cross-sectional areas of the airway, and the body mass index (BMI), are good factors for assessing the severity of OSAS [132].

3.3.5 Anatomical optical coherence tomography

Measurement of sizes and shapes of upper airways can be used to determine contributing factors to OSA, and effectiveness of various treatments on offer. Anatomical optical coherence tomography (aOCT) is a minimally invasive endoscopic imaging technique based on near-infrared light which can be used to measure sizes and shapes of parts of the upper airways. Measurements of the cross-sectional area can be determined at various locations in the upper airways. There are no radiological effects on subjects undergoing this examination. This is a real-time imaging technique for capturing the detail of the HUA. It was found that the size, rather than the shape abnormalities in OSAS subjects, are better anatomical predictors of OSAS [5, 133].

3.3.6 X-Ray fluoroscopy

Fluoroscopy uses X-rays with an endoscope and produces real-time images of internal anatomy. This technique is advantageous in that it is easy to use, and can return dynamic, real-time results. In addition, the patient can be arbitrarily positioned, and in any state, passive (asleep), or active (awake). High-radiation dosage during scans, low sensitivity of results, and the inability to perform cross-sectional cuts of the region of interest, make this technique somewhat impractical [107].

3.3.7 Nasopharyngoscopy

Nasopharyngoscopy is the dynamic (real-time) examination of the HUA (nasopharynx) using a flexible fibreoptic scope inserted into the HUA through the nose, with the patient under anaesthetic,

and lying on their back. Various manoeuvres can be performed by the patient, and the resulting dynamics can be observed in real-time. A Muller's manoeuvre is used for cases of snoring or sleep apnea. In this manoeuvre, the patient is asked to breathe with the nostrils pinched close. This generates a negative pressure in the airway. This usually reveals inward movement of the soft palate, or contracting of the side walls of the velopharynx, at the base of the tongue [119].

3.3.8 Ultrasound

Ultrasound (US) has been used to image the tongue during speech for more than twenty years. An example of such a scan can be seen in Figure 3.12. The US scans are real-time and non-invasive, however, graphical detail is limited compared to other imaging methods. The subject may be scanned in the supine position, however, excessive motion of the head has to be limited with a cervical collar. Contours of the airway structure can be found and measured using US [33].

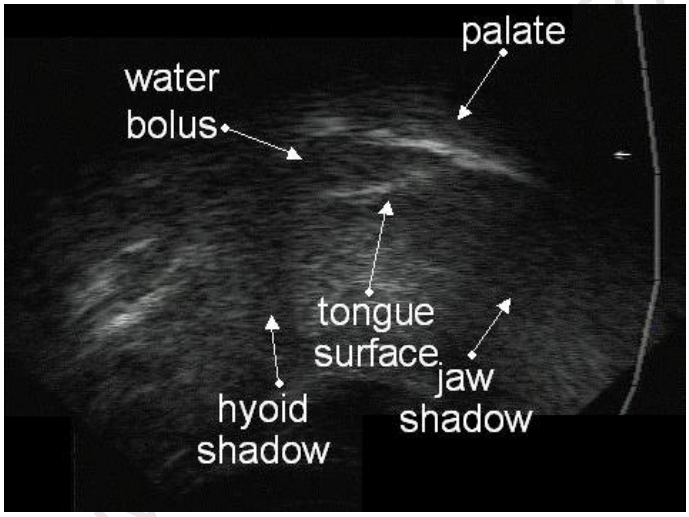

Figure 3.12: Ultrasound image of the human tongue [33].

3.3.9 Diffusion tensor imaging

Diffusion tensor imaging (DTI) is a useful MRI technique which can capture complex fibre architecture of muscles and other fibrous biological materials. The technique tracks and records anisotropic particle movement along the muscle fibre direction, and hence it can map individual muscle fibre orientations, as illustrated in Figure 3.13. Complex geometrical relationships between muscle groups can be determined using this technique [97].

Diffusion spectrum imaging (DSI) allows for multiple fibre orientations at one point in space, whereas DTI, only allows one [43, 45, 47, 81]. DSI can therefore be used to display crossing fibres as well, which makes it more versatile than DTI for mapping the tongue, with its complex musculature.

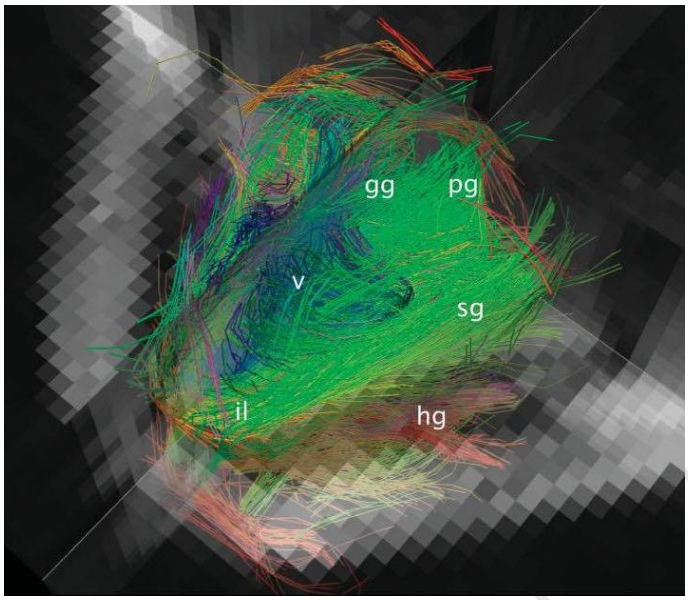

Figure 3.13: The human tongue musculature captured using DTI [47].

DTI and DSI show promise in capturing highly-resolution visual data. The inherent ability to capture intricate muscle fibres creates opportunities to improve the understanding of muscle structure of the HUA.

3.4 Skeletal muscle

The human tongue is made up mainly of skeletal muscle tissue. Skeletal muscle is so named, because it is primarily attached to, and involved in the movement of parts of the skeleton. Skeletal muscles are voluntary muscles, as they contract and relax consciously. Some of the main functions of skeletal muscle tissue are to induce motion, provide stability, and to move substances within the body [126]. Muscles of the tongue and HUA also play a role in speech. In general, muscle tissue has five basic characteristics [126]:

1. Excitability - the ability of muscle to respond to a stimulus by producing electrical impulses.
2. Conductivity - the ability of a muscle cells to conduct electrical impulses along its plasma membrane.
3. Contractility - the ability of muscle tissue to generate a force by shortening in response to a stimulus.
4. Extensibility - the ability of muscle tissue to be stretched without damage.
5. Elasticity - the ability of muscle tissue to return to its original size and shape after deformation.

3.4.1 Skeletal muscle structure

Skeletal muscles exhibit a hierarchical structure, when observed at different levels of magnification. A muscle, at the largest scale, is covered by connective tissue, namely, the epimesium. Many bundles of muscle fascicles are arranged within a muscle, and each fascicle is surrounded by its own connective tissue, namely, the perimesium. Muscle fascicles are composed of long cylindrical cells, namely, muscle fibres, each one surrounded by endomesium tissue. Muscle fibres are considered to be the structural units (cells) of skeletal muscle, and range from 10 to 100μm in diameter. Most have a length of 100μm, but some fibres can be up to 30 cm in length. Muscle fibres consist of many force-producing cells, known as sarcomeres. Sarcomeres are the basic contractile part of the muscle tissue [49, 53, 66, 89, 142].

Myofibrils consist of numerous amounts of sarcomeres arranged in series and parallel to each other. A group of myofibrils arranged in parallel, make up a muscle fibre. This repetitive nature of the structure of the muscle tissue suggests that, in terms of its mechanical behaviour, the muscle is ultimately a scaled up version of a sarcomere.

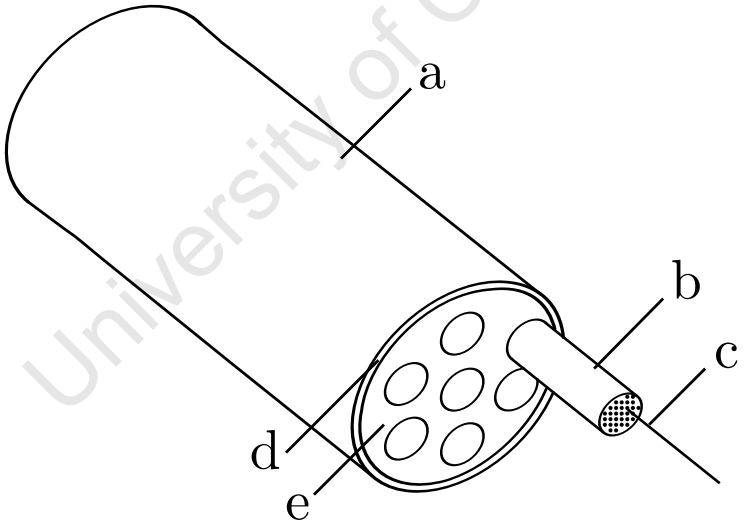

Figure 3.14: A breakdown of muscle structure. (a) muscle fibre, (b) myofibril, (c) muscle filament, (d) sarcolemma, (e) sarcoplasm

The muscles fascicles of the human tongue are arranged into identifiable muscle groups. In some regions of the tongue, one specific muscle group may be dominant, but there are regions where there is more than one muscle, and the fibres of each muscle group are interdigitated. This gives the tongue a highly complex structure, and also can be used to explain why it is so highly manoeuvrable [114].

Figure 3.15: Crossing muscle fibres of the tongue, transversalis (T), verticalis (V) and longitudinal (L) muscles [114].

3.4.2 The motor unit

A motor neuron delivers the signal that causes muscle fibres to contract. A motor unit is composed of a neuron, and a group the group of muscle fibres it stimulates. It is considered to be the smallest part of a muscle that can contract independently. The level of activation, and hence contractile force, in a muscle is dependent on the number of activated motor units. Muscles used for precise movement have a higher concentration of motor units.

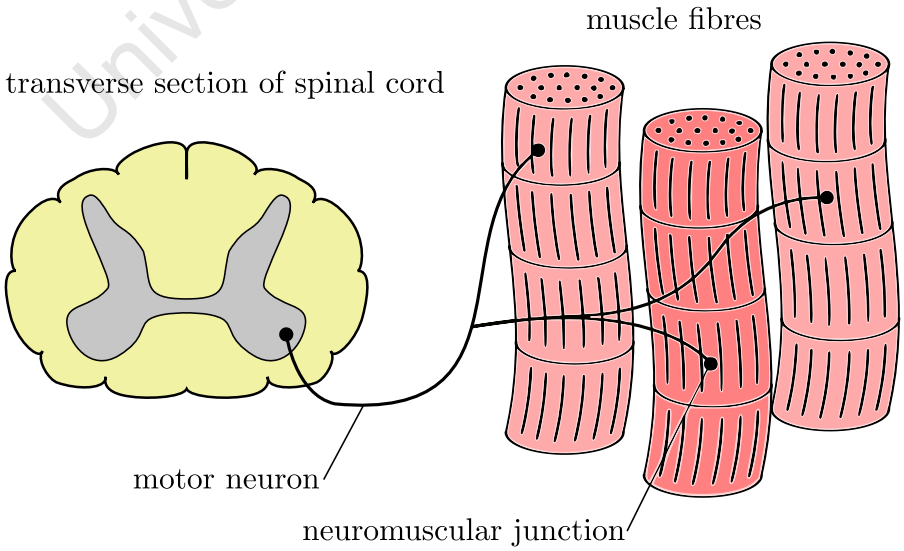

Figure 3.16: A motor unit of muscle tissue

3.4.3 The muscle sarcomere

The muscle sarcomere is the basic contractile unit of muscle tissue. Sarcomeres consist of three different filament systems made of specific proteins, and can be described as being striated, or banded. The thick filaments, made of myosin, are arranged hexagonally when viewed axially. The thin filaments, made of actin, are arranged tetragonally when viewed axially. Nebulin, found in the I-band of the sarcomeres, and titin (also called connectin), found in the I-band and A-band of the sarcomeres, give stability and support to the sarcomere. Cross-bridges are protrusions in the myosin, in the direction of the thin filaments, and are the active components of contraction. The structure of a sarcomere is illustrated in Figure 3.17.

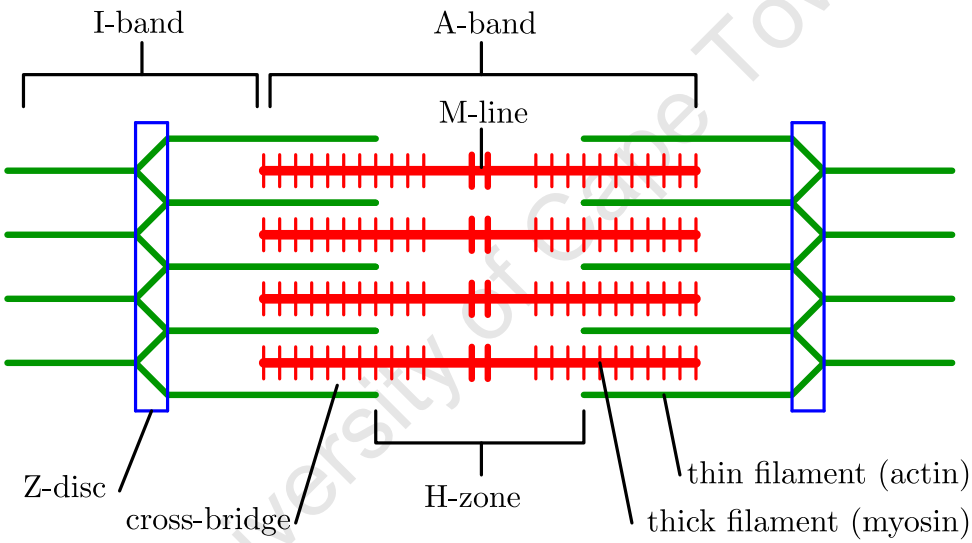

Figure 3.17: A single muscle sarcomere.

In the 1950s, J. Hanson and H. Huxley [66] developed a new theory on the mechanism of muscle contraction. Previously, it was thought that muscle contraction was a result of a folding mechanism, but Hanson and Huxley proposed that contraction was caused by sarcomere filaments sliding past each other. This model is known as the sliding filament mechanism of muscle contraction [126]. In this sliding filament model, cross-bridges, or myosin heads, pull on the thin filaments (actin), causing them to slide inwards towards the H-zone of the sarcomere. This causes a contraction in each activated sarcomere, and hence a contraction in the overall muscle tissue. A contractile force is thus generated in the muscle tissue. A contracted sarcomere is illustrated in Figure 3.18. More detail on the workings of muscle contraction can be found in various works on anatomy and physiology, for example G. J. Tortora and S. R. Grabowski [126].

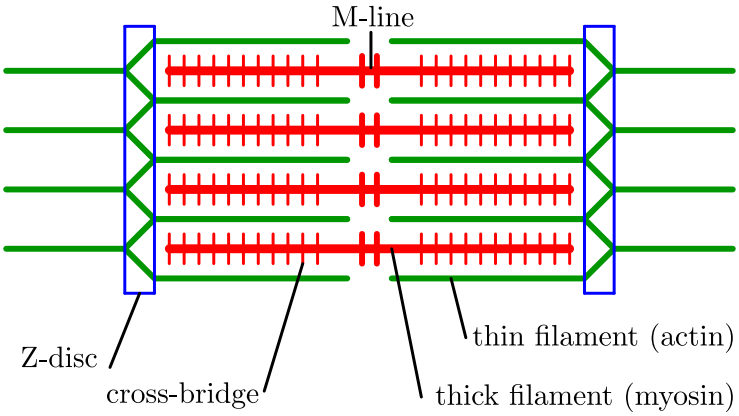

Figure 3.18: A muscle sarcomere in contraction.

3.4.4 Muscle stimulation and muscle tone

A twitch is a single stimulation-contraction-relaxation sequence in a muscle fibre. Wave summation occurs when muscle stimulation signals arrive at the muscle before it has fully relaxed from a previous stimuli. This causes an increase in the contractile state of the muscle. At a certain stimulation rate, the muscle can partially relax between successive stimuli. This is called incomplete tetanus. At a certain increased rate, there is no time for relaxation between successive stimuli, and complete tetanus occurs. This process is illustrated in Figure 3.19. This allows for a wide variation of the force produced in the muscle.

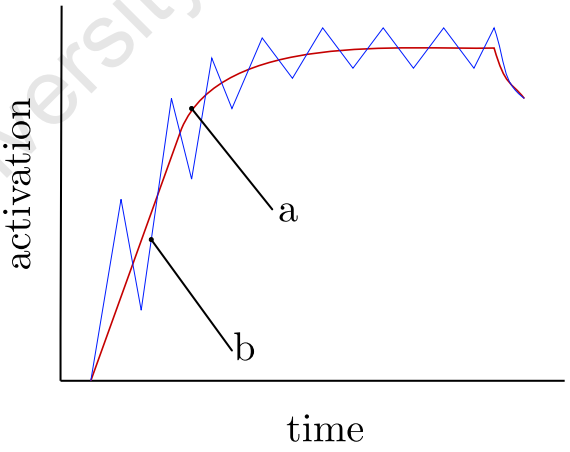

Figure 3.19: Myogram showing an example of (a) complete tetanus (smooth), and (b) incomplete tetanus (jagged), of muscle tissue.

Muscle tone is the result of the involuntary activation of a small number of motor units, causing a sustained firmness in the relaxed muscle. A small percentage of muscle fibres are contracted, while the rest are in a relaxed state, providing overall firmness without contracting the muscle. Hypotonia is the condition of decreased muscle tone, which plays a role in some OSA cases [126].

3.4.5 Isotonic and isometric contractions

An isotonic contraction occurs when a muscle undergoes a change in length under an applied load. Isotonic contractions can be either concentric or eccentric. For concentric contractions, the muscle tension exceeds the resistance and the muscle shortens. For eccentric contractions, the muscle tension developed is less than the resisting force, and the muscle elongates.

An isometric contraction occurs when the muscle does not or cannot change length, but the load in the muscle increases. An example of this is holding a weighted object in a fixed position. The load causes stretching, and the muscle counteracts this by contracting and an increase in tension is experienced. Although there is no movement, energy is still expended in maintaining the increased tensile force in the muscle. Most movements of the body use a combination of isotonic and isometric contractions [126].

4 Geometrical Modelling Of The Human Tongue

The geometrical data for the HUA was acquired from the open-source Visible Human Project (VHP) dataset. This dataset has both male and female specimen data of varying detail. The dataset itself consists of digital colour photographs, MRI, CT, and raw image data of the entire human body [102].

Various approaches to extracting the geometry of the tongue were experimented with. These include using CAD software, and the image processing tools available in MATLAB [91]. Ultimately, the medical image processing software package, Mimics [100], was used due to its advanced image and geometry processing tools. Each approach is discussed in this chapter.

4.1 The Visible Human Project

The Visible Human Project (VHP)® is an ongoing effort to create highly detailed three-dimensional anatomical models of the human body. The original dataset includes photographs of a male and female cadaver that were sliced and photographed at 1mm and $\frac{1}{3}$mm intervals respectively. The resolution of the digital images is 2048×1216 pixels with $\frac{1}{3} \times \frac{1}{3}$mm pixel size and 24-bit colour tone. A single image of the VHP dataset is shown in Figure 4.1.

Figure 4.1: VHP female dataset image sample taken midway through the head [102]. The blue material surrounding the subject is an immersive gel used for suspending and holding the cadaver in place.

The dataset also includes MRI and CT data. MRI images of the body were obtained at 4mm longitudinal intervals. The MRI images are at a resolution of 256×256 pixels with each pixel made up of 12-bit gray tone. The CT data consist of axial CT scans of the entire body taken at 1mm intervals at a pixel resolution of 512×512 with each pixel made up of 12-bit gray tone [102]. The female dataset was selected for use in this project due to its higher level of detail. In addition, the female dataset has less post-mortem deformation in the region of interest, i.e. the HUA, than the male.

4.2 Contour extraction in Pro-Engineer

Pro-Engineer is a parametric computer aided engineering (CAE) software package created by Parametric Technology Corporation (PTC) [125]. An attempt was made to import individual images from the VHP dataset into Pro-Engineer, and manually trace contours for the desired geometry as illustrated in Figure 4.2. This approach would have taken a considerable amount of time, and may not be the most accurate means of acquiring the geometry.

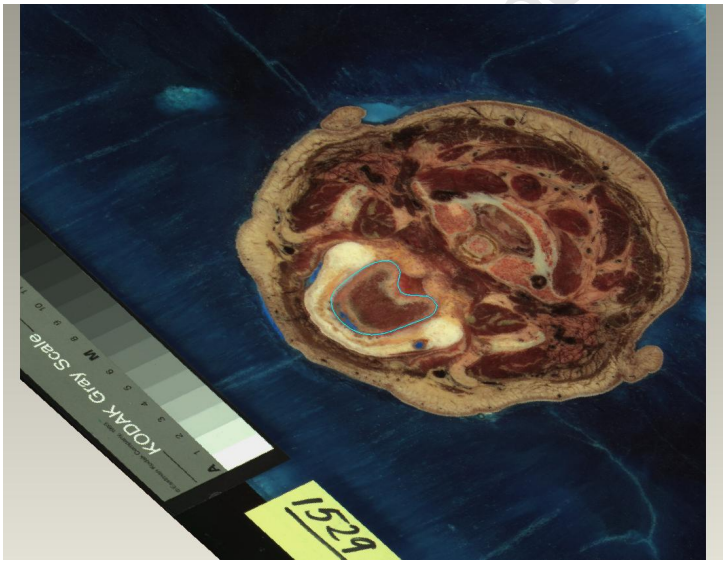

Figure 4.2: VHP contour extraction in Pro-Engineer (contour highlighted in blue).

4.3 Contour extraction in MATLAB

In order to reduce image processing time, and overall accuracy, an attempt was made to extract contours in MATLAB [91] by running an automated process. The VHP colour images were read into MATLAB in series. These images were then converted from colour to binary, with lighter colours transformed to white, and darker colours to black, according to a separation value setting. A filter was applied to remove relatively small irregularities. Each image was then processed using edge

detection tools to mark the edges as contours. The contoured images were filtered according to size on the two-dimensional image plane. The most relevant contours are then selected and eventually they could be used to construct an approximate three-dimensional geometrical model (Figure 4.3).

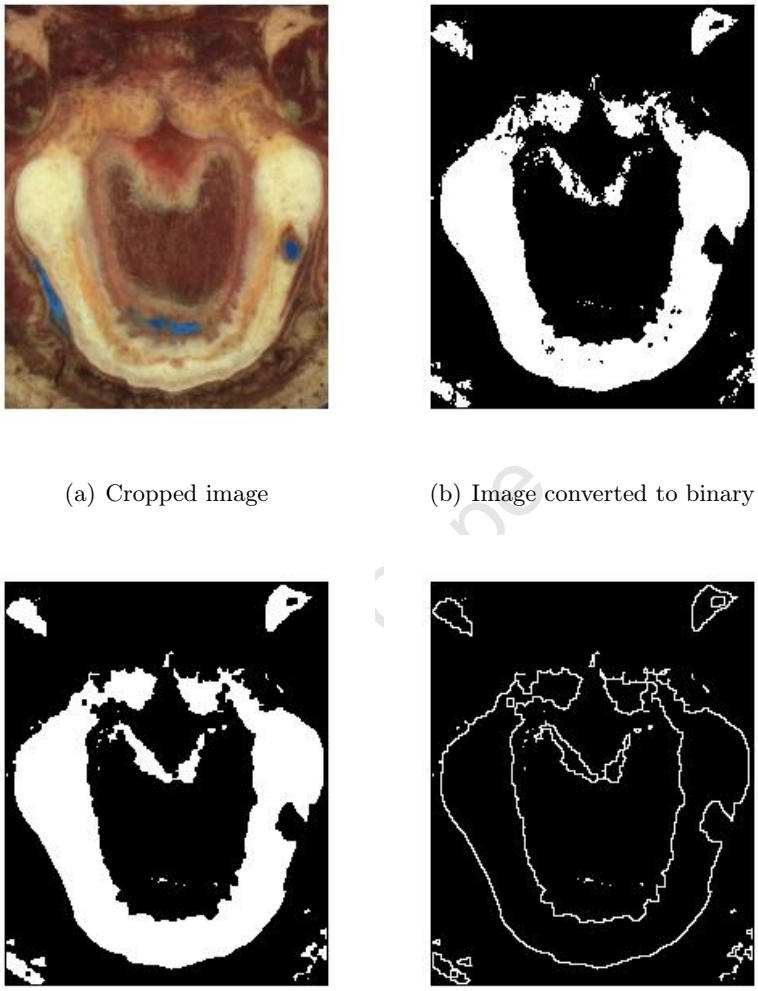

(a) Cropped image

(b) Image converted to binary

(c) Filtered image

(d) Contoured image after edge detection

Figure 4.3: Various stages of image processing of a VHP image in MATLAB.

4.3.1 Edge detection in MATLAB

Edge detection aims to identify points in an image which exhibit sharp changes, or discontinuities in image brightness, or colour. In the case of the VHP images, sharp changes in colour indicate edges of different biological tissues. These edges form contours when the edge detection tool is applied to the images. The contours that are derived from the tongue can be manually selected. The contours of sequential images are used to construct a three-dimensional model of the tongue.

4.4 Geometrical modelling in Mimics

Mimics is a commercial image processing software package used for design and modelling, developed by Materialise NV [100]. Mimics allows its users to create and modify three-dimensional computational models from a series of imported images. Various image formats can be imported and used, including RAW, CT, MRI, BMP, JPG, DICOM and TIFF, to name a few. Mimics exports computational models in various formats, readily usable with FE software.

The VHP data was imported into Mimics as a series of bitmap images. A slice thickness was assigned to these images, transforming the image pixels to voxels. Each slice of voxels represents one of the images from the dataset, with the specified thickness, equivalent to the actual distance between individual slices of the dataset. The thickness for the female data is $\frac{1}{3}$ mm. In addition, the dimensions of each highly detailed slice are precise up to $\frac{1}{3}$ mm. Hence, the voxels generated by this process are $\frac{1}{3} \times \frac{1}{3} \times \frac{1}{3}$ mm, for the female dataset. A set of 200 sequential images were used. These range from just below the nasal opening, to just below the digastric muscle and epiglottis, and measure 66mm axially. This range of data is enough to capture the entire oral cavity. Different views of this dataset can be seen in Figure 4.4.

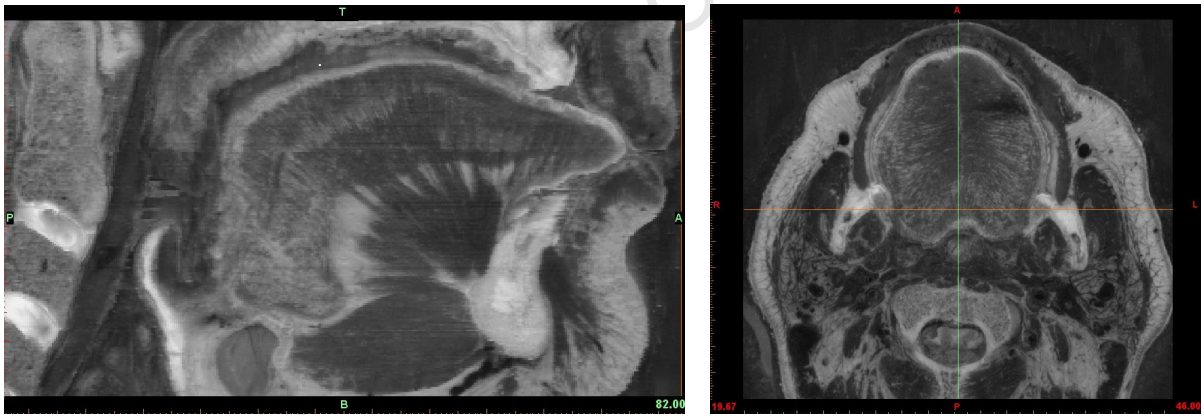

(a) Mid-sagittal view of VHP data, showing a portion of the head

(b) Axial view of VHP data cut through the head, near the tongue

Figure 4.4: VHP data viewed in Mimics.

4.4.1 Image processing in Mimics

Various image processing tools are available in Mimics. Thresholding and dynamic region growing tools were the best for identifying regions of interest in the voxel dataset.

Thresholding allows one to select a range of grayscale values in the voxel dataset. Voxels which fall into the desired range are selected, and the rest of the voxels, rejected. Different tissues can be

selected by applying some threshold filter to the voxel set.

Segmentation refers to the partitioning of the dataset into sets of voxels. The desired segments in this case, are the different muscle groups within the tongue, as well as segmenting the tongue itself, from the surrounding tissue. Segmentation of the uvula and epiglottis can be seen in Figure 4.5.

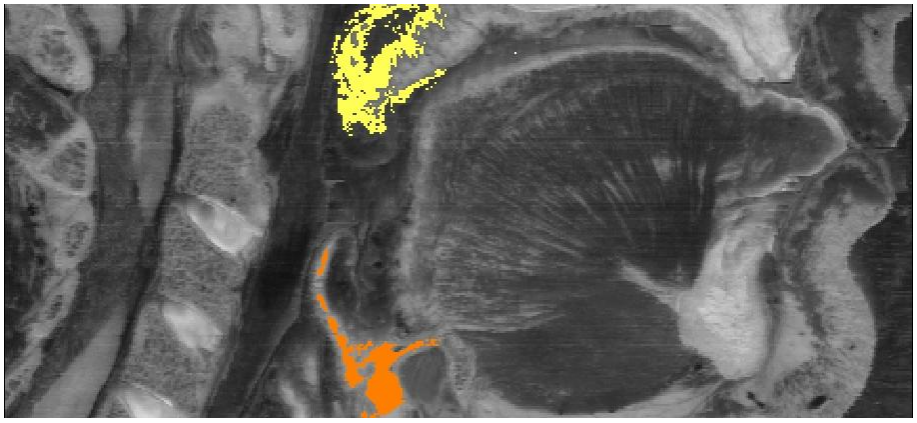

Figure 4.5: Segmentation of uvula (yellow) and epiglottis (orange).

Region growing involves the selection of initial seed points within the voxel set. Neighbouring voxels of the initial seed are selected according to a specified thresholding procedure. The region can hence be "grown" according to the number of neighbouring voxels desired. The dynamic region growing tool in Mimics is used for segmentation of the dataset. To form the entirety of the tongue, various individual regions were merged, and this can be seen in Figure 4.6.

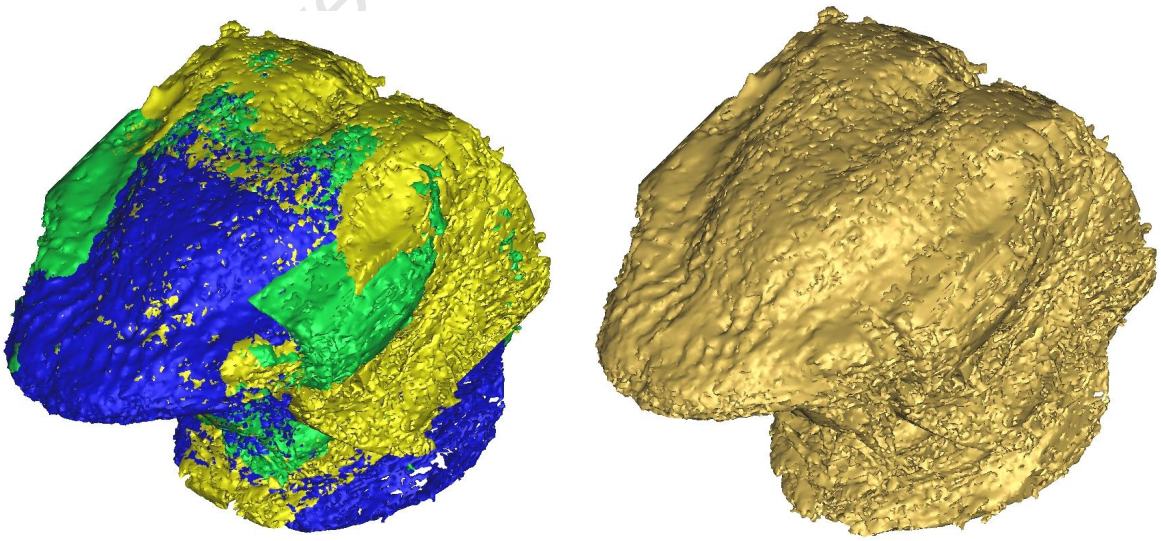

(a) Before merging (b) After merging

Figure 4.6: Merging of different captured regions of the tongue.

4.4.2 Three-dimensional model of tongue geometry

The main body of the human tongue geometry extracted using Mimics can be seen, together with part of the mandible, in Figure 4.7. This three-dimensional model was smoothed and processed to reduce irregularities without losing significant geometrical detail.

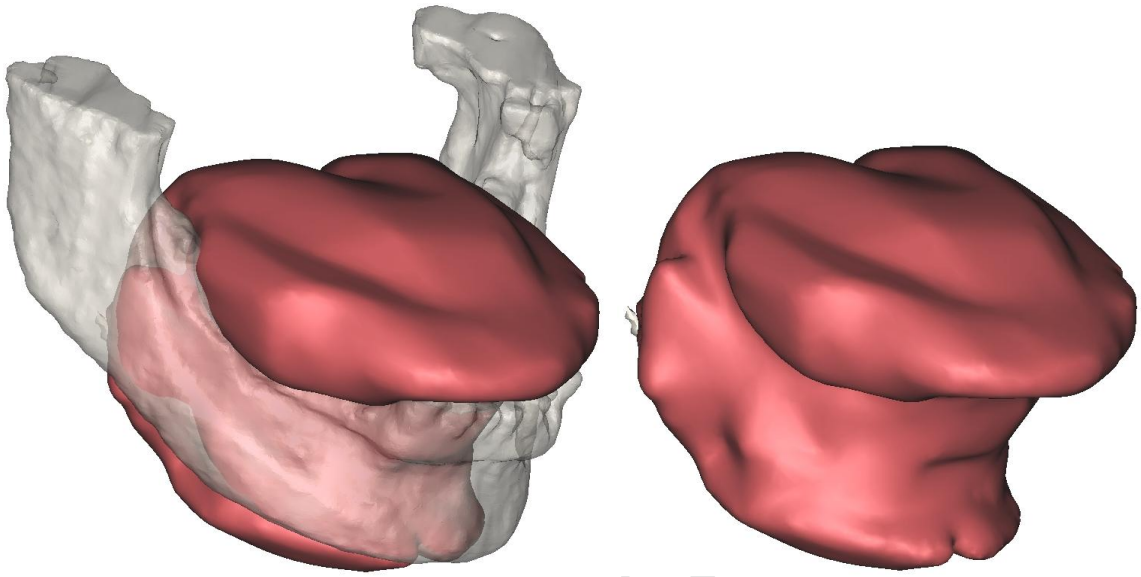

(a) Tongue and mandible (b) Tongue

Figure 4.7: Tongue geometry created from VHP female dataset captured in Mimics.

4.4.3 Geometry of individual muscle groups

The geometry of the individual muscle groups was identified and captured in Mimics. Using colour, grain, and striations (see Figure 4.5) as visual indications of fibre directionality of muscle fibre bundles, and also knowledge of the anatomy, the individual muscle groups were identified, and segmented as illustrated in Figure 4.8.

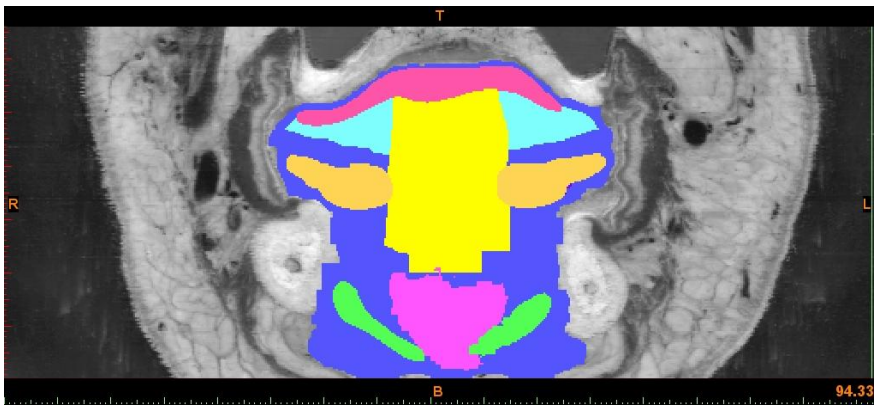

Figure 4.8: Segmentation of muscle groups of the tongue in Mimics.

In most instances, there is a clear distinction in the muscle fibre arrangement in the dataset. Each muscle group is processed using the cylinder tool in Mimics. With this tool, a trajectory for the muscle fibre directions of each muscle group is assigned. Individual muscle groups are illustrated in relation to the overall tongue, in Figure 4.9.

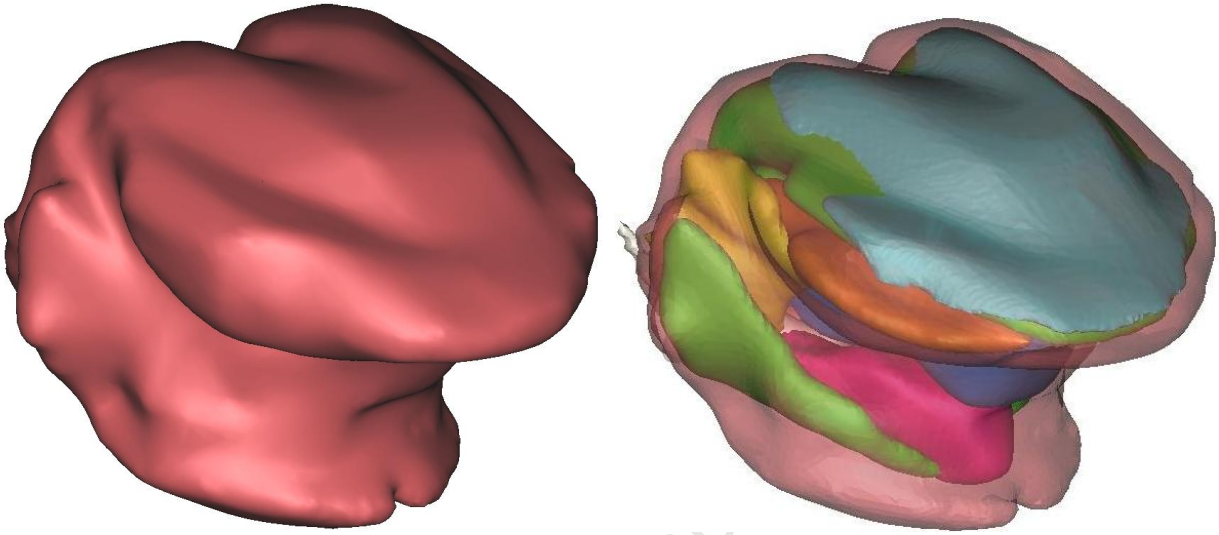

(a) Tongue (b) Tongue showing muscle groups

Figure 4.9: Individual muscle groups shown in relation in the tongue.

The genioglossus (GG), geniohyoid (GH) and hyoglossus (HG) muscles are shown in Figure 4.10.

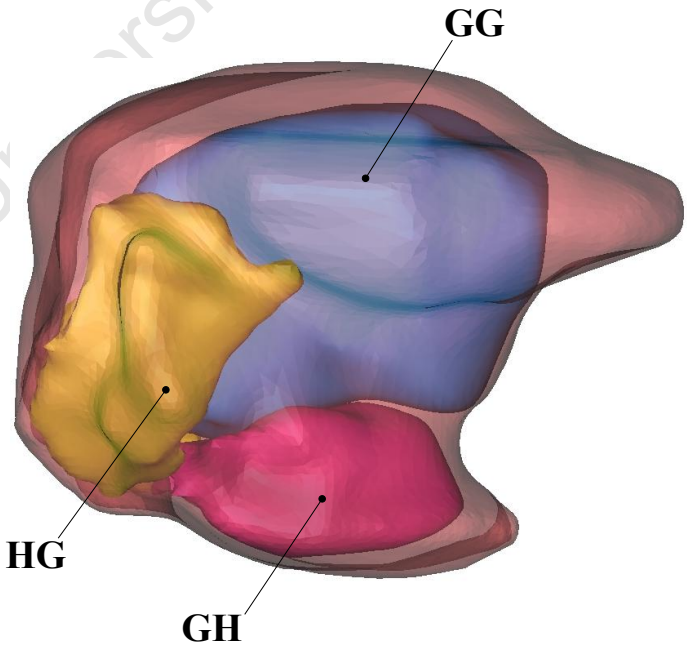

Figure 4.10: Tongue muscles extracted using Mimics. GG-genioglossus, GH-geniohyoid and HG-hyoglossus muscles.

The superior (SL) and inferior (IL) longitudinal muscles are shown in Figure 4.11.

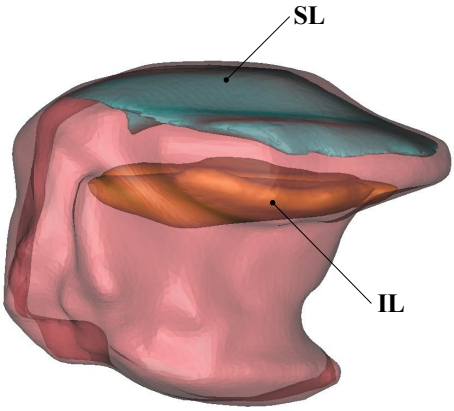

Figure 4.11: Superior (SL) and inferior (IL) longitudinal muscles.

The transversalis (T) and verticalis (V) muscles are shown in Figure 4.12. These muscles occupy a similar volume in the tongue.

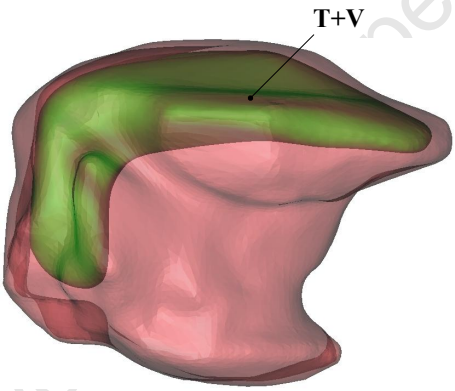

Figure 4.12: Transversalis (T) and verticalis (V) muscles.

The hyoid bone is shown in its position in the tongue, and on its own, in Figure 4.13.

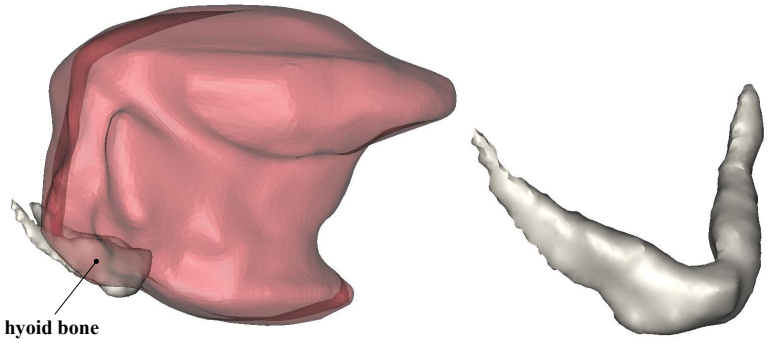

(a) hyoid bone position (b) hyoid bone

Figure 4.13: Hyoid bone shown in its position in the tongue, and on its own.

4.4.4 Processing the geometry

The geometry extracted from the dataset was quite rough, displaying surface irregularities such as holes and protrusions. The geometry also displayed sharp edges, and unrealistic features. A mesh generated from this rough geometry would be hard to work with. These abnormalities were reduced, and the geometry smoothed out using tools available in Mimics. Some of these tools are available in the remeshing module of Mimics. This process is illustrated on the SL muscle in Figure 4.14, and has been applied to the other tongue muscles groups as well.

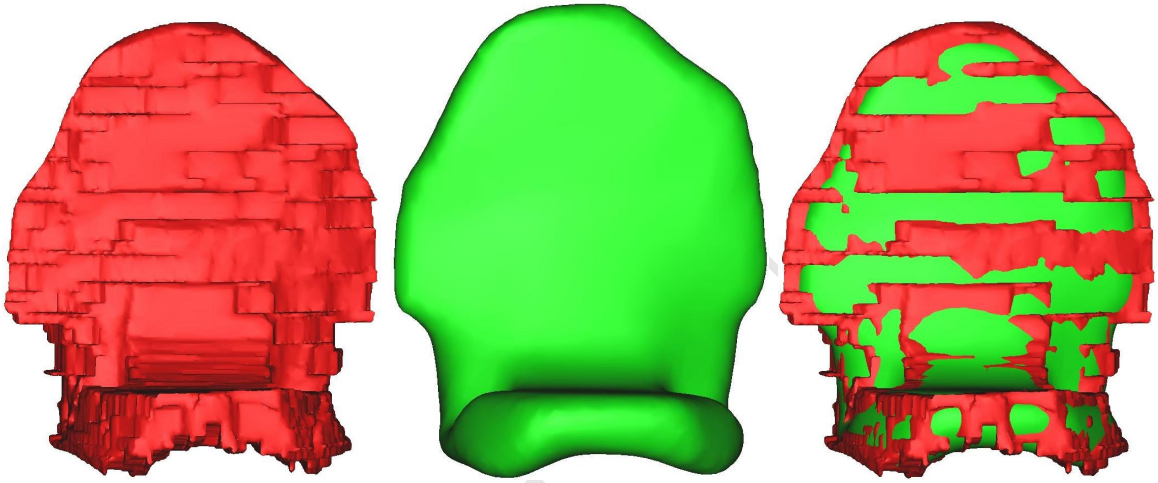

(a) Rough Geometry (b) Smoothed Geometry (c) Overlay showing difference in smoothness

Figure 4.14: Geometry-smoothing process of the superior longitudinal (SL) muscle.

In Mimics, the geometry can be examined and processed in three-dimensional previews. Any irregularities in the geometry can be removed, as seen in Figure 4.15.

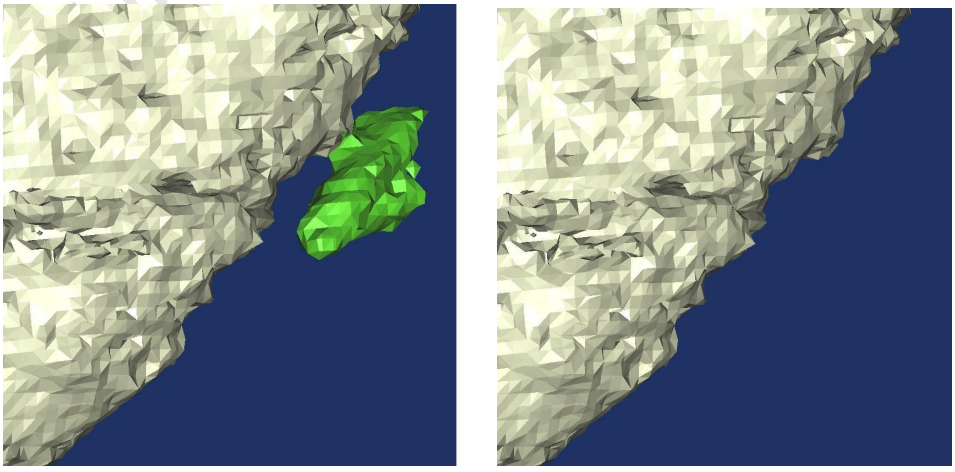

(a) Geometry with irregular protrusion (b) Geometry with irregularity removed

Figure 4.15: Manual cleanup of geometry of the mandible.

4.4.5 Mesh export to Abaqus

In earlier versions of Mimics, the geometry could only be exported as a shell type mesh. With Mimics Version 12.1, and later, it is possible to export volume meshes as well. Abaqus [24], is a commercial finite element software package, which is discussed in further detail in Chapter 6. Figures 4.16(a) and 4.16(b) show examples of exported meshes, with 5000 and 120000 hexahedral elements respectively.

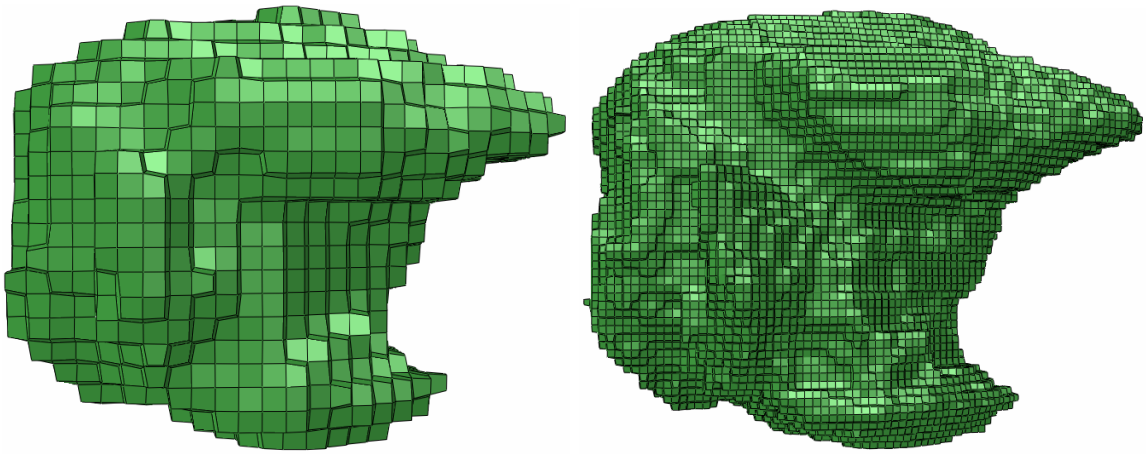

(a) Coarse hexahedral mesh (5000+ elements) (b) Fine hexahedral mesh (120000+ elements)

Figure 4.16: Hexahedral meshes of the tongue exported from Mimics, and viewed in Abaqus.

Smooth mesh from Gambit

A geometry file exported from Mimics was used to create a mesh of the tongue using Gambit ® pre-processing. Gambit is a commercial geometric modeling and grid generation tool. This smoothed mesh has 4800 elements, and is shown in Figure 4.17. This is the mesh that will be used for the simulations to follow.

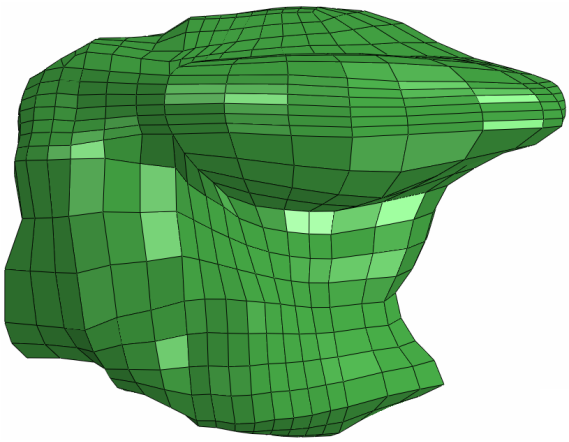

Figure 4.17: Processed mesh from Gambit, viewed in Abaqus

4.5 Capturing the myoarchitecture

The muscle fibre architecture of the tongue is a geometrical feature which is highly influential on the overall mechanical behaviour. The process of muscle fibre data capturing is described here.

A muscle fibre orientation dataset has been acquired through the work of Wilhelms-Tricarico [136, 137]. This dataset was derived from the VHP as well, and hence it can be used to directly compare to the fibre data obtained through extraction in Mimics. The muscle fibre directions were extracted at each gauss point in three dimensions. This fibre data is illustrated in Figure 4.18.

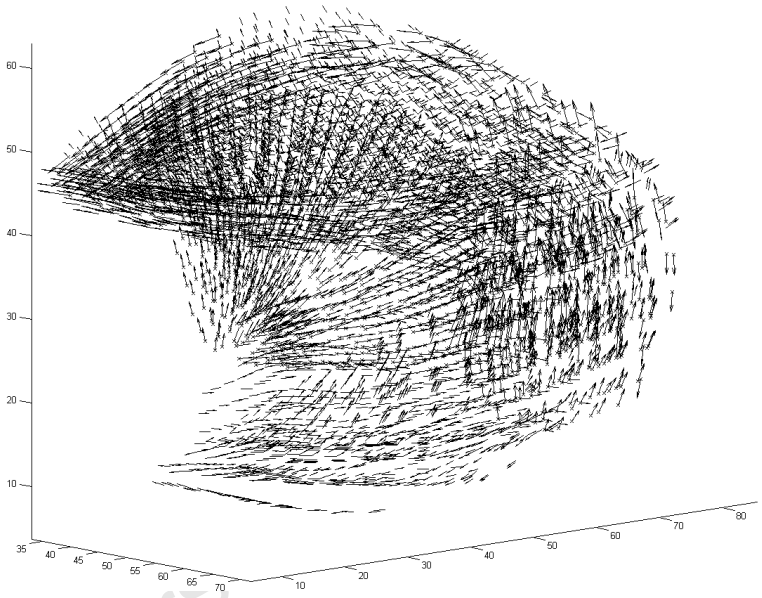

Figure 4.18: Fibre vectors of the tongue, adapted from the work of Wilhelms-Tricarico [136, 137].

MedCAD is an add-on module to Mimics that has a tool which can be used to map muscle fibre directions. This feature, called "cylinder", enables the extraction of geometry which follows trajectories, and has a specified radius. It has been successfully used in the past for veins and arteries [92].

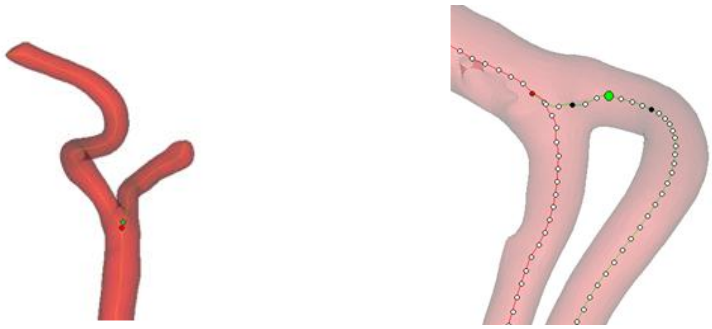

(a) Artery captured in Mimics (b) Artery showing control point, in green

Figure 4.19: Artery geometry created using the Cylinder tool in Mimics.

The trajectory of the cylinder is aligned along the muscle fibre directions. Control points allow one to manipulate the trajectory of these cylinders in three dimensions. The flexibility of this tool enables one to map the muscle fibre directions in the tongue.

4.5.1 Muscle fibres captured in Mimics

The process of fibre extraction was carried out for each muscle group of the tongue. Fibre directions were mapped manually in Mimics using the MedCAD cylinder tool. Using colour, grain and striations (see Figure 4.20) as visual indications of directionality of muscle fibres and also knowledge of the anatomy, the individual muscle groups were identified and segmented using advanced image and geometry processing tools in Mimics. In most instances, there is a clear distinction in the muscle fibre arrangement in the dataset.

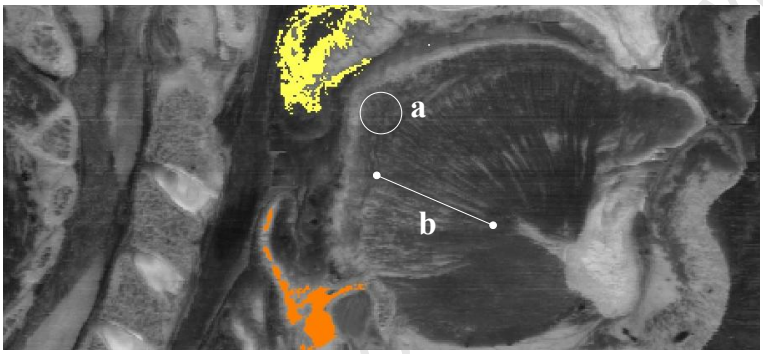

Figure 4.20: Segmentation of uvula (yellow) and epiglottis (orange) from VHP dataset. Typical grainy pattern indicated at point a, and striations indicated at point b.

There are 4800 elements in the mesh of the tongue generated from the geometrical data. The number of elements of the mesh containing fibres belonging to each of the 9 muscle groups extracted are summarized in Table 4.1.

Table 4.1: Tongue muscle groups and number of elements containing specified fibres.

number	muscle name	number of elements containing fibres
01	digastric	171
02	genioglossus	139
03	geniohyoid	261
04	hyoglossus	207
05	inferior longitudinal	219
06	mylohyoid	253
07	superior longitudinal	312
08	transverse	669
09	verticalis	754

Each muscle group is processed using a tool in Mimics. Vectors defining the fibre directions are assigned at multiple points in each muscle group. Muscle fibre orientations of the muscle groups were extracted in Mimics, some of which can be seen in Figure 4.21, overlaid with the geometry of the tongue itself.

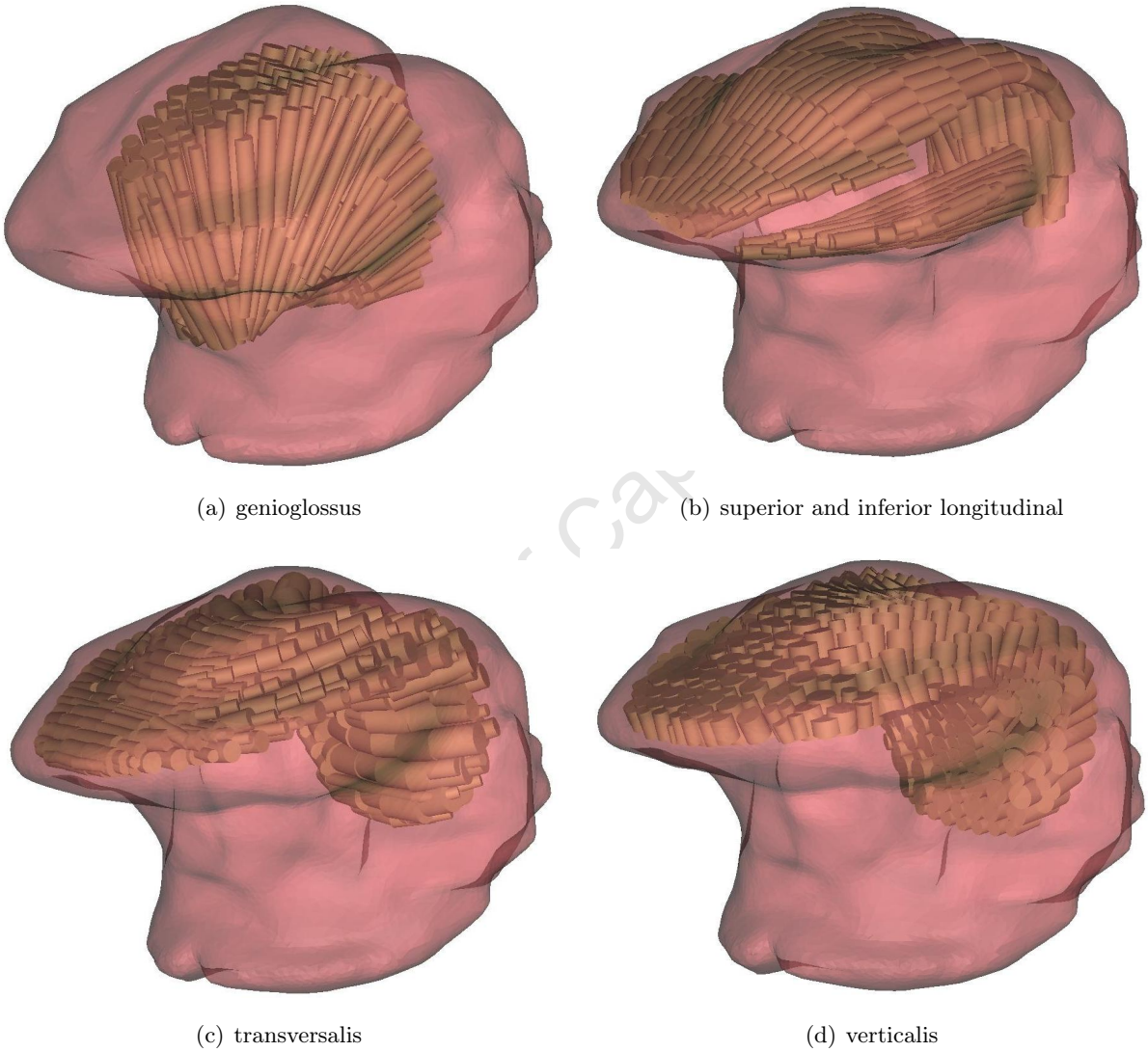

(a) genioglossus

(b) superior and inferior longitudinal

(c) transversalis

(d) verticalis

Figure 4.21: Muscle fibres of various tongue muscle groups, extracted and viewed in Mimics.

The fibre data was combined with a FE mesh using ParaView [67] in a similar way to which Wilhelms-Tricarico has done so [136, 137]. Each element in the mesh is assigned a specific fibre vector. The combined fibre and geometry data is displayed in Figures 4.22(a) and 4.22(b).

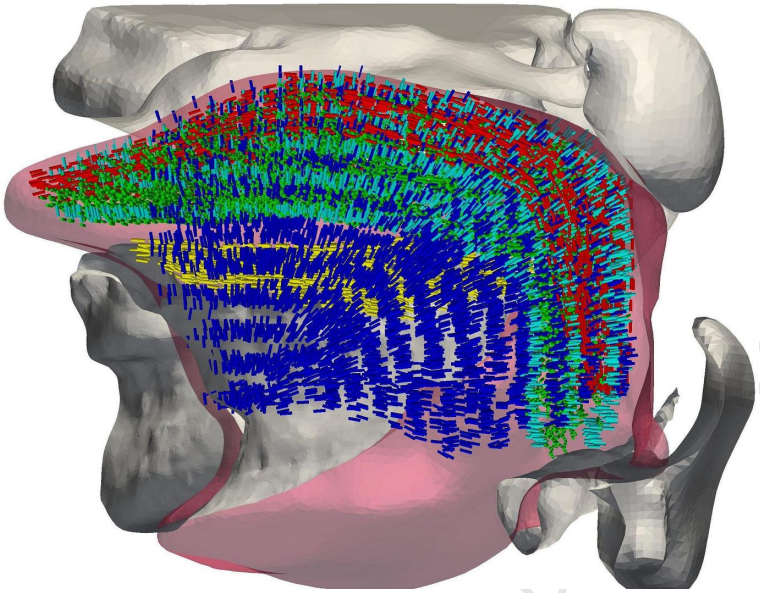

(a) Tongue geometry with fibres, shown with the mandible and the hard and soft palates

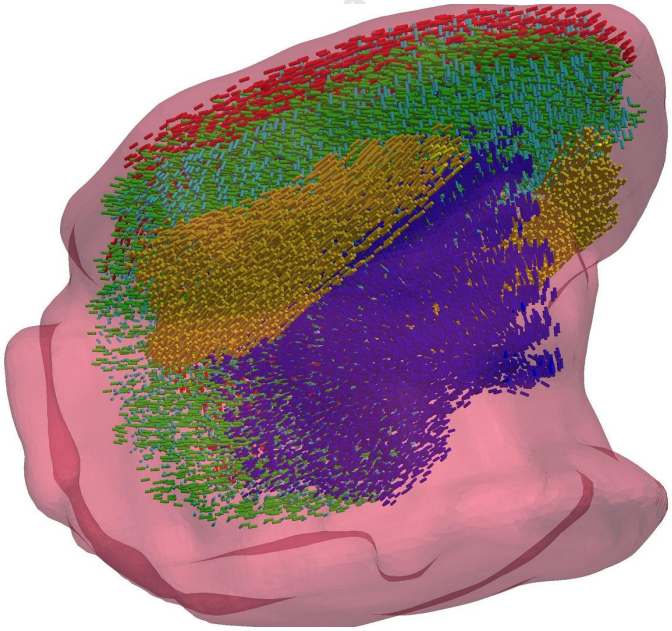

(b) Tongue fibre geometry

Figure 4.22: Tongue geometry with fibres of different muscle groups.

5 Governing Equations

This chapter discusses the model implemented to simulate the macroscopic response of the material of the human tongue under various loading conditions. As mentioned in previous chapters, the human tongue is composed mainly of skeletal muscle tissue. This muscle tissue behaviour has been modelled within the framework of continuum mechanics. Therefore, a brief review of relevant details, including aspects of continuum mechanics, will be given in this chapter. Having presented the basic theory, this chapter then proceeds with an overview of the most relevant constitutive models for skeletal muscle tissue. More detailed accounts on continuum mechanics and biological modelling can be found in Lai [76], Simo [116], Simo and Hughes [117], Fung [42], Holzapfel [55] and Malvern [87], for example. The notation used is relatively standard and follows that used by Simo [116].

Gibbs (or symbolic) notation, and Cartesian (or index) notation, are both used throughout this thesis. With Gibbs notation, vectors are designated by bold-faced letters ($\mathbf{a}$) and scalars are denoted as plain letters (a). Unit vectors are typically represented with a caret placed over a bold-faced letter ($\hat{\mathbf{a}}$). The magnitude of a vector $\mathbf{a}$ is denoted by $|\mathbf{a}|$.

In Cartesian (or index) notation, a group of n numbers a_1 to a_n, can be referred to by the notation, a_i, where the subscript $i = 1, 2, ..., n$. A comma followed by the index j indicates partial differentiation with respect to the jth component. A superimposed dot ($\dot{a}$) indicates differentiation with respect to time t, and a repeated index represents a summation over the range of that index.

5.1 An overview of Continuum Mechanics

Continuum mechanics is a branch of mechanics that deals with the mechanical behaviour of deformable bodies. The body is treated as a continuous medium, and its properties are represented by smooth functions of position and time. It is within this framework that the model for the material of the tongue will be developed.

5.1.1 Kinematics of a continuum

Kinematics deals with the motion and deformation of objects. Consider an arbitrary body moving from reference position Ω_0 to current position Ω_t. The reference position of a material point P_0 is specified by the position vector $\boldsymbol{X}$, and its current position by the position vector $\boldsymbol{x}$ (see Figure 5.1).

The current position can be written as

$$\boldsymbol{x} = \hat{\boldsymbol{x}}(\boldsymbol{X}, t) \ . \tag{5.1}$$

This relation is invertible if

$$J = \det\left(\frac{\partial \boldsymbol{x}}{\partial \boldsymbol{X}}\right) \neq 0 \ , \tag{5.2}$$

in which case the reference position can be expressed in terms of the current position and time, i.e.

$$\boldsymbol{X} = \hat{\boldsymbol{X}}(\boldsymbol{x}, t) \ . \tag{5.3}$$

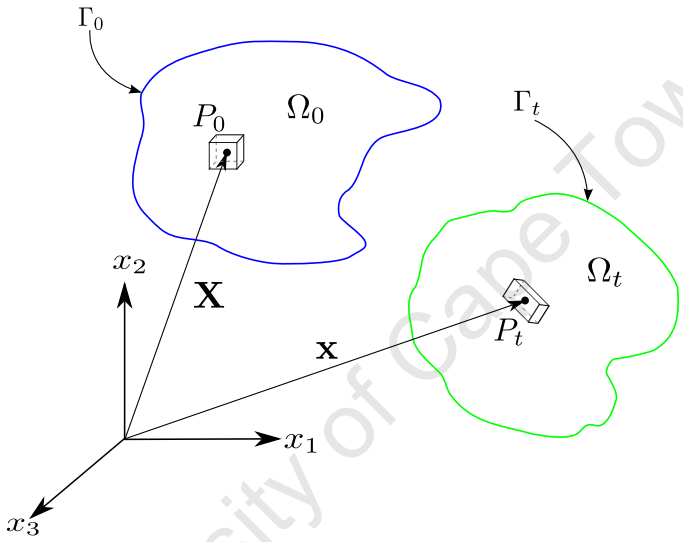

Figure 5.1: Three-dimensional motion of an arbitrary body Ω

The properties of the body can therefore be written either as functions of reference position and time, e.g.

$$\theta = \Theta(\boldsymbol{X}, t), \quad \boldsymbol{v} = \boldsymbol{V}(\boldsymbol{X}, t) \ , \tag{5.4}$$

or current position and time

$$\theta = \bar{\theta}(\boldsymbol{x}, t), \quad \boldsymbol{v} = \tilde{\boldsymbol{v}}(\boldsymbol{x}, t) \ . \tag{5.5}$$

These are known as the Lagrangian (material), and Eulerian (spatial) descriptions of a property.

Material derivative

The rate of change of a property of a material particle, with respect to time, in the material description, is given by

$$\frac{D\Theta}{Dt} = \frac{\partial}{\partial t}\Theta(\boldsymbol{X}, t) \ , \tag{5.6}$$

and in the spatial description by

$$\frac{D\theta}{Dt} = \left.\frac{\partial\theta}{\partial t}\right|_{\boldsymbol{x}} + \boldsymbol{v}\cdot\nabla\theta \ , \tag{5.7}$$

where

$$\nabla(\cdot) = \frac{\partial(\cdot)}{\partial \boldsymbol{x}} \tag{5.8}$$

is the gradient operator with respect to the current configuration. The gradient operator with respect to the reference configuration is denoted by

$$\mathrm{GRAD}(\cdot) = \frac{\partial(\cdot)}{\partial \boldsymbol{X}} \ . \tag{5.9}$$

Velocity and acceleration

The velocity $\boldsymbol{v}$ is the time rate of change of the position of a particle, and acceleration $\boldsymbol{a}$ is the time rate of change of velocity of a particle. The material descriptions of velocity and acceleration are given by

$$\boldsymbol{V} = \frac{D\boldsymbol{x}}{Dt} = \frac{\partial}{\partial t}\hat{\boldsymbol{x}}(\boldsymbol{X}, t) \ , \tag{5.10}$$

$$\boldsymbol{A} = \frac{D\boldsymbol{V}}{Dt} = \frac{\partial}{\partial t}\boldsymbol{V}(\boldsymbol{X}, t) \ , \tag{5.11}$$

and the spatial descriptions by

$$\boldsymbol{v} = \frac{D\boldsymbol{x}}{Dt} \ , \tag{5.12}$$

$$\boldsymbol{a} = \frac{D\boldsymbol{v}}{Dt} = \left.\frac{\partial\boldsymbol{v}}{\partial t}\right|_{\boldsymbol{x}} + (\nabla\boldsymbol{v})\boldsymbol{v} \ . \tag{5.13}$$

Deformation

A body undergoing deformation can be seen in Figure 5.2. The displacement vector, denoted $\boldsymbol{u}$, represents the difference between the current and reference position of a material point:

$$\boldsymbol{u} = \hat{\boldsymbol{x}}(\boldsymbol{X}, t) - \boldsymbol{X} \ . \tag{5.14}$$

The displacement gradient, denoted GRAD $\boldsymbol{u}$, represents the change in displacement vector with respect to the change in the reference position of a particle, and is given in index notation by

$$[\mathrm{GRAD}\ \boldsymbol{u}]_{ij} = \frac{\partial u_i}{\partial X_j} \ . \tag{5.15}$$

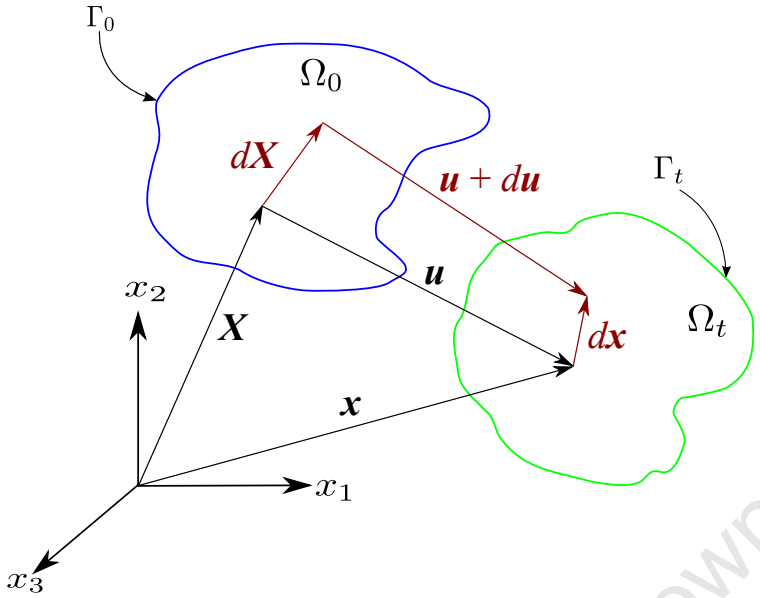

Figure 5.2: A three-dimensional body undergoing deformation

The deformation gradient, $\boldsymbol{F}$, represents the change in the current position of particle with respect to the change in its reference position, and is given by

$$\boldsymbol{F} = \text{GRAD}\ \hat{\boldsymbol{x}}(\boldsymbol{X}, t)\ , \tag{5.16}$$

or in index notation by

$$F_{ij} = \frac{\partial x_i}{\partial X_j}\ . \tag{5.17}$$

It can therefore be shown that

$$d\boldsymbol{x} = \boldsymbol{F} d\boldsymbol{X}\ . \tag{5.18}$$

The deformation gradient can be decomposed into a product of an orthogonal tensor and a positive definite symmetric tensor in the form

$$\boldsymbol{F} = \boldsymbol{R}\boldsymbol{U} = \boldsymbol{V}\boldsymbol{R}\ , \tag{5.19}$$

where $\boldsymbol{R}$ is an orthogonal tensor representing a rotation, $\boldsymbol{U}$ is the right stretch tensor, and $\boldsymbol{V}$ is the left stretch tensor. $\boldsymbol{U}$ and $\boldsymbol{V}$ have the same principal stretches, and principal directions, $\boldsymbol{N}_i$ and $\boldsymbol{n}_i$, respectively, related to each other by

$$\boldsymbol{n}_i = \boldsymbol{R}\boldsymbol{N}_i\ . \tag{5.20}$$

The right Cauchy-Green deformation tensor is defined by

$$\boldsymbol{C} = \boldsymbol{F}^T\boldsymbol{F} = \boldsymbol{U}^2 \ . \tag{5.21}$$

The invariants of the right Cauchy-Green tensor are

$$I_1^{\boldsymbol{C}} = \mathrm{tr}(\boldsymbol{C}) \ , \tag{5.22}$$

$$I_2^{\boldsymbol{C}} = \frac{[(\mathrm{tr}\boldsymbol{C})^2 - \mathrm{tr}(\boldsymbol{C}^2)]}{2} \ , \tag{5.23}$$

$$I_3^{\boldsymbol{C}} = \det(\boldsymbol{C}) \ , \tag{5.24}$$

where $\det \boldsymbol{C}$ is the determinant, and $\mathrm{tr}(\boldsymbol{C})$ is the trace of the tensor $\boldsymbol{C}$, i.e.

$$\mathrm{tr}(\boldsymbol{C}) = C_{ii} \ . \tag{5.25}$$

Incompressible bodies do not undergo any volume change. In this case

$$\det \boldsymbol{F} = 1 \ . \tag{5.26}$$

The left Cauchy-Green deformation tensor can be defined as

$$\boldsymbol{B} = \boldsymbol{F}\boldsymbol{F}^T = \boldsymbol{V}^2 \ . \tag{5.27}$$

The principal stretches (or eigenvalues) λ_i, can be obtained from the spectral decompositions of $\boldsymbol{C}$ by

$$\boldsymbol{C} = \sum_{i=1}^{3} \lambda_i^2 \boldsymbol{N}_i \otimes \boldsymbol{N}_i \ , \tag{5.28}$$

and from $\boldsymbol{B}$ by

$$\boldsymbol{B} = \sum_{i=1}^{3} \lambda_i^2 \boldsymbol{n}_i \otimes \boldsymbol{n}_i \ . \tag{5.29}$$

They can also be obtained from the stretch tensors, $\boldsymbol{U}$ by

$$\boldsymbol{U} = \sum_{i=1}^{3} \lambda_i \boldsymbol{N}_i \otimes \boldsymbol{N}_i \ , \tag{5.30}$$

and $\boldsymbol{V}$ by

$$\boldsymbol{V} = \sum_{i=1}^{3} \lambda_i \boldsymbol{n}_i \otimes \boldsymbol{n}_i \ . \tag{5.31}$$

where $\boldsymbol{N}_i$ and $\boldsymbol{n}_i$ are eigenvectors in each respective case.

For small strains,

$$|d\boldsymbol{u}| << |d\boldsymbol{X}| \ , \tag{5.32}$$

so that

$$|\nabla \boldsymbol{u}| << 1 \ . \tag{5.33}$$

Hence

$$\left|(\nabla \boldsymbol{u})^T (\nabla \boldsymbol{u})\right| << |\nabla \boldsymbol{u}| \ , \tag{5.34}$$

and

$$\boldsymbol{F}^T \boldsymbol{F} = \boldsymbol{I} + 2\boldsymbol{E} \simeq \boldsymbol{I} + \nabla \boldsymbol{u} + (\nabla \boldsymbol{u})^T \ , \tag{5.35}$$

where, for small strains, the Lagrangian finite strain tensor, denoted $\boldsymbol{E}$, is approximated by the infinitesimal strain tensor $\boldsymbol{\varepsilon}$, where

$$\boldsymbol{\varepsilon} = \frac{1}{2}\left(\nabla \boldsymbol{u} + (\nabla \boldsymbol{u})^T\right) \ . \tag{5.36}$$

Since $\boldsymbol{\varepsilon}$ is symmetric, it has three eigenvalues, ε_i and three corresponding mutually orthogonal eigenvectors, $\boldsymbol{n}_i$. Consider three line elements that emanate from the same point and which are orientated in the principal directions, so that they define a parallelepiped of rectangular shape with volume

$$dV = dS_1 \, dS_2 \, dS_3 \ . \tag{5.37}$$

If ε_i are the principal strains, the change in volume is

$$\Delta(dV) = (1+\varepsilon_1) dS_1 \, (1+\varepsilon_2) dS_2 \, (1+\varepsilon_3) dS_3 - dV \ , \tag{5.38}$$

giving

$$\Delta(dV) = (\varepsilon_1 + \varepsilon_2 + \varepsilon_3) dV + \text{higher order terms} \ . \tag{5.39}$$

For small strains, volume change or dilatation is given by

$$e = \frac{\Delta(dV)}{dV} = \varepsilon_{ii} = \frac{\partial u_i}{\partial X_i} = \operatorname{div} \boldsymbol{u} \ . \tag{5.40}$$

5.1.2 Stress

Consider an arbitrary body and a volume dV located at a material point, P (Figure (5.3)). A traction force $\boldsymbol{t}$ and body force $\boldsymbol{b}$ acts on this body. The body force, $\boldsymbol{b}$, acts throughout the body and has the units of force per unit mass. The surface traction, $\boldsymbol{t}$, acts over any surface of the body and has units of force per unit area.

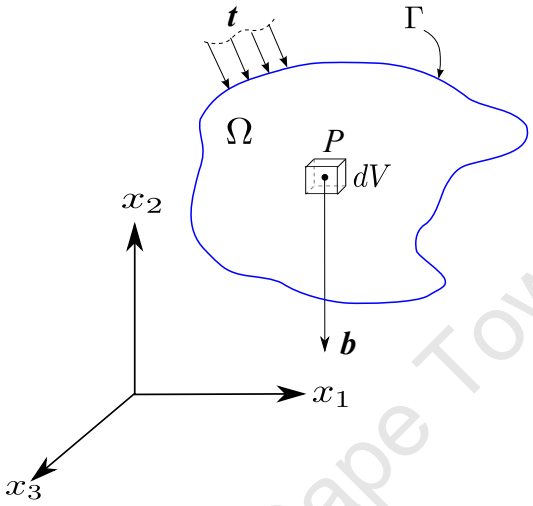

Figure 5.3: Arbitrary body with infinitesimal particle P with a volume dV. A traction $\boldsymbol{t}$ and body force $\boldsymbol{b}$ acts on this body.

Consider the free body created by cutting a body, Ω, along a plane passing through point P as in Figure 5.4.

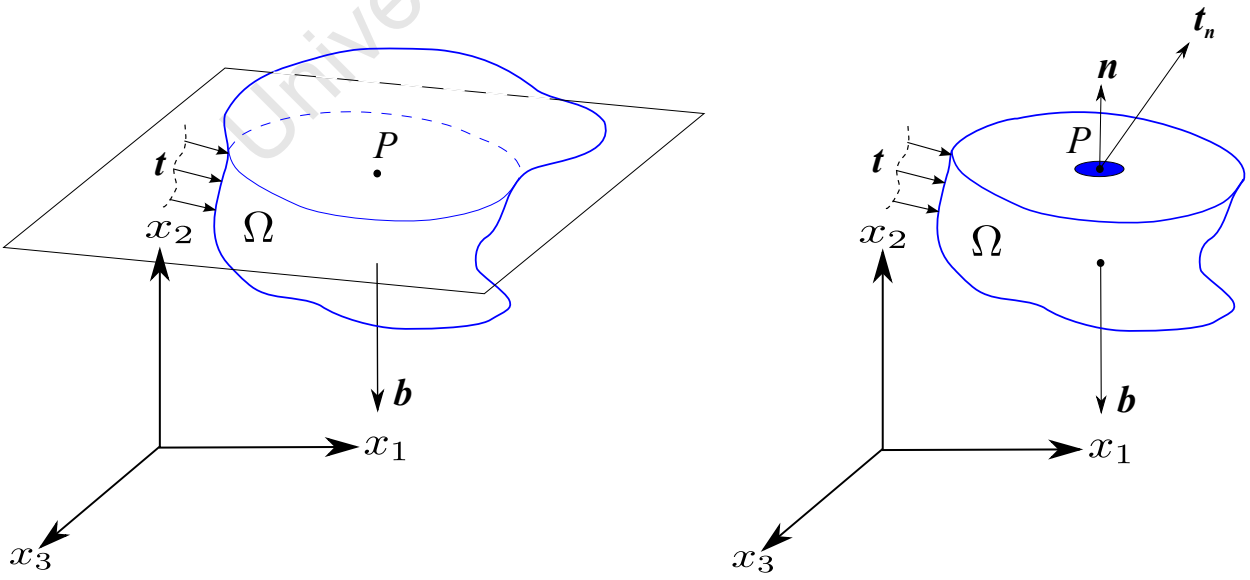

(a) Free body Ω before planar cut.

(b) Free body Ω after planar cut.

Figure 5.4: Free body with planar cut through point P.

The traction on the cut surface is referred to as the Cauchy stress vector, and is defined as

$$\boldsymbol{t_n} = \lim_{\Delta A \to 0} \frac{\Delta \boldsymbol{F}}{\Delta A} \ , \tag{5.41}$$

where $\Delta \boldsymbol{F}$ is the force acting on area, ΔA, with normal vector, $\boldsymbol{n}$, at point, P.

According to Cauchy's theorem, the stress vector $\boldsymbol{t_n}$ at any point in the continuum, associated with a plane with normal $\boldsymbol{n}$, can be obtained from the Cauchy stress tensor by

$$\boldsymbol{t_n} = \boldsymbol{\sigma n} \ . \tag{5.42}$$

5.1.3 Cauchy's equation of motion

Cauchy's equation of motion for the balance of linear momentum is given by

$$\text{div}\boldsymbol{\sigma} + \rho \boldsymbol{b} = \rho \boldsymbol{a} \tag{5.43}$$

or, in index form,

$$\frac{\partial \sigma_{ij}}{\partial x_i} + \rho b_i = \rho a_i \ . \tag{5.44}$$

Balance of angular momentum requires that the Cauchy stress tensor be symmetric:

$$\boldsymbol{\sigma}^T = \boldsymbol{\sigma} \quad \text{or} \quad \sigma_{ij} = \sigma_{ji} \ . \tag{5.45}$$

For small strains

$$\frac{\partial u_i}{\partial x_j} \simeq \frac{\partial u_i}{\partial X_j} \ . \tag{5.46}$$

Since displacements are small, the velocities are also small and consequently the Lagrangian and Eulerian descriptions of acceleration are approximately equal:

$$a_i = \left.\frac{\partial^2 u_i}{\partial t^2}\right|_{\boldsymbol{X}} \simeq \left.\frac{\partial^2 u_i}{\partial t^2}\right|_{\boldsymbol{x}}, \quad v_i = \frac{Du_i}{Dt} \ . \tag{5.47}$$

The differential volume (dV) is related to the original volume (dV_0) by

$$dV = (1 + \varepsilon_{kk}) dV_0 \ , \tag{5.48}$$

therefore

$$\rho = (1 + \varepsilon_{kk})^{-1} \rho_0 \ . \tag{5.49}$$

Since $\boldsymbol{\varepsilon}_{kk} << 1$, the density can be treated as constant:

$$\rho \simeq \rho_0 \ . \tag{5.50}$$

From equations (5.46), (5.47), and (5.49) it can be seen that in the case of small strains, spatial and material coordinates are equivalent. Cauchy's equation ((5.44)) thus reduces to

$$\frac{\partial \sigma_{ji}}{\partial x_j} + \rho b_i = \rho \frac{\partial^2 u_i}{\partial t^2} \ . \tag{5.51}$$

If the body is in equilibrium, there is no resultant acceleration, and Cauchy's equation reduces to

$$\frac{\partial \sigma_{ji}}{\partial x_j} + \rho b_i = 0 \ . \tag{5.52}$$

Solutions of problems in elasticity

Problems in elasticity are concerned with obtaining solutions for the 15 unknowns u_i, ε_{ij} and σ_{ij}, which are related by the 15 equations, 3 equations from Cauchy's equation (5.51), 6 independent equations from the constitutive equation and a further 6 independent equations from (5.36). To solve these equations it is necessary to take account of the initial conditions, and the boundary conditions.

Boundary conditions have two forms, namely Dirichlet, or Neumann conditions:
Dirichlet boundary conditions involve prescribed displacements: i.e.,

$$\boldsymbol{u} = \bar{\boldsymbol{u}} \text{ on } \Gamma \ . \tag{5.53}$$

Neumann boundary conditions involve prescribed tractions:

$$\boldsymbol{t_n} = \boldsymbol{\sigma n} = \bar{\boldsymbol{t}} \text{ on } \Gamma \ . \tag{5.54}$$

Note that either a displacement or traction must be specified for each point on the boundary but not both.

Initial conditions are given by

$$\boldsymbol{u}(\boldsymbol{x}, 0) \quad \text{and} \quad \frac{\partial \boldsymbol{u}}{\partial t}(\boldsymbol{x}, 0) \ . \tag{5.55}$$

Note that $t = 0$ and that initial accelerations need not be specified.

5.1.4 Linear Elasticity

A body undergoing a deformation can be considered to be linear elastic solid if:

- the relationship between stress and strain is linear
- the deformation is rate-independent and path-independent
- body returns to original configuration after load is removed.

These requirements are met by

$$\boldsymbol{\sigma} = \boldsymbol{\sigma}(\boldsymbol{\varepsilon}), \quad \boldsymbol{\sigma}(\mathbf{0}) = \mathbf{0} \ , \tag{5.56}$$

where $\boldsymbol{\sigma}$ is the Cauchy stress tensor and $\boldsymbol{\varepsilon}$ is the infinitesimal strain tensor. Since $\boldsymbol{\sigma}$ is related linearly to $\boldsymbol{\varepsilon}$, (5.56) becomes

$$\sigma_{ij} = \mathbb{C}_{ijkl}\, \varepsilon_{kl} \ , \tag{5.57}$$

where $\mathbb{C}_{ijkl}$ is the fourth order elasticity tensor.

In general, $\mathbb{C}_{ijkl}$ has 81 elements, but not all of them are independent. The symmetry of the strain tensor gives

$$\mathbb{C}_{ijkl} = \mathbb{C}_{ijlk} \ . \tag{5.58}$$

This reduces the number of independent elements to 54. From the symmetry of the stress tensor,

$$\mathbb{C}_{ijkl} = \mathbb{C}_{jilk} \ , \tag{5.59}$$

and the number of independent elements reduce to 36.

If we assume the existence of a strain energy function

$$U = \frac{1}{2}\mathbb{C}_{ijkl}\, \varepsilon_{ij}\, \varepsilon_{kl} \tag{5.60}$$

with $\sigma_{ij} = \dfrac{\partial U}{\partial \varepsilon_{ij}}$, then

$$\mathbb{C}_{ijkl} = \frac{\partial \sigma_{ij}}{\partial \varepsilon_{kl}} = \frac{\partial^2 U}{\partial \varepsilon_{kl} \partial \varepsilon_{ij}} = \frac{\partial^2 U}{\partial \varepsilon_{ij} \partial \varepsilon_{kl}} = \frac{\partial \sigma_{kl}}{\partial \varepsilon_{ij}} = \mathbb{C}_{klij} \ . \tag{5.61}$$

This reduces the number of independent elements to 21.

Linear isotropic elastic solid

A body is homogeneous if its properties do not depend on position. A body is isotropic if its material properties are independent of direction. A linear elastic solid is isotropic if its elasticity tensor remains the same under a transformation:

$$\mathbb{C}'_{ijkl} = \mathbb{C}_{ijkl} \ . \tag{5.62}$$

In this case, $\mathbb{C}_{ijkl}$ is known as an isotropic tensor, and it can be shown that

$$\sigma_{ij} = \mathbb{C}_{ijkl}\varepsilon_{kl} = \lambda\varepsilon_{kk}\delta_{ij} + 2\mu\boldsymbol{\varepsilon}_{ij} \ , \tag{5.63}$$

where the coefficients λ and μ are called Lamé constants.

Young's Modulus and Poisson's ratio

Equation (5.63) can be inverted to obtain

$$\varepsilon_{ij} = \frac{1}{2\mu}\left[\sigma_{ij} - \frac{\lambda}{3\lambda + 2\mu}\sigma_{kk}\delta_{ij}\right] \ . \tag{5.64}$$

Consider a uniaxial stress state where all the elements of $\boldsymbol{\sigma}$, except for σ_{11} are zero. The strains are therefore given by

$$\varepsilon_{11} = \frac{\lambda + \mu}{\mu(3\lambda + 2\mu)}\sigma_{11} \ , \tag{5.65}$$

$$\varepsilon_{22} = \varepsilon_{33} = -\frac{\lambda}{2(\lambda + \mu)}\varepsilon_{11} \ , \tag{5.66}$$

$$\varepsilon_{12} = \varepsilon_{13} = \varepsilon_{23} = 0 \ . \tag{5.67}$$

It can be seen that the ratio of axial stress to axial strain is given by

$$E = \frac{\sigma_{11}}{\varepsilon_{11}} = \frac{\mu(3\lambda + 2\mu)}{\lambda + \mu} \ . \tag{5.68}$$

The quantity E is commonly referred to as Young's modulus or the modulus of elasticity. Furthermore the negative of the ratio of the transverse strain to the axial strain is:

$$\nu = -\frac{\varepsilon_{22}}{\varepsilon_{11}} = -\frac{\varepsilon_{33}}{\varepsilon_{11}} = \frac{\lambda}{2(\lambda + \mu)} \tag{5.69}$$

The quantity ν is the called Poisson's ratio.

Consider a simple shear stress state where all the elements of $\boldsymbol{\sigma}$ are zero, except for $\sigma_{12} = \sigma_{21} = \tau$. From (5.64)

$$\varepsilon_{12} = \varepsilon_{21} = \frac{\tau}{2\mu} \ . \tag{5.70}$$

The quantity $G = \mu$ is called the shear modulus, and in terms of E and ν, is given by

$$G = \mu = \frac{\tau}{\gamma} = \frac{E}{2(1+\nu)} \ . \tag{5.71}$$

Using (5.68) and (5.69), equation (5.64) can be rewritten as

$$\varepsilon_{ij} = \frac{1}{E}\left[(1+\nu)\sigma_{ij} - \nu\sigma_{kk}\delta_{ij}\right] \ , \tag{5.72}$$

and the inverse of this is

$$\sigma_{ij} = \frac{E}{1+\nu}\left[\varepsilon_{ij} + \frac{\nu}{1-2\nu}\varepsilon_{kk}\delta_{ij}\right] \ . \tag{5.73}$$

Isotropic elasticity tensor

Voigt notation is simply a way of writing the components of a symmetric tensor in vector form. For example, in the linear elastic relationship in (5.57), each term is converted to Voigt notation as follows:

$$\sigma_{ij} \Rightarrow \begin{bmatrix} \sigma_{11} & \sigma_{22} & \sigma_{33} & \sigma_{12} & \sigma_{23} & \sigma_{13} \end{bmatrix}^T \ , \tag{5.74}$$

$$\mathbb{C}_{ijkl} \Rightarrow \begin{bmatrix} \mathbb{C}_{1111} & \mathbb{C}_{1122} & \mathbb{C}_{1133} & \sqrt{2}\mathbb{C}_{1112} & \sqrt{2}\mathbb{C}_{1123} & \sqrt{2}\mathbb{C}_{1113} \\ \mathbb{C}_{2211} & \mathbb{C}_{2222} & \mathbb{C}_{2233} & \sqrt{2}\mathbb{C}_{2211} & \sqrt{2}\mathbb{C}_{2223} & \sqrt{2}\mathbb{C}_{2213} \\ \mathbb{C}_{3311} & \mathbb{C}_{3322} & \mathbb{C}_{3333} & \sqrt{2}\mathbb{C}_{3312} & \sqrt{2}\mathbb{C}_{3323} & \sqrt{2}\mathbb{C}_{3313} \\ \sqrt{2}\mathbb{C}_{1211} & \sqrt{2}\mathbb{C}_{1222} & \sqrt{2}\mathbb{C}_{1233} & 2\mathbb{C}_{1212} & 2\mathbb{C}_{1223} & 2\mathbb{C}_{1213} \\ \sqrt{2}\mathbb{C}_{2311} & \sqrt{2}\mathbb{C}_{2322} & \sqrt{2}\mathbb{C}_{2333} & 2\mathbb{C}_{2312} & 2\mathbb{C}_{2323} & 2\mathbb{C}_{2313} \\ \sqrt{2}\mathbb{C}_{1311} & \sqrt{2}\mathbb{C}_{1322} & \sqrt{2}\mathbb{C}_{1333} & 2\mathbb{C}_{1312} & 2\mathbb{C}_{1323} & 2\mathbb{C}_{1313} \end{bmatrix} \ , \tag{5.75}$$

$$\varepsilon_{kl} \Rightarrow \begin{bmatrix} \varepsilon_{11} & \varepsilon_{22} & \varepsilon_{33} & 2\varepsilon_{12} & 2\varepsilon_{23} & 2\varepsilon_{13} \end{bmatrix}^T \ . \tag{5.76}$$

Thus, the isotropic elasticity tensor in Voigt notation is given by

$$\mathbb{C}_{ij} = \begin{bmatrix} \mathbb{C}_{11} & \mathbb{C}_{12} & \mathbb{C}_{12} & 0 & 0 & 0 \\ \mathbb{C}_{12} & \mathbb{C}_{11} & \mathbb{C}_{12} & 0 & 0 & 0 \\ \mathbb{C}_{12} & \mathbb{C}_{12} & \mathbb{C}_{11} & 0 & 0 & 0 \\ 0 & 0 & 0 & \mathbb{C}_{44} & 0 & 0 \\ 0 & 0 & 0 & 0 & \mathbb{C}_{44} & 0 \\ 0 & 0 & 0 & 0 & 0 & \mathbb{C}_{44} \end{bmatrix} \ , \tag{5.77}$$

where

$$\mathbb{C}_{11} = \frac{E(1-\nu)}{(1+\nu)(1-2\,\nu)} \ , \tag{5.78}$$

$$\mathbb{C}_{12} = \frac{E(\nu)}{(1+\nu)(1-2\,\nu)} \ , \tag{5.79}$$

$$G = \mu = (\mathbb{C}_{11} - \mathbb{C}_{12})/2 \ , \tag{5.80}$$

$$\mathbb{C}_{44} = 2\,G \ . \tag{5.81}$$

5.1.5 Transverse isotropy

The muscle fibres introduce directionality into the material properties and the material should be treated as transversely isotropic. Let $\boldsymbol{N}$ be the unit vector in the direction of the muscle fibre in the reference configuration; $\boldsymbol{n}$ is the unit vector in the direction of a muscle fibre in the current configuration. These are related by

$$\boldsymbol{F}\boldsymbol{N} = \lambda_f\,\boldsymbol{n} \ . \tag{5.82}$$

$\boldsymbol{F}$ thus transforms $\boldsymbol{N}$, stretching it by λ_f, and rotating it to the new orientation $\boldsymbol{n}$. From (5.82), it is seen that

$$\lambda_f = \sqrt{\boldsymbol{N}\cdot\boldsymbol{C}\boldsymbol{N}} \ . \tag{5.83}$$

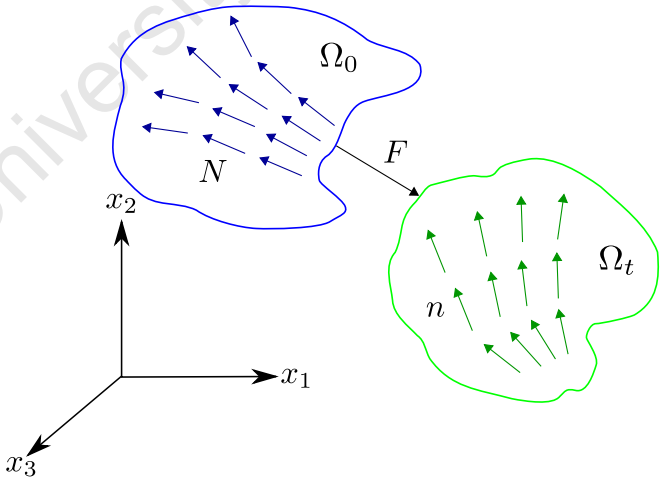

Figure 5.5: Transformation of material fibres through deformation.

The invariants of the right Cauchy-Green tensor which involve the material fibres are

$$I_4^{\boldsymbol{C}} = \boldsymbol{N}\cdot\boldsymbol{C}\boldsymbol{N} \ , \tag{5.84}$$

$$I_5^{\boldsymbol{C}} = \boldsymbol{N}\cdot\boldsymbol{C}^2\boldsymbol{N} \ . \tag{5.85}$$

5.2 Constitutive model for skeletal muscle

There is a long history in the development of constitutive muscle models. One of the most important works on muscle models is that of Hill [53]. The main alternative to Hill's model is the Distribution Moment (DM) model [23]. Most later muscle models are based on either the Hill or the DM model. The Hill model is a phenomenonological model based on physical observations, whereas the DM model is based on cross-bridge theory of muscle contraction. There are other phenomenological models in literature, but the focus for this section will be on Hill's model [3, 11, 40, 46, 51, 105, 138].

Hill's model is discussed in further detail in this chapter. A muscle model recently developed by Martins [88, 89], based on the Hill model, will also be discussed. To conclude this chapter, a linearized version of Martins' model is presented and discussed.

5.2.1 Hill's muscle model

The classical Hill's muscle model consists of three components, each representing a specific component of a muscle sarcomere (see 3.4 for more detail on muscle structure). A sarcomere is considered to be a unit cell of a myofibril, and it falls into the microscopic scale (order of μm). It is also considered to be the basic contractile unit of muscle tissue. For this reason, Hill's model is classified as a micro-scale model of muscle behaviour. The sarcomeres are arranged in series and parallel to each other, forming the myofibril. It is assumed that the microscopic behaviour of each cell contributes similarly, and hence, the behaviour of the overall collection of cells, i.e. the muscle fibres, behave similarly to its sarcomeres. Thus, it is assumed that the microscopic framework of the muscle model developed by Hill can be applied on a macroscopic level (illustrated in Figure 5.6).

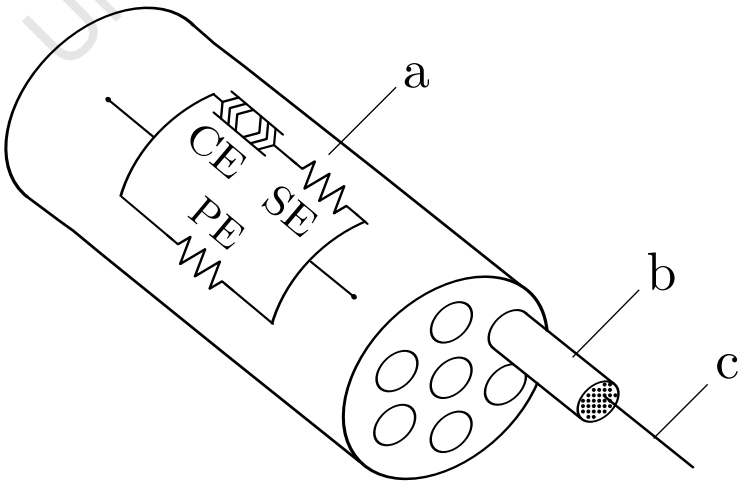

Figure 5.6: Illustration of Hill-type muscle fibre. (a) muscle fibre, (b) myofibril, (c) muscle filament

The three components of Hill's model are the contractile element (CE) and series element (SE), in series with each other, and the parallel element (PE), parallel to the first two (figure 5.7). This model has been widely used by many including Kojic [74], Martins [88], Pandy [106], and Van Loocke [128, 129, 130], to name a few.

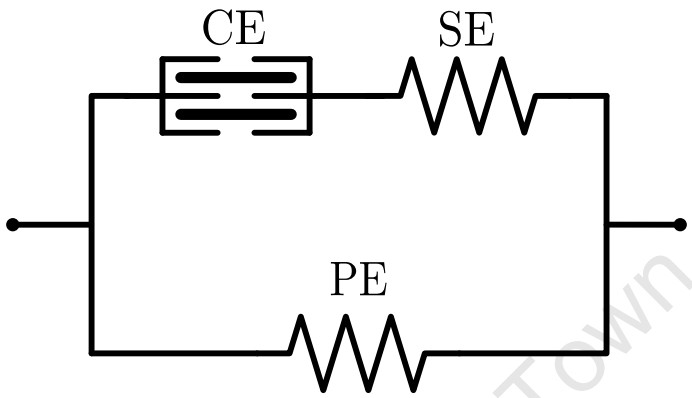

Figure 5.7: Classical Hill-type muscle model. SE-Series element, CE-Contractile element, PE-Parallel element

A few alternatives to the classical Hill model have been suggested. In one arrangement (5.8(a)), the PE and CE are in parallel, with the SE in series to the combination of the first two. This type of muscle model has been used in the works of Zahalak [141, 142], Cole [23] and Van den Bogert [127]. Another model suggested by Zulliger [148] has all three components in parallel with each other (5.8(b)). An early study comparing some of these models was done by Brady [13].

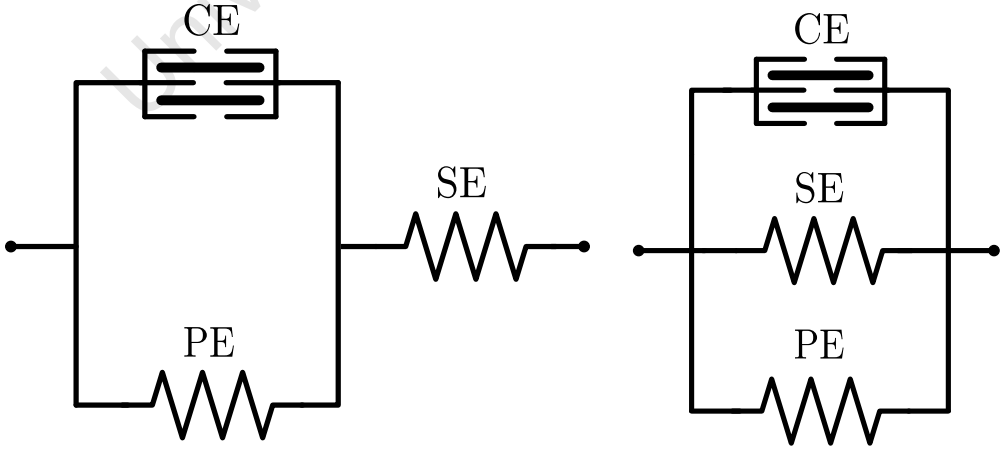

(a) Alternative one, to the classic Hill-type muscle model

(b) Alternative two, to the classic Hill-type muscle model

Figure 5.8: Alternatives to the classic Hill-type muscle model. SE-series element, CE-contractile element, PE-parallel element

A detailed breakdown of the muscle structure can be seen in Figure 3.14, and definitions of its components are given in Chapter 3. Each element in both types of models represents a physical component of the muscle tissue:

- PE - connective tissues (epymisium, perimesium and endomesium) and also the sarcolemma
- SE - elastic components of sarcomere (myofilaments and cross-bridges)
- CE - active contractile components, i.e. sliding actin-myosin filaments, the active force generated is directly related to the number of active cross-bridges between the filaments.

Another more simplistic muscle model is suggested in the works of Cole [23], and Malhotra [83]. In this model the parallel element is assumed to be insignificant, and is omitted completely. It has the CE in series with the SE (see Figure 5.9).

Figure 5.9: Alternative to Hill-type muscle model. SE-series element, CE-contractile element

The classical Hill muscle model is modified by taking the surrounding isotropic ground material into account as illustrated in Figure 5.10. The isotropic part is three-dimensional, whereas the fibre parts are one-dimensional in the fibre direction. This is the muscle model selected for the linearized muscle model (LMM) discussed later in this Chapter.

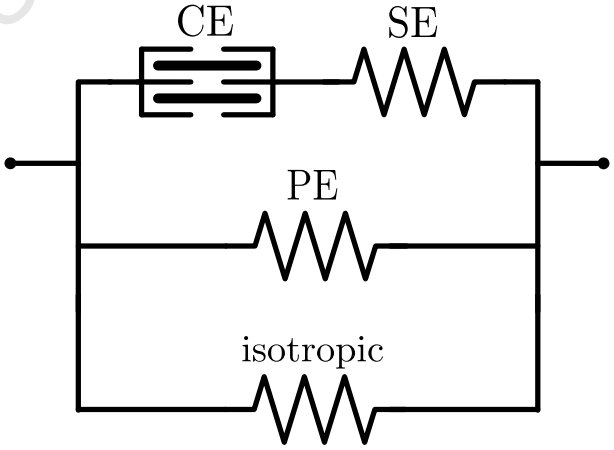

Figure 5.10: Hill-type muscle model with isotropic component.

5.2.2 Martins' muscle model

What makes muscle tissue different from other biological soft tissue is its ability to contract actively (by neural stimulation) [42, 113]. Martins presents a numerical model of this active behaviour of skeletal muscle, as well as the passive behaviour [28, 88, 89]. The passive behaviour of muscle tissue has the same properties of other biological soft tissues. An example of typical active and passive stress-strain behaviour for muscle tissue is illustrated in Figure 5.11. The activation process involves highly complex electrical and chemical signals between neural and muscular components. This activation process itself is not directly modelled, but instead, a neural stimulus is taken as an input and driver to the contraction process in this model.

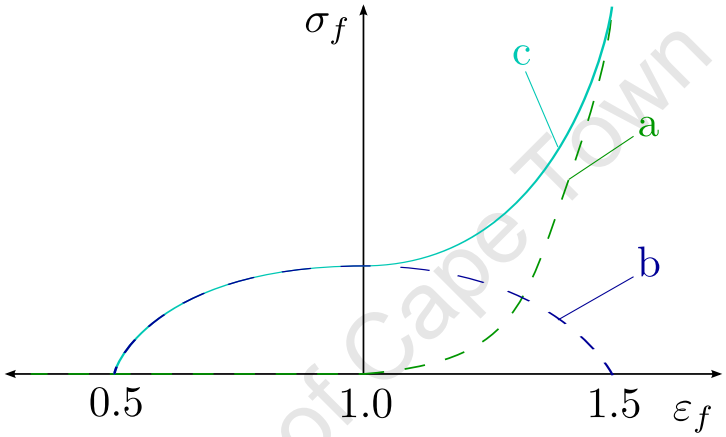

Figure 5.11: General muscle fibre stress-strain relationship. (a) purely passive behaviour, (b) purely active behaviour, (c) actual behaviour (combination of active and passive)

Active contraction of muscle tissue causes a reduction in length, and this produces tensile forces (stress) within the material. The muscle activation function used by Martins is that due to Pandy and Zajac for skeletal muscle contraction [106, 143].

In general, biological soft tissues, including muscle tissue, exhibit highly non-linear mechanical behaviour and are thus treated as hyperelastic. Like other biological soft tissue, muscle tissue is also treated as incompressible. Furthermore, due to the inherent presence of muscle fibres in the tissue, it is considered anisotropic. To be more specific, muscle tissue is transversely isotropic in the direction of the muscle fibres [42, 113]. The constitutive equation adopted for this model is a modified form of the incompressible transversely isotropic hyperelastic model proposed by Humphrey and Yin [64, 65] for passive cardiac tissue.

The classical one-dimensional Hill type model (Figure 5.7) is used as a basis for this work. The three-dimensional model is consistent with the one-dimensional model used by Hill [53], Huxley [66] and Zajac [143].

We present here a description of the model. The one-dimensional longitudinal muscle stress (in the direction of fibres) is the sum of the stresses in the SE and PE i.e.,

$$T = T_p + T_s \ . \tag{5.86}$$

The stress in the CE is equal to the stress in the SE:

$$T_c = T_s \ . \tag{5.87}$$

The stress in muscle tissue can be described with the general constitutive equation for fibre-reinforced composites with transversely isotropic material symmetry and incompressible, or nearly incompressible behaviour. This model follows from the works of Flory [38], Simo [118] and Spencer [120], and have been used by many authors, including Humphrey [63, 62, 64, 65] and Weiss [135]. The total stress is given by

$$\boldsymbol{\sigma} = \boldsymbol{\sigma}_J + \boldsymbol{\sigma}_m + \boldsymbol{\sigma}_f \ , \tag{5.88}$$

where $\boldsymbol{\sigma}_J$ is the incompressible component, i.e.,

$$\boldsymbol{\sigma}_J = -p\boldsymbol{I} \ , \tag{5.89}$$

where p is the hydrostatic pressure and $\boldsymbol{I}$ is the identity tensor.

For the quasi-incompressible case $\boldsymbol{\sigma}_J$ has the form

$$\boldsymbol{\sigma}_J = \frac{1}{D}\frac{dU_J}{dJ}\boldsymbol{I} \ , \tag{5.90}$$

where D is an incompressibility constant, U_J is an energy function used to penalize the volume change and prevent material collapse, and $J = \det(\boldsymbol{F})$ is the Jacobian ($J = 1$ for incompressibility).

The terms $\boldsymbol{\sigma}_m$ and $\boldsymbol{\sigma}_f$ in equation (5.88) may be combined and written as $\boldsymbol{\sigma}_{isochoric}$. In the incompressible transversely isotropic case, this stress, $\boldsymbol{\sigma}_{isochoric}$ is derived from a strain energy function (SEF) that depends on four invariants of the right Cauchy-Green strain tensor, $\boldsymbol{C}$. The invariants are given in (5.22).

The isotropic matrix $\boldsymbol{\sigma}_m$ in equation (5.88) is given by

$$\boldsymbol{\sigma}_m = 2\,bc\,\exp[b\,(\boldsymbol{I}_1^C - 3)]\,\mathrm{dev}[\boldsymbol{B}] \ , \tag{5.91}$$

where b and c are constants and $\boldsymbol{B}$ is the left Cauchy-Green tensor given in (5.27), and the deviatoric operator is given by

$$\mathrm{dev}[\cdot] = (\cdot) - \frac{1}{3}\mathrm{tr}(\cdot)\boldsymbol{I} \ . \tag{5.92}$$

The term $\boldsymbol{\sigma}_f$ denotes the stress in the fibre i.e.,

$$\boldsymbol{\sigma}_f = \text{dev}[\lambda_f T \boldsymbol{n} \otimes \boldsymbol{n}] \ , \tag{5.93}$$

where λ_f is the stretch ratio of the muscle fibres, and is given by (5.83), the scalar T (see (5.86)) is the stress in the fibre, and the unit vector in the direction of the muscle fibre in the current configuration ($\boldsymbol{n}$) can be found from (5.82) from

$$\boldsymbol{n} = \frac{\boldsymbol{F}\boldsymbol{N}}{\lambda_f} \ . \tag{5.94}$$

The fibre stretch (λ_f) may be split, multiplicatively, to give the contractile (λ_c) and series (λ_s) stretches, so that

$$\lambda_f = \lambda_s \lambda_c \ . \tag{5.95}$$

An initial fibre length L_0, a deformed fibre length due to actin-myosin contraction L^c, and final length due to elastic deformation of fibres L, the stretches are defined as

$$\lambda_f = \frac{L}{L_0}, \quad \lambda_c = \frac{L^c}{L_0}, \quad \lambda_s = \frac{L}{L^c} \ . \tag{5.96}$$

This multiplicative split of the stretches has an advantage over the additive split method, commonly used in biomechanics, in that it does not require information on the partition of the initial fibre length between the CE and SE.

The relationship between T_p in (5.86) and λ_f in the PE, can be seen in Figure 5.12. The stress in the PE is given by

$$T_p(\lambda_f) = T_0 \, f_p(\lambda_f) \ , \tag{5.97}$$

where

$$f_p(\lambda_f) = \begin{cases} 2aA \exp\left[a(\lambda_f - 1)^2\right](\lambda_f - 1), & \lambda_f > 1 \\ 0, & \text{otherwise} \ , \end{cases} \tag{5.98}$$

where T_0, a and A are constants.

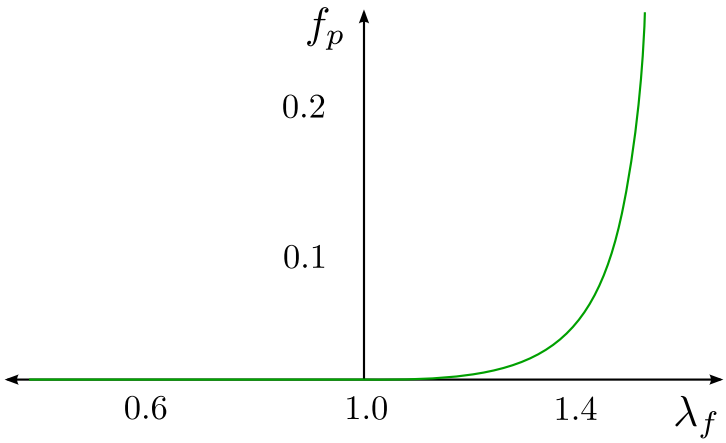

Figure 5.12: Passive force-length relation of muscle tissue for $a = 12.43$ and $A = 8.568 \times 10^{-4}$ in Equation (5.98) [88].

The relationship between T_s in (5.86) and λ_s in the SE, can be seen in Figure 5.13. The stress in the SE is given by

$$T_s(\lambda_s, \lambda_c) = T_0 \, f_s(\lambda_s, \lambda_c) \, , \tag{5.99}$$

where

$$f_s(\lambda_s, \lambda_c) = \begin{cases} 0.1\{\exp\left[100\lambda_c(\lambda_s - 1)\right] - 1]\}, & \lambda_s \geq 1 \\ 0, & \text{otherwise} \end{cases} \tag{5.100}$$

It should be noted that functions in Equations (5.97) and (5.99) can only be non-negative, as the fibres can only work in tension, not in compression.

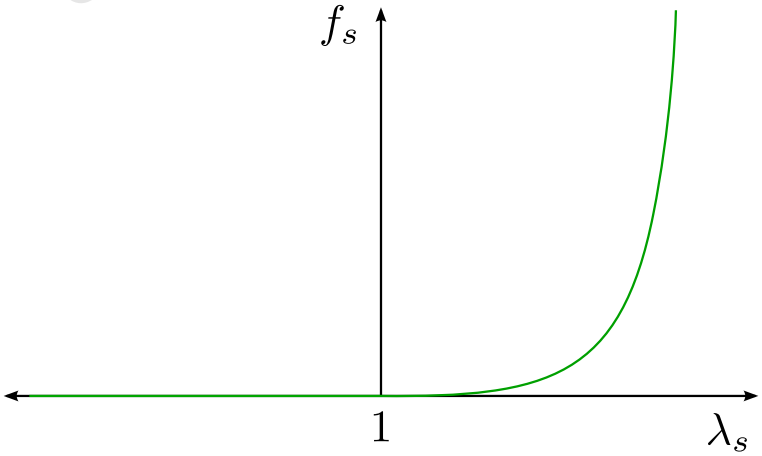

Figure 5.13: Relationship between f_s and λ_s in the SE for fixed λ_c.

The relationship between stress, T_c and strain-rate, $\dot{\lambda}_c$ in the CE, and between the stress, T_c and strain, λ_c, are given by

$$T_c(\lambda_c, \dot{\lambda}_c, \alpha) = T_0 \, f_c^l(\lambda_c) \, f_c^v(\dot{\lambda}_c) \, \alpha(t) \ , \tag{5.101}$$

where

$$f_c^l(\lambda_c) = \begin{cases} (-4(\lambda_c - 1)^2 + 1), & 0.5 \leq \lambda_c \leq 1.5 \\ 0, & \text{otherwise} \ , \end{cases} \tag{5.102}$$

and

$$f_c^v(\dot{\lambda}_c) = \begin{cases} 0, & \dot{\lambda}_c < -10 \\ -\dfrac{1}{\arctan(5)} \arctan(-0.5\dot{\lambda}_c) + 1, & -10 \leq \dot{\lambda}_c \leq 2 \\ \dfrac{\pi}{4 \arctan(5)} + 1, & \dot{\lambda}_c > 2 \ . \end{cases} \tag{5.103}$$

These relationships for the CE are illustrated in Figure 5.14.

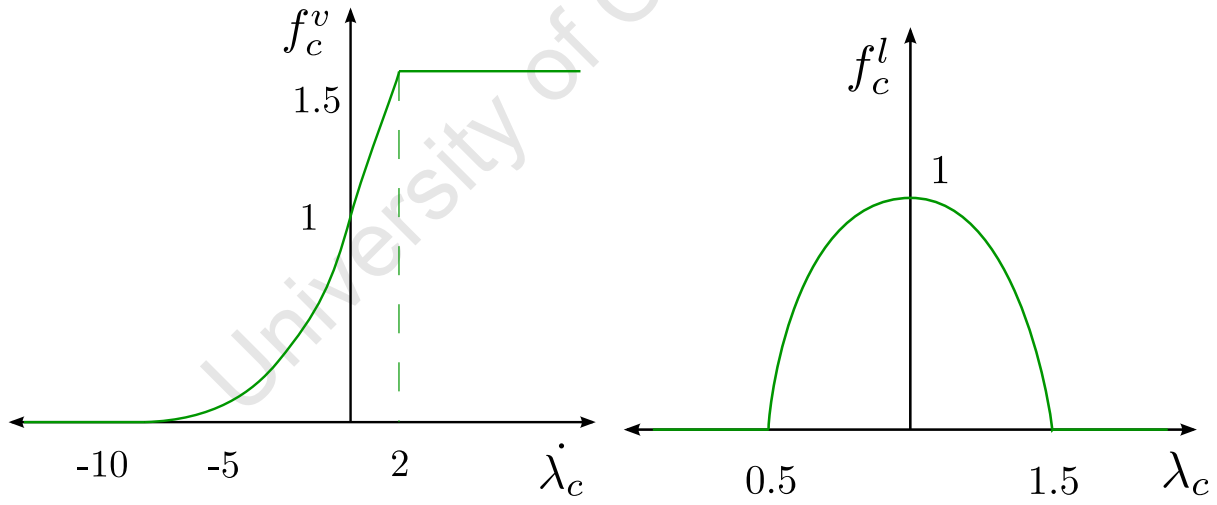

(a) Force-velocity relation of fully activated muscle tissue when CE is at optimal length

(b) Force-length relation of muscle tissue due to an active force

Figure 5.14: Force-velocity and force-length relations for CE [88].

The time-dependent activation function illustrated in Figure 5.15 is given by the solution to the first-order differential equation used by Pandy and Zajac et. al. [106, 143],

$$\dot{\alpha}(t, u) = \frac{1}{\tau_{rise}}(1 - \alpha(t))u(t) + \frac{1}{\tau_{fall}}(\alpha_{min} - \alpha(t))(1 - u(t)) \ , \tag{5.104}$$

where τ_{rise} and τ_{fall} are time constants for activation and deactivation of the muscle, α_{min} is the minimum value of the activation, and $u(t)$ is the neural excitation as a function of time, ranging from 0 to 1, given by

$$u(t) = \begin{cases} 1, & 0 < t \leq 1 \\ 0, & \text{otherwise} \end{cases} \tag{5.105}$$

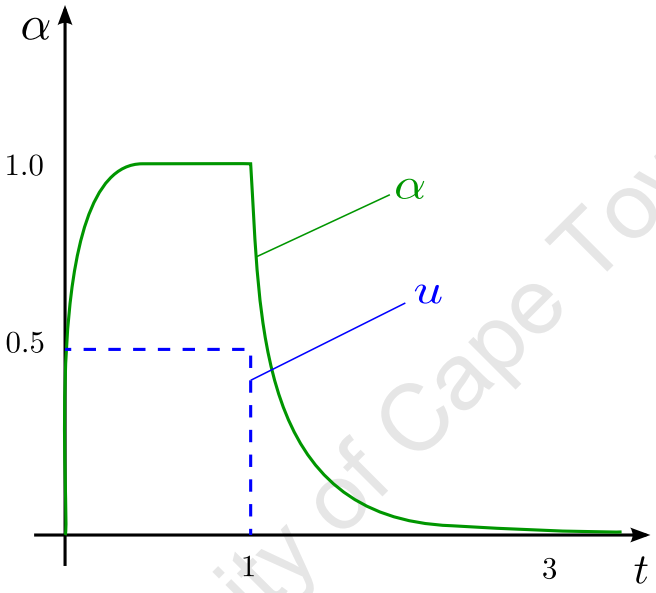

Figure 5.15: Example of an activation function $\alpha(t)$ for a given neural excitation $u(t)$ vs. time (s)

In summary, the Cauchy stress for this model is given by

$$\boldsymbol{\sigma} = -p\boldsymbol{I} + 2\,\mathrm{dev}[\boldsymbol{F}\frac{\partial U}{\partial C}\boldsymbol{F}^T] \ . \tag{5.106}$$

Furthermore, the incompressibility constraint must hold, i.e.,

$$J = \det \boldsymbol{F} = 1 \ . \tag{5.107}$$

In (5.106), the strain energy function U, is given by

$$U(\boldsymbol{C},\ \lambda_c) = U_{matrix}(\boldsymbol{I}_1^c) + U_p(\lambda_f) + U_s(\frac{\lambda_f}{\lambda_c},\ \lambda_c) \ , \tag{5.108}$$

where each term corresponds to the stress contributions in (5.91), (5.93), (5.97), and (5.99), by partial differentiation of the SEF with respect to $\boldsymbol{C}$.

5.2.3 Linearized muscle model

For the purposes of this thesis, a linearized formulation of the muscle model is used. This will be referred to as the LMM (linearized muscle model). The LMM discussed in this chapter is a linearized, small strain version of Martins' model [88, 89]. The LMM is used in FE simulations of the human tongue. The modified constitutive relations are introduced, and discussed in detail in this section.

The total stress in this linearized model remains unchanged, and is given by equation (5.88). In this case, $\boldsymbol{\sigma}_m$ is the stress in the surrounding ground substance, and is given by

$$\boldsymbol{\sigma}_m = \mathbb{C}_m \boldsymbol{\varepsilon} \ , \tag{5.109}$$

where $\mathbb{C}_m$ is the constitutive tensor of the ground material, which is typically isotropic, as in (5.77), and $\boldsymbol{\varepsilon}$ is the strain in the material.

Generally, for any stretch λ, one can write

$$\lambda = 1 + \varepsilon \ , \tag{5.110}$$

where $\varepsilon << 1$.

For small strains, the stress in the fibres, $\boldsymbol{\sigma}_f$ is given by

$$\boldsymbol{\sigma}_f = \lambda_f T \boldsymbol{N}_v \simeq T \boldsymbol{N}_v \ . \tag{5.111}$$

where

$$\boldsymbol{N}_v = [N_1 N_1 \ \ N_2 N_2 \ \ N_3 N_3 \ \ N_2 N_3 \ \ N_3 N_1 \ \ N_1 N_2]^T \ , \tag{5.112}$$

is Voigt notation for $\boldsymbol{N} \otimes \boldsymbol{N}$, or $N_i \, N_j$.

The strain in the fibre direction, ε_f, is given by

$$\varepsilon_f = \boldsymbol{N} \cdot \boldsymbol{\varepsilon} \boldsymbol{N} \ . \tag{5.113}$$

Using (5.110), the multiplicative split equation (5.95) can now be rewritten as

$$\lambda_f = 1 + \varepsilon_s + \varepsilon_c + \text{higher order terms}, \tag{5.114}$$

where the higher order terms can be assumed to be insignificant, and drop out of the equation.

Rearranging the terms in (5.114), and considering (5.110), we obtain a formulation for SE and CE strain in terms of fibre strain:

$$\lambda_f - 1 \simeq \varepsilon_s + \varepsilon_c \ , \tag{5.115}$$

hence

$$\varepsilon_f \simeq \varepsilon_s + \varepsilon_c \ . \tag{5.116}$$

The stress in the PE is given by

$$T_p(\lambda_f) = T_0 f_p(\lambda_f) \ . \tag{5.117}$$

Linearization of f_p in (5.98) gives

$$f_p(\varepsilon_f) = \begin{cases} 2aA\,\varepsilon_f & \varepsilon_f > 0 \\ 0, & \text{otherwise} \ . \end{cases} \tag{5.118}$$

The resulting linearized stress-strain relation for the PE can be seen in Figure 5.16(a). Here $m_p = 2aA$ is the tangent in the curve at $\boldsymbol{\varepsilon}_f = 0$.

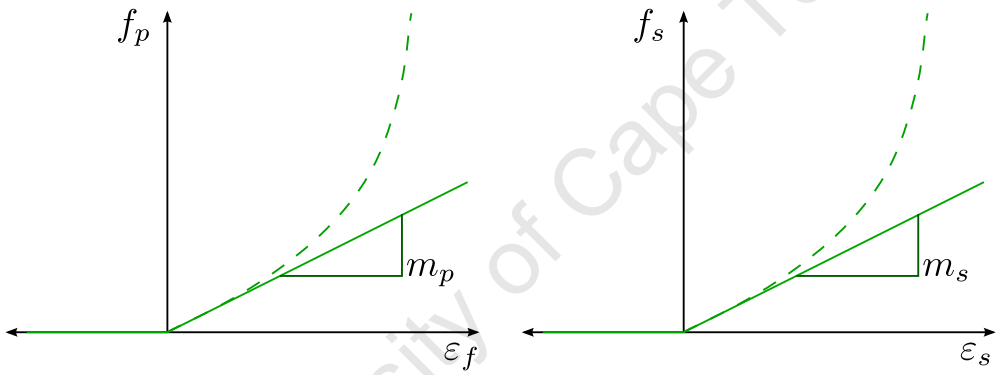

(a) Linearized stress-strain relation for the PE. (b) Linearized stress-strain relation for the SE.

Figure 5.16: Linearized stress-strain relation for the PE and the SE.

The stress in the SE is given by

$$T_s(\lambda_s, \lambda_c) = T_0 f_s(\lambda_s, \lambda_c) \ . \tag{5.119}$$

Using (5.116), we obtain

$$f_s(\varepsilon_f, \varepsilon_c) = 0.1[\exp\left[100(1+\varepsilon_c)(\varepsilon_f - \varepsilon_c)\right] - 1], \quad \varepsilon_s \geq 0 \ . \tag{5.120}$$

But

$$(1+\varepsilon_c)(\varepsilon_f - \varepsilon_c) = (\varepsilon_f - \varepsilon_c) + (\varepsilon_c\,\varepsilon_f - {\varepsilon_c}^2) \ . \tag{5.121}$$

Neglecting the higher order term and simplifying, we find that

$$f_s(\varepsilon_f, \varepsilon_c) = 0.1\left\{\exp\left[100(\varepsilon_f - \varepsilon_c)\right] - 1\right\}, \quad \varepsilon_s \geq 0 \ . \tag{5.122}$$

For small x we have $e^x \simeq 1+x$. Applying this approximation to (5.122), and using equation (5.116), the function then reduces to

$$f_s(\varepsilon_s) = \begin{cases} 10\,\varepsilon_s & \varepsilon_s \geq 0 \\ 0, & \text{otherwise} \ . \end{cases} \tag{5.123}$$

The resulting linearized stress-strain relation for the SE can be seen in Figure 5.16(b). Here $m_s = 10$ is the gradient of the straight line.

The stress in the CE is given by

$$T_c(\lambda_c, \dot{\lambda}_c, \alpha) = T_0\, f_c^l(\lambda_c)\, f_c^v(\dot{\lambda}_c)\, \alpha(t) \ , \tag{5.124}$$

where $f_c^l(\lambda_c)$ and $f_c^v(\dot{\lambda}_c)$ are modified from the standard formulations in (5.102) and (5.103), respectively, using the relationships in (5.110) and (5.116) giving $f_c^l(\varepsilon_c)$ and $f_c^v(\dot{\varepsilon}_c)$. $\alpha(t)$ is the activation function in (5.104). The function $f_c^l(\lambda_c)$ is replaced by the step function

$$f_c^l(\varepsilon_c) = \begin{cases} 1, & -0.5 \leq \varepsilon_c \leq 0.5 \\ 0, & \text{otherwise} \ . \end{cases} \tag{5.125}$$

The function $f_c^v(\dot{\lambda}_c)$ is replaced by the continuous piecewise linear function

$$f_c^v(\dot{\varepsilon}_c) = \begin{cases} 0, & \dot{\varepsilon}_c < -5 \\ \frac{1}{5}\dot{\varepsilon}_c + 1, & -5 \leq \dot{\varepsilon}_c \leq 3 \\ 1.6, & \dot{\varepsilon}_c > 3 \end{cases} \tag{5.126}$$

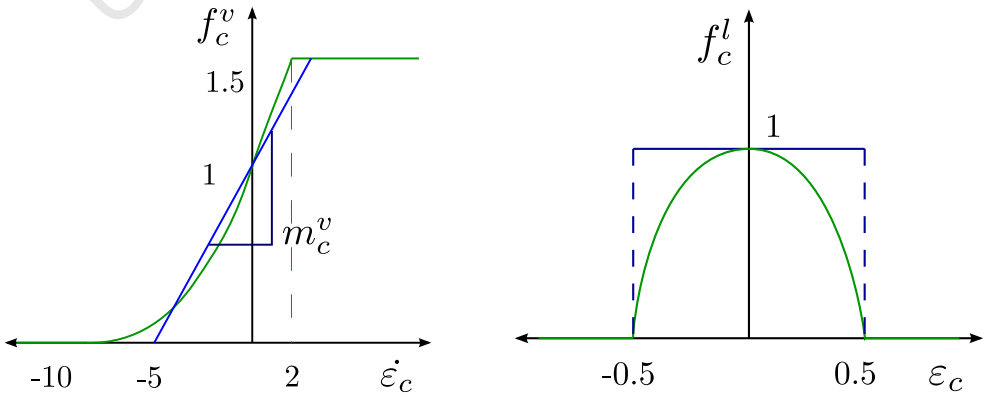

(a) Force-velocity relation of fully activated muscle tissue when CE is at optimal length.

(b) Force-length relation of muscle tissue due to an active force.

Figure 5.17: Linearized force-length and force-velocity relations for CE.

The resulting linearized stress vs. strain and stress vs. strain-rate relations for the CE can be seen in Figure 5.17(a) and 5.17(b) respectively. The blue line in each of the Figures 5.17(b) and 5.17(a) illustrate the linearized functions used for the LMM, superimposed on the original, non-linear functions, shown in green.

Activation function

An implicit method is a numerical method for solving time-variable ordinary and partial differential equations. An implicit method calculates the state of a system at a later time by solving an equation involving both the current state of the system and the later one.

The backward Euler method is an implicit method which uses the current and previous states of the system to find the solution at the current state. The time-dependent activation function given by the first-order differential equation system in (5.104) and (5.105) is to be linearized using this method [106, 143].

The activation rate in Equation (5.104), is given by

$$\dot{\alpha} = \frac{\alpha^n - \alpha^{n-1}}{\Delta t} \ , \tag{5.127}$$

where Δt is the timestep size, α^n is the activation at the current timestep, α^{n-1} is the activation at the previous timestep.

Applying the backward Euler method (5.127) to the activation function (5.104),

$$\frac{\alpha^n - \alpha^{n-1}}{\Delta t} = \frac{1}{\tau_{rise}}(1 - \alpha^n)u + \frac{1}{\tau_{fall}}(\alpha_{min} - \alpha^n)(1 - u) \ . \tag{5.128}$$

Multiplying each term by Δt gives

$$\alpha^n - \alpha^{n-1} = \frac{\Delta t\, u}{\tau_{rise}} - \frac{\alpha^n \Delta t\, u}{\tau_{rise}} + \frac{\Delta t}{\tau_{fall}}(\alpha_{min} - \alpha_{min} u - \alpha^n + \alpha^n\, u) \ . \tag{5.129}$$

Solving for α^n, gives the relation

$$\alpha^n(u) = \frac{\alpha^{n-1}\tau_{rise}\tau_{fall} + \Delta t\, u\, \tau_{fall} + \Delta t\, \alpha_{min}\tau_{rise} - \Delta t\, \alpha_{min} u\, \tau_{rise}}{\tau_{rise}\tau_{fall} + \Delta t\, u\, \tau_{fall} + \Delta t \tau_{rise} - \Delta t\, u\, \tau_{rise}} \ . \tag{5.130}$$

Using the neural input function in Equation (5.105), gives the solution for the activation function as

$$\alpha^n(t) = \begin{cases} 0, & t < 0 \\ \dfrac{\alpha^{n-1}\,\tau_{rise}\,\tau_{fall} + \Delta t\,\tau_{fall}}{\tau_{rise}\,\tau_{fall} + \Delta t\,\tau_{fall}}, & 0 \leq t \leq 1 \\ \dfrac{\alpha^{n-1}\,\tau_{rise}\,\tau_{fall} + \Delta t\,\alpha_{min}\,\tau_{rise}}{\tau_{rise}\,\tau_{fall} + \Delta t\,\tau_{rise}}, & t > 1\ . \end{cases} \tag{5.131}$$

This implicit method allows one to determine the activation level at the current increment in time based on the activation level at the previous time increment. It is in this way that the activation function is handled computationally.

LMM parameters

The parameters of the constitutive equation were obtained from multiaxial testing data, from Humphrey and Yin [65], and are given as

$$c = 3.87\ gf/cm^2\ ,$$
$$b = 23.46\ ,$$
$$A = 8.568 \times 10^{-4}\ gf/cm^2\ ,$$
$$a = 12.43\ .$$

In addition, the activation stress constant is chosen from Martins [88], namely

$$T_0 = 6280\ gf/cm^2\ , \tag{5.132}$$

From Equation (5.91), the scalar product of b and c, is equivalent to G, the shear modulus. It can be shown that the shear modulus is related to the Young's modulus as follows,

$$G = \frac{E}{2(1+\nu)}\ . \tag{5.133}$$

Using the parameters b and c, a relationship between Young's modulus, and the Poisson's ratio, is given as

$$E = 2(1+\nu)bc\ . \tag{5.134}$$

Thus the Young's modulus and Poisson's ratio of the surrounding ground tissue are selected according to this relationship. For a selected Poisson's ratio $\nu = 0.45$, Young's modulus is given as $E \approx 26000\ Pa$.

LMM summary

The behaviour of the LMM is summarized in Table 5.1 below:

Table 5.1: Summary of LMM behaviour.

$$\text{div}\boldsymbol{\sigma} + \boldsymbol{F} = \boldsymbol{0}$$

$$\boldsymbol{\sigma} = \boldsymbol{\sigma}_m + \boldsymbol{\sigma}_f$$

$$\boldsymbol{\sigma}_m = \mathbb{C}_m \boldsymbol{\varepsilon}$$

$$\boldsymbol{\varepsilon} = \frac{1}{2}\left(\nabla \boldsymbol{u} + (\nabla \boldsymbol{u})^T\right)$$

$$\boldsymbol{\sigma}_f = T_0[\beta \boldsymbol{\varepsilon}_f + \gamma \boldsymbol{\varepsilon}_c]\boldsymbol{N}_v$$

$$\varepsilon_f = \boldsymbol{N} \cdot \boldsymbol{\varepsilon} \boldsymbol{N}$$

$$T_p = \begin{cases} T_0\, 2aA\, \varepsilon_f & \varepsilon_f > 0 \\ 0, & \text{otherwise} \end{cases}$$

$$T_s = \begin{cases} T_0\, 10\, \varepsilon_s & \varepsilon_s \geq 0 \\ 0, & \text{otherwise} \end{cases}$$

$$T_c = T_0\, f_c^l(\varepsilon_c)\, f_c^v(\dot{\varepsilon_c})\, \alpha(t)$$

where

$$f_c^l(\varepsilon_c) = \begin{cases} 1, & -0.5 \leq \varepsilon_c \leq 0.5 \\ 0, & \text{otherwise .} \end{cases}$$

$$f_c^v(\dot{\varepsilon_c}) = \begin{cases} 0, & \dot{\varepsilon_c} < -5 \\ \frac{1}{5}\dot{\varepsilon_c} + 1, & -5 \leq \dot{\varepsilon_c} \leq 3 \\ 1.6, & \dot{\varepsilon_c} > 3 \end{cases}$$

$$\alpha(t) = \begin{cases} 0, & t < 0 \\ \dfrac{\alpha^{n-1}\, \tau_{rise}\, \tau_{fall} + \Delta t\, \tau_{fall}}{\tau_{rise}\, \tau_{fall} + \Delta t\, \tau_{fall}} & 0 \leq t \leq 1 \\ \dfrac{\alpha^{n-1}\, \tau_{rise}\, \tau_{fall} + \Delta t\, \alpha_{min}\, \tau_{rise}}{\tau_{rise}\, \tau_{fall} + \Delta t\, \tau_{rise}} & t > 1 \end{cases}$$

6 Finite Element Approximations

"Divide each difficulty into as many parts as is feasible and necessary to resolve it." This statement posed by Rene Descartes adequately defines the process of the finite element method (FEM).

This chapter presents a general overview of the finite element method (FEM). The governing equations presented in the previous chapter are incorporated into the finite element formulation for the linearized muscle model (LMM). The commercial finite element software package Abaqus [24] is used as a basis for FE modelling, and this LMM is implemented in an Abaqus user element (UEL). For further reference, more detailed accounts on the FEM can be found in the literature, e.g. [7, 36, 61, 147].

6.1 The finite element method

It has been about 50 years since the words "finite element" were introduced in a publication by R.W. Clough [21], who was, at that time, working in the civil engineering field [22]. The essentials of FEM however, such as mesh discretization, can be traced back to around 1941, with the works of A. Hrennikoff and R. Courant, in the civil and aeronautical engineering fields. Courant's work followed on from earlier significant research in partial differential equations (PDEs) by J. W. S. Rayleigh, W. Ritz, and B. Galerkin.

The FEM is an approximate method for finding solutions of differential equations. It involves discretization of the domain into a set of discrete sub-domains, called elements, interconnected at points, called nodes.

6.1.1 Strong to weak formulation and discretization

Consider the boundary value problem (BVP) in Figure 5.3, and the boundary condition stated in (5.53) and (5.54). The boundary conditions, together with the PDE, defined over the required domain (Ω), is called the "strong form" of the BVP. The BVP is generally not soluble in closed form. To obtain approximate solutions using FEM, the strong form is first converted into a weak form (or variational form). The weak problem is then posed on a discrete space. For a linear BVP, this leads to a system of simultaneous linear or non-linear algebraic equations.

Weak formulations are an important tool for solving partial differential equations. In a weak formulation, an equation is no longer required to hold at each point in the domain. We show how a weak

formulation is derived taking as an example the problem

$$-\nabla^2 u = f \text{ , on a domain } \Omega \subset \mathbb{R}^d \text{ ,} \tag{6.1}$$

$$u = 0 \text{ on the boundary } \Gamma \text{ .} \tag{6.2}$$

Testing (6.1) with differentiable test functions v, which also satisfies $v = 0$ on Γ, we get

$$-\int_\Omega v\nabla^2 u \, dx = \int_\Omega fv \, dx. \tag{6.3}$$

The left side of this equation can be made to be closer to symmetric by using integration by parts,

$$\int_\Omega \nabla u \cdot \nabla v \, dx = \int_\Omega fv \, dx \quad v = 0 \text{ on } \Gamma. \tag{6.4}$$

This is the weak formulation of Poisson's equation: to find $u \in V$ which satisfies (6.4) for all $v \in V$, where V is a space in which the problem is posed. The generic form is obtained by assigning

$$a(u, v) = \int_\Omega \nabla u \cdot \nabla v \, dx \tag{6.5}$$

and

$$f(v) = \int_\Omega fv \, dx. \tag{6.6}$$

where $a(\cdot, \cdot)$ is a continuous bilinear form, and f is a continuous linear operator on V. This is the fundamental basis of the Galerkin method for numerical solutions of PDEs.

Galerkin's method

The Galerkin method is a method for converting the weak form of a differential equation to a discrete problem. The abstract problem posed as a weak formulation on a Hilbert space, V, in equations (6.4), (6.5), and (6.6), is restated as

$$u \in \mathrm{V} \text{ such that for all } v \in \mathrm{V}, a(u, v) = f(v). \tag{6.7}$$

The essence of the Galerkin method is to replace V with a subspace V^h which is finite-dimensional, and to replace (6.7) with the problem

$$u^h \in V^h \text{ such that for all } v^h \in V^h, \tag{6.8}$$

$$a(u^h, v^h) = f(v^h) \text{ .} \tag{6.9}$$

Since V_h is finite-dimensional, it has a basis $\{N_i\}_{i=1}^n$, and we can write

$$u^h = \sum_{i=1}^{n} N_i d_i \quad , \quad v^h = \sum_{i=1}^{n} N_i \bar{d}_i \ . \tag{6.10}$$

Substituting (6.10), into (6.7) we obtain the linear system

$$\mathbf{K}\boldsymbol{d} = \mathbf{F} \ , \tag{6.11}$$

where $\mathbf{K}$, $\boldsymbol{d}$, and $\mathbf{F}$ are the global stiffness matrix, the global displacement vector, and the global force vector, respectively, and where

$$K_{ij} = a(N_i, N_j) \text{ and } F_i = f(N_i) \ . \tag{6.12}$$

6.2 Linearized muscle model

The governing PDEs discussed in the previous chapter, and summarized in Table 5.1 are used to develop a linearized weak formulation for muscle material. The FEM applied to the formulation, using the same approach to derive the weak form of the equilibrium equation, is addressed in the following section.

For equilibrium of the LMM BVP,

$$\int_\Omega \boldsymbol{\sigma}(\boldsymbol{u}, \varepsilon_c) : \boldsymbol{\varepsilon}(\boldsymbol{v}) d\Omega = \int_\Omega \boldsymbol{f} \cdot \boldsymbol{v} \ d\Omega \ . \tag{6.13}$$

Using the formulation of total stress from (5.88), and ignoring the incompressible component gives

$$\boldsymbol{\sigma} = \boldsymbol{\sigma}_m + \boldsymbol{\sigma}_f \ . \tag{6.14}$$

Expanding this equation using equations (5.109) and (5.111) gives

$$\boldsymbol{\sigma} = \mathbb{C}_m \boldsymbol{\varepsilon} + T_0[\beta \varepsilon_f + \gamma \varepsilon_c^n] \boldsymbol{N}_v \ , \tag{6.15}$$

where the parameters are defined by

$$\beta = m_p + m_s \ , \tag{6.16}$$

$$\gamma = -m_s \ , \tag{6.17}$$

and n is the current timestep in the solution process.

The constraint that states that in the Hill three-element model, the contractile stress must be equal to the series stress in (5.87) in a one-dimensional sense, can also be written in three-dimensional form as

$$\boldsymbol{\sigma_c} = \boldsymbol{\sigma_s} \ . \tag{6.18}$$

By expanding the contractile and series element stress functions using (5.126) and (5.123), gives

$$f_c^l(m_c^v\dot{\varepsilon}_c + c_c^v)\alpha^n = m_s(\varepsilon_f - \varepsilon_c^n) \ , \tag{6.19}$$

where the parameters derive from (5.126) and (5.123).

Using the backward-Euler method, the contractile strain rate $\dot{\varepsilon}_c$, can be approximated by

$$\dot{\varepsilon}_c = \frac{\varepsilon_c^n - \varepsilon_c^{n-1}}{\Delta t} \ , \tag{6.20}$$

where n is the increment in time, ε_c^n is the current contractile strain, and ε_c^{n-1} is the contractile strain at the previous timestep.

Combining equations (6.19) and (6.20), ε_c^n is then given by the relationship

$$\varepsilon_c^n = \eta\phi\varepsilon_f + \phi(\varepsilon_c^{n-1} + \kappa\Delta t) \ , \tag{6.21}$$

where new parameters are chosen by rearrangement of terms, assuming $f_c^l \neq 0,\ \alpha^n \neq 0,\ m_c^v \neq 0$, as

$$\eta = \frac{m_s\ \Delta t}{m_c^v\ f_c^l\ \alpha^n} \ , \tag{6.22}$$

$$\phi = (1+\eta)^{-1} \ , \tag{6.23}$$

$$\kappa = -\frac{c_c^v}{m_c^v} \ . \tag{6.24}$$

Substitution of $\boldsymbol{\varepsilon}_c^n$ using equation (6.21) into equation (6.15) gives

$$\boldsymbol{\sigma} = \mathbb{C}_m\boldsymbol{\varepsilon} + T_0[(\beta + \gamma\eta\phi)\varepsilon_f]\boldsymbol{N}_v + T_0[\gamma\phi(\varepsilon_c^{n-1} + \kappa\Delta t)]\boldsymbol{N}_v \ . \tag{6.25}$$

Equation (6.25) together with the weak equilibrium equation in (6.13) has to be solved. In order to achieve this solution, some relevant FE theory is introduced and implemented here.

6.2.1 Trilinear hexahedral element

The finite element method is a method for constructing the basis or shape functions in a way that lends itself to solution on the computer. We will use shape functions constructed on a cube or

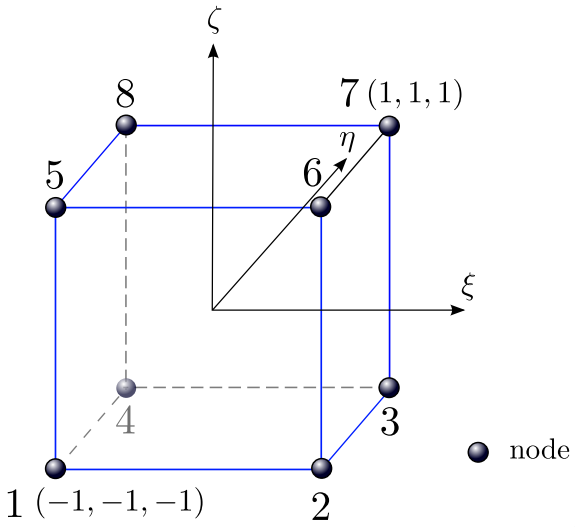

Figure 6.1: The 8-noded, trilinear, isoparametric hexahedral element.

hexahedron. An eight-noded hexahedral (brick) element is developed based on the partition of unity method. The formulation uses linear isoparametric shape functions. The nodes are numbered so as to ensure that the Jacobian determinant, and thus, the volume is positive.
The reference element's coordinate system is denoted by ξ, η, and ζ. The element represented in this coordinate system is illustrated in Figure 6.1.

- ξ ranges from -1 on face 1485 to $+1$ on face 2376,
- η ranges from -1 on face 1265 to $+1$ on face 3487,
- ζ ranges from -1 on face 1234 to $+1$ on face 5678.

The reference element shape functions are defined by

$$\hat{\mathrm{N}}_i(\xi,\eta,\zeta) = \frac{1}{8}(1+\xi\xi_i)(1+\eta\eta_i)(1+\zeta\zeta_i)\ , \tag{6.26}$$

where ξ_i, η_i and ζ_i denote the coordinates of the i^{th} node.

Using isoparametric mapping, i.e.

$$\boldsymbol{x}(x,y,z) = \sum_A \boldsymbol{x}_A\,\mathrm{N}_A(\xi,\eta,\zeta)\,, \tag{6.27}$$

the shape functions on the elements are given by

$$\mathrm{N}_i^e(x,y,z) = \hat{\mathrm{N}}_i(\xi,\eta,\zeta)\ , \tag{6.28}$$

where $\mathrm{N}_i^e(x,y,z) = 1$ at node i, and 0 at other nodes, i.e.

$$\mathrm{N}_i^e(x_j) = \delta_{ij}\ , \tag{6.29}$$

where x_j is the vector storing the coordinates.

This isoparametric mapping from the actual coordinate system to the isoparametric coordinate system and back to the actual coordinate system, over a single timestep, is illustrated in Figure 6.2. This mapping occurs for each element at each timestep.

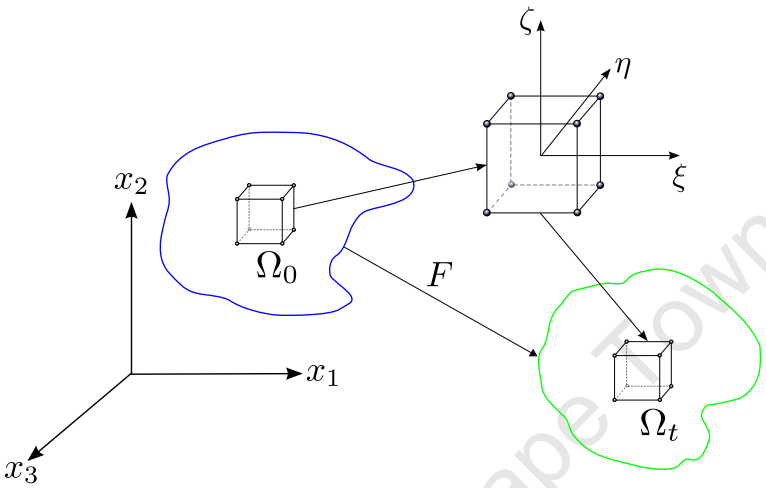

Figure 6.2: An illustration of isoparametric mapping.

The displacement of the element may be found by using the interpolation functions, i.e.

$$\boldsymbol{u} = \mathbf{N}\boldsymbol{d} \ , \tag{6.30}$$

where $\boldsymbol{u}$ is the vector of displacements, and $\boldsymbol{d}$ is the vector of nodal displacements, $\mathbf{N}$ is the matrix of shape or interpolation functions, defined as

$$\mathbf{N} = [N_1 \ ... \ N_8]^T \ . \tag{6.31}$$

Equation (6.30) is used to derive the strain, $\boldsymbol{\varepsilon}$, in the element as

$$\boldsymbol{\varepsilon} = \mathbf{D}\boldsymbol{u} = \mathbf{D}\mathbf{N}\boldsymbol{d} \ , \tag{6.32}$$

where $\mathbf{D}$ is a matrix of differential operators that convert displacements to strains using linear elasticity theory. Its basic structure in Voigt notation is given by

$$\mathbf{D} = \left[\begin{array}{ccc|c|ccc} \frac{\partial}{\partial x} & 0 & 0 & & \frac{\partial}{\partial x} & 0 & 0 \\ 0 & \frac{\partial}{\partial y} & 0 & & 0 & \frac{\partial}{\partial y} & \\ 0 & 0 & \frac{\partial}{\partial z} & & 0 & 0 & \frac{\partial}{\partial z} \\ \frac{\partial}{\partial y} & \frac{\partial}{\partial x} & 0 & \ldots & \frac{\partial}{\partial y} & \frac{\partial}{\partial x} & 0 \\ 0 & \frac{\partial}{\partial z} & \frac{\partial}{\partial y} & & 0 & \frac{\partial}{\partial z} & \frac{\partial}{\partial y} \\ \frac{\partial}{\partial z} & 0 & \frac{\partial}{\partial x} & & \frac{\partial}{\partial z} & 0 & \frac{\partial}{\partial x} \end{array}\right] . \tag{6.33}$$

where $I = 8$, is the number of nodes, and the size of $\mathbf{D}$ is 6×24, since there are 3 degrees of freedom per node, and 8 nodes.

Equation (6.32) shows that the strain-displacement matrix $\mathbf{B}$, is given by

$$\mathbf{B} = \mathbf{D}\mathbf{N} , \tag{6.34}$$

or in matrix notation as

$$\mathbf{B} = \left[\begin{array}{ccc|c|ccc} \frac{\partial N_1}{\partial x} & 0 & 0 & & \frac{\partial N_I}{\partial x} & 0 & 0 \\ 0 & \frac{\partial N_1}{\partial y} & 0 & & 0 & \frac{\partial N_I}{\partial y} & 0 \\ 0 & 0 & \frac{\partial N_1}{\partial z} & & 0 & 0 & \frac{\partial N_I}{\partial z} \\ \frac{\partial N_1}{\partial y} & \frac{\partial N_1}{\partial x} & 0 & \ldots & \frac{\partial N_I}{\partial y} & \frac{\partial N_I}{\partial x} & 0 \\ 0 & \frac{\partial N_1}{\partial z} & \frac{\partial N_1}{\partial y} & & 0 & \frac{\partial N_I}{\partial z} & \frac{\partial N_I}{\partial y} \\ \frac{\partial N_1}{\partial z} & 0 & \frac{\partial N_1}{\partial x} & & \frac{\partial N_I}{\partial z} & 0 & \frac{\partial N_I}{\partial x} \end{array}\right] , \tag{6.35}$$

where the number of nodes I is 8.

The strains in an element can therefore also be given by

$$\boldsymbol{\varepsilon} = \mathbf{B}\boldsymbol{d} . \tag{6.36}$$

where

$$\boldsymbol{\varepsilon} = \left[\begin{array}{c} \varepsilon_{xx} \\ \varepsilon_{yy} \\ \varepsilon_{zz} \\ \gamma_{xy} \\ \gamma_{xz} \\ \gamma_{yz} \end{array}\right] = \left[\begin{array}{c} \frac{\partial u_x}{\partial x} \\ \frac{\partial u_y}{\partial y} \\ \frac{\partial u_z}{\partial z} \\ \frac{\partial u_x}{\partial y} + \frac{\partial u_y}{\partial x} \\ \frac{\partial u_x}{\partial z} + \frac{\partial u_z}{\partial x} \\ \frac{\partial u_y}{\partial z} + \frac{\partial u_z}{\partial y} \end{array}\right] . \tag{6.37}$$

The Jacobian matrix is defined as $\boldsymbol{J}$, and it is used to map from the reference element, $\hat{\Omega}$ to the actual element Ω_e, and vice versa, i.e.

$$\frac{\partial \mathbf{N}}{\partial \boldsymbol{X}} = \underbrace{\left[\frac{\partial \boldsymbol{X}(\boldsymbol{\xi})}{\partial \boldsymbol{\xi}}\right]}_{\boldsymbol{J}(\boldsymbol{\xi})}^{-T} \frac{\partial \mathbf{N}}{\partial \boldsymbol{\xi}} \tag{6.38}$$

The Jacobian matrix is given by

$$\boldsymbol{J} = \frac{\partial \boldsymbol{X}}{\partial \boldsymbol{\xi}} = \begin{bmatrix} \frac{\partial X}{\partial \xi} & \frac{\partial Y}{\partial \xi} & \frac{\partial Z}{\partial \xi} \\ \frac{\partial X}{\partial \eta} & \frac{\partial Y}{\partial \eta} & \frac{\partial Z}{\partial \eta} \\ \frac{\partial X}{\partial \zeta} & \frac{\partial Y}{\partial \zeta} & \frac{\partial Z}{\partial \zeta} \end{bmatrix} . \tag{6.39}$$

The inverse, transverse Jacobian matrix is given by

$$\boldsymbol{J}^{-T} = \frac{\partial \boldsymbol{\xi}}{\partial \boldsymbol{X}} = \begin{bmatrix} \frac{\partial \xi}{\partial X} & \frac{\partial \eta}{\partial X} & \frac{\partial \zeta}{\partial X} \\ \frac{\partial \xi}{\partial Y} & \frac{\partial \eta}{\partial Y} & \frac{\partial \zeta}{\partial Y} \\ \frac{\partial \xi}{\partial Z} & \frac{\partial \eta}{\partial Z} & \frac{\partial \zeta}{\partial Z} \end{bmatrix} . \tag{6.40}$$

The determinant of the Jacobian matrix is defined as

$$J = \det \boldsymbol{J} \tag{6.41}$$

6.2.2 Stiffness matrix assembly

The element stiffness matrix for linear elasticity is given by

$$\mathbf{K}_e = \int_{\Omega_e} \mathbf{B}_e^T \, \mathbb{C}_e \, \mathbf{B}_e \, d\Omega_e \ . \tag{6.42}$$

The global stiffness matrix is found using equations (6.11), and (6.42),

$$\mathbf{K} = \mathsf{A}_{e=1}^{n_{el}} \left(\mathbf{K}_e\right) = \mathsf{A}_{e=1}^{n_{el}} \left(\int_{\Omega_e} \mathbf{B}_e^T \, \mathbb{C}_e \, \mathbf{B}_e \, d\Omega_e \right) \ , \tag{6.43}$$

and the force vector is given by

$$\mathbf{F} = \mathbf{F}^{\text{ext}} - \mathbf{F}^{\text{int}} \ , \tag{6.44}$$

$$\mathbf{F} = \mathsf{A}_{e=1}^{n_{el}} \left(\int_{\Omega_e} \mathbf{N}_e^T \, F_e \, d\Omega_e \ - \int_{\Omega_e} \mathbf{B}_e^T \, \mathbb{C}_e \, \mathbf{B}_e \, d\Omega_e \bar{\boldsymbol{d}} \right) \ , \tag{6.45}$$

where $\mathbf{A}$ denotes the finite element assembly operator, and n_{el} is the number of elements.

Applying Equations (6.13) to (6.25) to

$$\mathbf{K}\boldsymbol{d} = \mathbf{F} \ , \tag{6.46}$$

gives the equalibrium equation for the LMM as

$$\begin{aligned} &\Big\{ \overbrace{\int_\Omega \mathbf{B}^T \mathbb{C}_m \mathbf{B} \, d\Omega}^{\mathbf{K}_m} + \overbrace{\int_\Omega T_0(\beta + \gamma\eta\phi)\mathbf{B}^T \mathbb{C}_f \mathbf{B} \, d\Omega}^{\mathbf{K}_f} \Big\} \boldsymbol{d} \\ &\quad = \underbrace{\int_\Omega \mathbf{N}^T \boldsymbol{b} \, d\Omega}_{\mathbf{F}_b} - \underbrace{\int_\Omega T_0 \gamma\phi(\varepsilon_c^{n-1} - \kappa\Delta t)\mathbf{B}^T \boldsymbol{N}_v \, d\Omega}_{\mathbf{F}_f} - \underbrace{\int_\Omega \mathbf{B}^T \boldsymbol{\sigma} \, d\Omega}_{\mathbf{F}_{\text{res}}} \ , \end{aligned} \tag{6.47}$$

where $\mathbb{C}_f$ is the Voigt notation (6×6, 2nd-rank) tensor for the 4th-rank tensor created by

$$\boldsymbol{N} \otimes \boldsymbol{N} \otimes \boldsymbol{N} \otimes \boldsymbol{N} \quad \text{or} \quad \mathrm{N}_i \, \mathrm{N}_j \, \mathrm{N}_k \, \mathrm{N}_l \ , \tag{6.48}$$

$\mathbf{K}_m$ is the equivalent standard stiffness matrix term,
$\mathbf{K}_f$ is the fibre stiffness matrix term,
$\mathbf{F}_b$ is the equivalent standard body force term,
$\mathbf{F}_{\text{res}}$ is the residual force term,
and $\mathbf{F}_f$ is the fibre force term.

The contractile strain at the current increment in time is found by obtained from the current fibre strain, and previous contractile strain using (6.21). The variables $\beta, \gamma, \eta, \phi, \kappa$, are all constant w.r.t. time. These variables, including ε_c^{n-1}, and α^{n-1} have to be initialized at the start of the first increment. ε_c^{n-1} is the contractile strain at the previous timestep, and is required at the current timestep n.

Gaussian quadrature

In numerical analysis, a quadrature rule is an approximation of the definite integral of a function, usually stated as the weighted sum of function values at specified points within the domain of integration. An n-point Gaussian quadrature rule is constructed to yield an exact result for polynomials of degree $2n - 1$ or less, by a suitable choice of the points x_i and weights w_i for $i = 1, ..., n$.

Integration is done on the reference element, so an element in the actual domain is mapped to a reference element coordinate system as illustrated in Figure 6.2. The integrals over the reference element are related to the original element by the Jacobian, namely J, of the mapping. The domain

of integration for such a rule is conventionally taken as $[-1, 1]$, so the rule is stated as

$$\int_{-1}^{1} f(x)\, dx \approx \sum_{i=1}^{n} w_i f(x_i). \tag{6.49}$$

Table 6.1: Gaussian quadrature rules

Number of points, n	Points, x_i	Weights, w_i
1	0	2
2	$\pm\sqrt{\frac{1}{3}}$	1

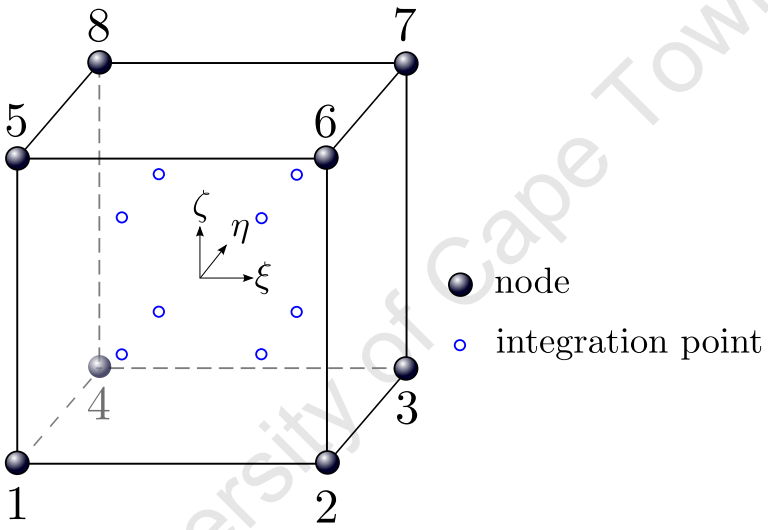

Figure 6.3: The eight-noded, trilinear, hexahedral isoparametric element with integration points

The Gaussian quadrature points for the trilinear hexahedral element are illustrated in Figure 6.3. For this element, the Gaussian quadrature is given as

$$\int_{-1}^{1}\int_{-1}^{1}\int_{-1}^{1} f(\xi, \eta, \zeta)\, d\xi\ d\eta\ d\zeta \approx \sum_{i=1}^{n} w_i f(\xi_i, \eta_i, \zeta_i). \tag{6.50}$$

Applying Gaussian quadrature to the linear elastic relationship in (6.42), results in the approximation for the stiffness matrix as

$$\mathbf{K}_e \approx \sum_{i=1}^{p_1}\sum_{j=1}^{p_2}\sum_{k=1}^{p_3} w_i\, w_j\, w_k\, \mathbf{B}_e^T\, \mathbb{C}_e\, \mathbf{B}_e\, J\, d\Omega_e\ , \tag{6.51}$$

where p_1, p_2 and p_3 are the number of Gauss points in the ξ, η and ζ directions, and $J = \det\boldsymbol{J}$. In the case of trilinear hexahedral elements, $p_1 = p_2 = p_3 = 2$.

6.3 LMM Algorithm

The algorithm for the implementation of the LMM in an Abaqus UEL is presented here. This subroutine, written in the FORTRAN programming language, is called once per timestep, for each element.

Data: **K F**

Result: $\boldsymbol{u}$

Muscle activation parameter, $\alpha^{n-1} \approx 0$;

Set number of fibres and fibre data filenames ;

Declare all variables and initialize arrays ;

Read material properties from input file ;

Check if passive or active fibres are to be used, or no fibres, read from input file ;

Set Humphrey's and linearized muscle model (LMM) parameters ;

if *fibres = active, set* T_0 **then**

  if *reduced activity* $= 100\%$ **then**

    $T_0 = 6820 * 98.065;$

  else if *reduced activity* $= 1\%$ **then**

    $T_0 = 6820 * 98.065 * 0.01;$

  else if *reduced activity* $= 0.1\%$ **then**

    $T_0 = 6820 * 98.065 * 0.001;$

  end

end

Algorithm 1: LMM initialization.

Check if small-displacement analysis, implicit time increment, and static;

Set body force from load in input file;

Recall neural activation α^{n-1} from previous timestep;

if *element number (JELEM) = fibre index* **then**

  Store fibre on element basis in fibre array;

  if *active = true* **then**

    Set neural activation history according to implicit activation relationship;

    if *current time < time at end of activitation* **then**

      $\alpha^n = f_1(\alpha^{n-1})$;

    else

      $\alpha^n = f_2(\alpha^{n-1});$

    else

      $\alpha^n \approx 0;$

    end

  else

    $\alpha^n \approx 0$

  end

end

Algorithm 2: LMM activation function selection.

Store current activation level, α^n, determine and store activation rate, $\dot{\alpha^n}$

Determine reorganized Martins' constants from LMM constants

Form isotropic ground material constitutive tensor, $\mathbb{C}_M$, in Voigt notation

Determine Gauss integration point coordinates from nodal c

for *k = 1 to number of integration points* **do**

  Construct $\boldsymbol{N} \otimes \boldsymbol{N} \otimes \boldsymbol{N} \otimes \boldsymbol{N}$ from fibre array and convert to Voigt notation $\mathbb{C}_f$;

  Construct $\boldsymbol{N} \otimes \boldsymbol{N}$ from fibre array and convert to Voigt notation $\boldsymbol{N}_v$;

  Store $\mathbb{C}_f$ and $\boldsymbol{N}_v$ in an array;

  Construct shape functions, shape function derivatives, and strain displacement matrix $\mathbf{B}$;

  Construct isotropic stiffness $\mathbf{K}_m = \mathbf{B}^T \mathbb{C}_m \mathbf{B} W J$;

  Construct fibre stiffness $\mathbf{K}_f = \mathbf{B}^T \mathbb{C}_f \mathbf{B} W J$;

  for *i = 1 to NDOFEL (number of degrees of freedom per element)* **do**

    for *j = 1 to NDOFEL* **do**

      Construct stiffness matrix $[\text{AMATRX}]_{ij} = [K_m]_{ij} + T_0(\beta + \gamma\,\eta\,\phi)[K_f]_{ij}$;

    end

  end

end

Algorithm 3: LMM stiffness matrix (AMATRX) formation.

Determine current stresses and strains;
for *k = 1 to number of integration points* **do**
  Call shape functions, shape function derivatives, and strain displacement matrix $\mathbf{B}$;
  Recall $\mathbb{C}_f$ and $\boldsymbol{N}_v$ from a storage array;
  if *KINC* $= 1$ **then**
    CE strain $\boldsymbol{\varepsilon}_c^{n-1} = 0$
  else
    Recall CE strain $\boldsymbol{\varepsilon}_c^{n-1}$ from previous increment using SVARS
  end
  Determine total strain $\boldsymbol{\varepsilon}_T = \mathbf{B}\,\boldsymbol{u}^n$;
  Determine fibre strain $\boldsymbol{\varepsilon}_f = \mathbf{N}_v\,\boldsymbol{\varepsilon}_T$;
  Determine current CE strain from previous CE strain $\boldsymbol{\varepsilon}_c^n = \eta\phi\boldsymbol{\varepsilon}_f + \phi(\boldsymbol{\varepsilon}_c^{n-1} + \kappa\Delta t)$;
  Store current CE strain in SVARS ;
  Determine CE strain rate $\dot{\boldsymbol{\varepsilon}}_c$;
  Determine SE strain, $\boldsymbol{\varepsilon}_s = \boldsymbol{\varepsilon}_f - \boldsymbol{\varepsilon}_c^n$;
  Determine $T_s(\boldsymbol{\varepsilon}_s)$, $T_p(\boldsymbol{\varepsilon}_f)$, $T_c(\dot{\boldsymbol{\varepsilon}}_c)$, and $T_T = T_p + T_s$;
  SE stress $\boldsymbol{\sigma}_s = \boldsymbol{N}_v T_s$;
  CE stress $\boldsymbol{\sigma}_c = \boldsymbol{N}_v T_c$;
  Fibre stress $\boldsymbol{\sigma}_f = \boldsymbol{N}_v T_T$;
  Isotropic ground matrix stress $\boldsymbol{\sigma}_m = \mathbb{C}_m\boldsymbol{\varepsilon}_T$;
  Total stress $\boldsymbol{\sigma}_T = \boldsymbol{\sigma}_m + \boldsymbol{\sigma}_f$;
  Store residual stress $\boldsymbol{\sigma}_{\text{res}}^n = \boldsymbol{\sigma}_T$ in SVARS ;
  Construct residual force $\mathbf{F}_{\text{res}} = \mathbf{B}^T\,{\boldsymbol{\sigma}_{\text{res}}}^n\,W\,J$;
  Construct fibre force term $\mathbf{F}_f = T_0\gamma\phi\,(\boldsymbol{\varepsilon}_c^{n-1} + \kappa\Delta t)\mathbf{B}^T\boldsymbol{N}_v\,W\,J$;
  Construct body force term $\mathbf{F}_b = \mathbf{N}^T\boldsymbol{b}\,W\,J$;
  for *i = 1 to NDOFEL* **do**
    Construct $\{\text{RHS}\}_i = \{\mathbf{F}_b\}_i - \{\mathbf{F}_f\}_i - \{\mathbf{F}_{\text{res}}\}_i$;
  end
  Determine and store current displacement $\boldsymbol{u}^n$ in SVARS ;
end

Algorithm 4: LMM RHS vector formation.

6.4 Implementation in Abaqus

Abaqus is a general purpose FEA program, used for modelling the mechanics of structures under externally applied loads [24]. The software itself consists of three packages, namely Abaqus/Standard, for implicit FEM problems, Abaqus/Explicit, for explicit FEM problems, and Abaqus/CAE, for preprocessing and visualization of results.

Abaqus Standard uses an iterative equation solver for both linear and nonlinear behaviours. Linear analysis is always considered as linear perturbation analysis. This approach allows general application of linear analysis techniques for more complicated problems [26].

Preprocessing in Abaqus/CAE involves geometrical modelling, done graphically, in Abaqus itself, or another preprocessing program, and assigning various other parameters of the physical problem to be solved. An Abaqus input file with most of the model problems included is generated at the end of this process. The input file can be modified with a text editor.

Simulations which solve the problem, are run in Abaqus/Standard. The history of various variables from the beginning of the simulation, such as stress, displacement, strain etc. are stored. Once a simulation has completed, postprocessing of results can be done numerically, and also visually, using the visualization module of Abaqus/CAE.

The Abaqus UEL user subroutine is used to accomodate the nonstandard features of the LMM. The UEL subroutine is called for each element of user-defined element type at the beginning and end of each solution increment. The subroutine takes as input, the nodal displacement vector, nodal coordinates, and material properties and returns the stiffness matrix and force vector. The visualization of results in Abaqus CAE, obtained from using a UEL subroutine are limited.

6.4.1 Material fibre management

The user subroutine "orient", allows the user to define a local coordinate system in a required direction, where one of the main coordinate axes are in the direction of the fibres ($\boldsymbol{N}$). The user subroutine "distribution", allows the user to define spatially varying coordinate systems, which differ from one integration point, or element, to the next.

Another way to handle material fibres, is to store the fibre data in a formatted plain text data file, and read in this fibre data through the execution of the UEL subroutine source file. This process of data management was selected for the muscle fibre directions. A generated model mesh is aligned with fibre data extracted in Mimics (see Chapter 4). The mesh and fibre data are combined when the subroutine is run, and the fibre data file opened.

6.4.2 Convergence of solution

In Abaqus, the system of linear equations to be solved is denoted by the matrix equation

$$\mathbf{K}\boldsymbol{u} = \mathbf{F} \ , \tag{6.52}$$

where $\mathbf{K}$ is the global stiffness matrix, $\mathbf{F}$ is the load vector, and $\boldsymbol{u}$ is the desired solution.

To generate the solution, a sequence of linear solver iterations is performed, whereby an approximate solution gets closer to the exact solution at each iteration. The term "convergence" is used to describe this process. This is done irrespective of whether the problem is linear or non-linear. The error in the approximate solution is measured by the residual, $\boldsymbol{R}$, of the linear system, defined by

$$\boldsymbol{R} = ||\mathbf{K}\boldsymbol{u} - \mathbf{F}|| \ , \tag{6.53}$$

where $||\cdot||$ is the l^2 norm, defined by

$$|\boldsymbol{x}| = \sqrt{\sum_{i=1}^{n} |x_i|^2} \ . \tag{6.54}$$

The approximate solution is said to be converged when the residual, $\boldsymbol{R}$ is below a default tolerance.

7 Verification and Validation

The aim of this chapter is to describe the methods employed to verify and validate the behaviour of the linearized muscle model (LMM). In order to do this, various computational benchmark tests are to be carried out on the model. These benchmark tests are designed to examine specific aspects of the behaviour of the model and include, amongst others, uniaxial testing and Cook's membrane problem. Comparative results for some of these tests are available in the literature [104].

Mechanical behaviour under the influence of fibre orientation, and muscle activation is also tested. The effects of fibre orientations are examined using uniaxial passive tests, while the effects of muscle activation are examined with isometric and isotonic contraction tests (see Subsection 3.4.5). The results for the active tests are compared to the test data available in Martins et. al. [89, 88]. A basic test with isotropic behaviour is performed on the LMM and compared to the Abaqus standard 8-noded hexahedral element, i.e. the C3D8 element type [24]. Passive and active muscle behaviours are also compared and discussed.

In an isotropic test, all muscle fibre effects are completely removed by setting the stress $T_0 = 0$ in (5.132). Thus only the isotropic ground matrix has an effect. Uniaxial isotropic tests are covered in Subsection 7.1.1, and isotropic tests on the tongue are covered in Section 8.2.

When running passive tests the full model is used with the activation parameter α set approximately equal to zero. Since α appears in the denominator in (6.22), it is not set to zero exactly, but rather set to a significantly small value compared to the magnitude of all other parameters. T_0 is not set to zero for the passive and active tests. Passive testing of the LMM should thus exhibit transverse isotropic behaviour. The descriptions and results for the benchmark tests are presented and discussed in detail in the sections that follow. For all of these tests, the parameters in the activation function in (5.104) are specified as

$$\begin{aligned} \tau_{rise} &= 20 \times 10^{-3}\, s \quad , \\ \tau_{fall} &= 200 \times 10^{-3}\, s \quad , \\ \alpha_{min} &= 0 \quad , \\ \alpha_0 &= 0 \quad . \end{aligned} \tag{7.1}$$

Results of physical tests on the passive behaviour of musculoskeletal tissues in compression can be found in Grieve and Armstrong [50]. Some of the material parameters for this model are selected from physical tests on cardiac muscle tissue carried out by Humphrey et. al. [62, 63, 64, 65].

7.1 Uniaxial displacement tests

The uniaxial test is used to examine the most basic behaviour of the LMM. The size of the domain is $2 \times 2 \times 2$ length units. By symmetry, only a quarter of the domain, with dimensions $1 \times 1 \times 2$ length units is analysed. Symmetry boundary conditions are applied to the faces of the domain facing the negative X-direction and negative Y-direction, illustrated in Figure 7.1. On each of these faces, the displacement degree of freedom in the direction normal to the respective face was fixed to 0. A third face in the positive Z-direction in Figure 7.1), is fixed for the displacement degree of freedom in the Z-direction.

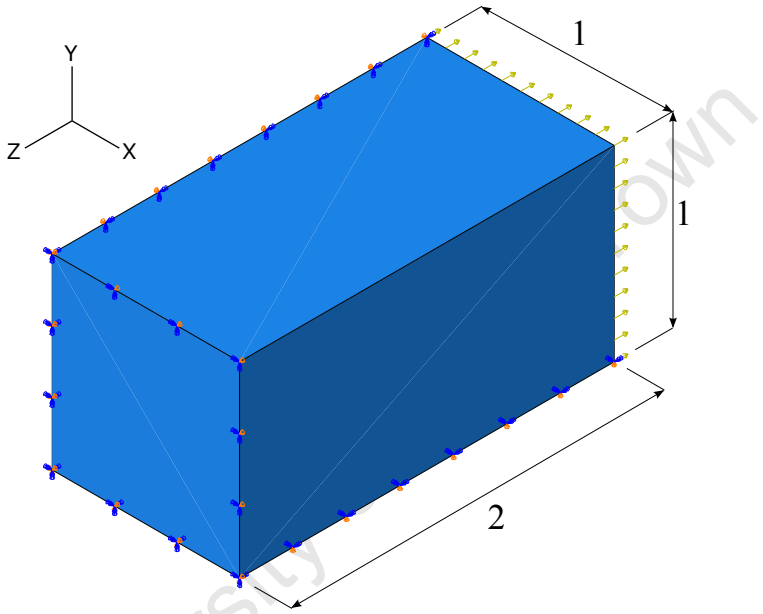

Figure 7.1: Boundary conditions and dimensions illustrated on the uniaxial domain in Abaqus.

A range of mesh sizes are used, from a single element, up to a mesh size of $10 \times 10 \times 20$, or 2000 elements. Values for Young's modulus, and Poisson's ratio are selected using Equation (5.134). Taking values for Humphrey's constants from (5.2.3), and for a selected value of $\nu = 0.45$, Young's modulus is given as $E \approx 26000\,Pa$. These properties are applied to the isotropic ground material, in which the fibres are embedded.

The unixial tests consist of the following loading conditions:

- isotropic behaviour, with external loading,
- passive muscle behaviour, with external loading,
- active muscle behaviour, without external loading,
- and active muscle behaviour, with external loading.

The uniaxial tests make use of mesh sizes ranging from a single element up to 2000 elements. A total uniaxial force of $\boldsymbol{P} = 1.3\,N$ was chosen as the external force for all the different uniaxial tests. This force is distributed uniformly according to nodal contributions. This applied force gives exactly 5% stretch for the uniaxial isotropic test, of all mesh sizes. For each mesh size, an average force of

$$\mathrm{F}_{\mathrm{node}} = \frac{1.3}{\text{number of nodes}}\,N\,, \tag{7.2}$$

was applied per node on the free axial face.

This gives an axial displacement solution of $0.001\,m$ for all nodes on the free axial face. The stress in this single element case is found to be $1300\,Pa$ for both the Abaqus standard C3D8 element, and and simplified isotropic LMM UEL. A nodal loading distribution with the size 16 mesh is illustrated as an example in Figure 7.2. The total force $\boldsymbol{P}$ is distributed as follows:

- $\mathbf{F}_1 = \frac{\boldsymbol{P}}{16}$ for nodes which have contributions from 1 element,
- $\mathbf{F}_2 = \frac{2\boldsymbol{P}}{16} = \frac{\boldsymbol{P}}{8}$ for nodes which have contributions from 2 elements,
- and $\mathbf{F}_3 = \frac{4\boldsymbol{P}}{16} = \frac{\boldsymbol{P}}{4}$ for nodes which have contributions from 4 elements.

The nodal loads for varying mesh sizes are distributed in a similar manner.

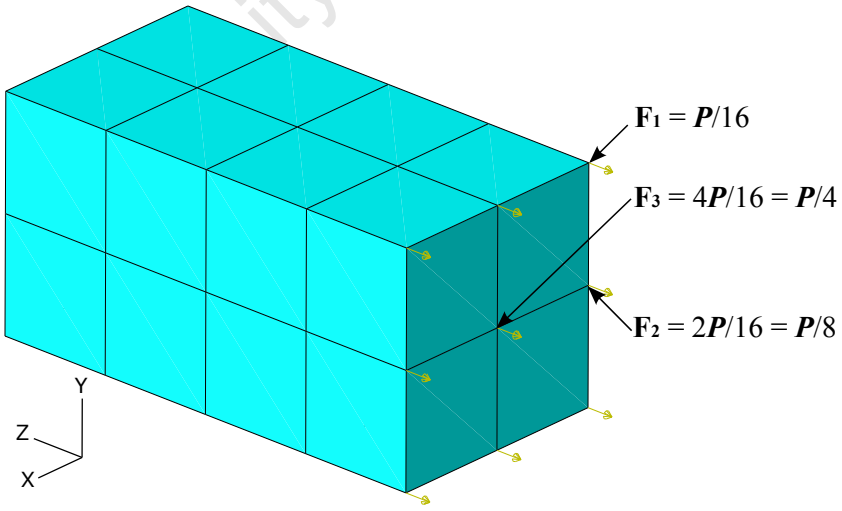

Figure 7.2: Nodal load distribution for uniaxial test.

For the anisotropic cases, a single set of material fibres are introduced in the Z-direction. For the cases with external loading, a normal tensile load is applied to the face in the positive Z-direction. This setup, as well as that with no external loading, is illustrated in the equivalent two-dimensional representation in Figure 7.3.

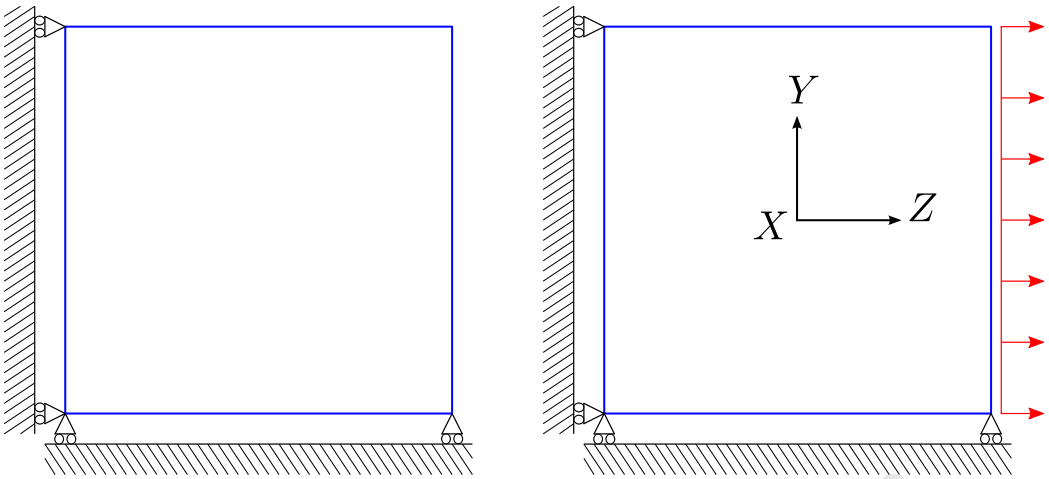

(a) Single element constraints, with no external loading.

(b) Single element constraints, uniaxially loaded.

Figure 7.3: Two-dimensional representation of the uniaxial test constraints with and without external loading.

7.1.1 Isotropic uniaxial test

The uniaxial isotropic test was done using the LMM UEL element and compared to the behaviour of the Abaqus standard hexahedral C3D8 element, under similar loading. The effects of muscle fibres are removed from the formulation by setting T_0 to zero, simplifying the formulation to an isotropic level. This test shows identical results for the LMM UEL and the Abaqus standard C3D8 element types for the variety of mesh sizes used. A summary of the results for the maximum displacement of all nodes on free face are shown in Table 7.1.

Table 7.1: Displacement results for the uniaxial isotropic test.

number of elements	average force per node (N)	Abaqus C3D8 displacement (m)	LMM UEL displacement (m)	displacement difference %
1	0.03250	1.000×10^{-3}	1.000×10^{-3}	0.00%
16	0.01444	1.000×10^{-3}	1.000×10^{-3}	0.00%
128	0.00520	1.000×10^{-3}	1.000×10^{-3}	0.00%
2000	0.00107	1.000×10^{-3}	1.000×10^{-3}	0.00%

The displacement contours of the mesh with 2000 elements for the Abaqus standard C3D8 are displayed in Figure 7.4(a), and for the LMM UEL in Figure 7.4(b). From these figures, it can be seen that the displacement contours for the LMM UEL are visually similar to the C3D8 results. Numerically, the displacement results for the two element types are 100% identical.

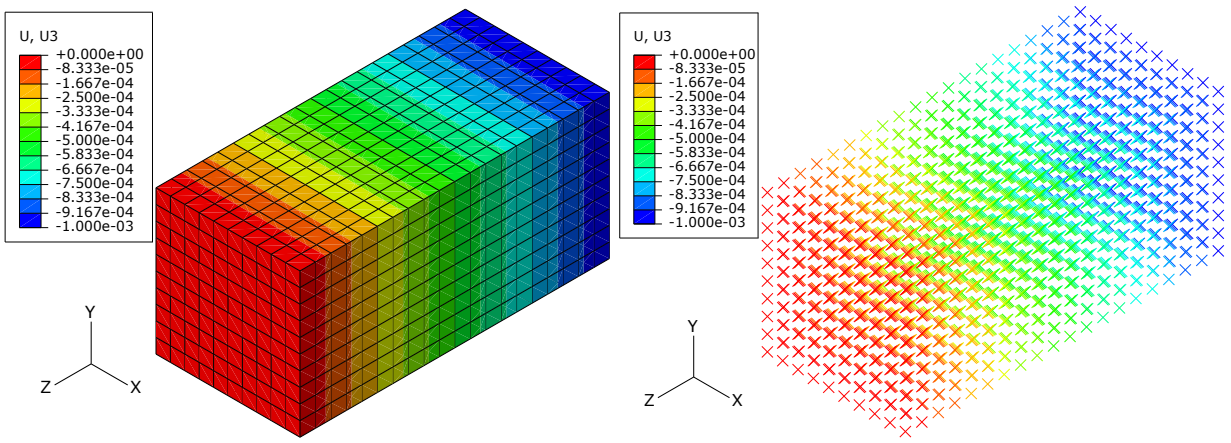

(a) Displacement contour for C3D8

(b) Displacement contour for LMM UEL.

Figure 7.4: Displacement contours for C3D8 and LMM UEL isotropic uniaxial tests.

7.1.2 Passive uniaxial test

A series of tests were run to examine the effects of the passive muscle fibres present in the isotropic ground matrix. For these passive tests, the activation function, $\alpha(t)$ is set to approximately zero. This ensures that the SE and CE contributions to stress are nullified, while the PE contribution is still taken into account. It should be noted that the value of T_0 selected affects not only the active performance of the model, but also the passive performance. T_0 was selected to be 68.20 gf/cm^2, or 1% of the values specified in Martins.

The fibres are set to each of the three base directions in successive tests, and loaded uniaxially. In the first test, the fibres lie in the same direction as the applied load, i.e. the Z-direction. In the remaining two tests, the fibres are aligned in the X- and Y-directions, respectively, each orthogonal to the applied load. The displacement results of all nodes on the free axial face for the passive fibre tests are summarized in Table 7.2.

Table 7.2: Uniaxial passive displacement results.

Fibre direction	displacement in X (m)	displacement in Y (m)	displacement in Z (m)
X	-4.391×10^{-5}	-7.812×10^{-5}	-2.788×10^{-4}
Y	-7.812×10^{-5}	-4.391×10^{-5}	-2.788×10^{-4}
Z	-4.391×10^{-5}	-4.391×10^{-5}	-1.951×10^{-4}
isotropic	-2.250×10^{-4}	-2.250×10^{-4}	-1.000×10^{-3}

The displacement results for the test with fibre in the X-direction are shown in Figure 7.5. It should be noted that the displacements are exaggerated in these illustrations. It can be seen from these results that the displacement in the Y-direction is higher than the displacement in the X-direction.

The shape of the deformed mesh also indicates more displacement in the Y-direction compared to the X-direction. This means that the fibres add stiffness in the direction along their axes, so that the overall material is stiffer in the fibre direction.

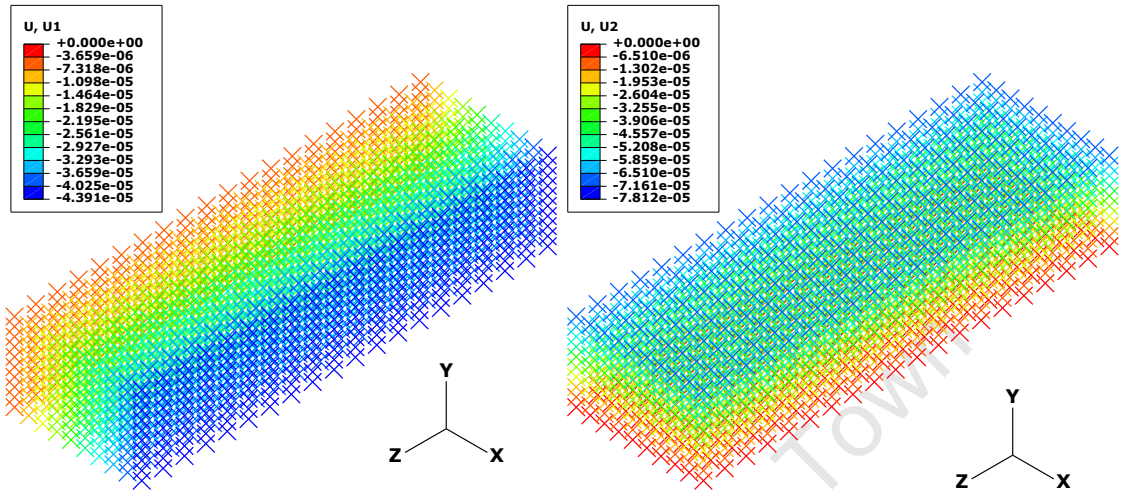

(a) X-displacement contour (b) Y-Displacement contour

Figure 7.5: Displacement contours with passive fibres in X-direction, and load in Z-direction.

The displacement results for the test with fibre in the Y-direction are shown in Figure 7.6. It can be seen from these results that the displacement in the X-direction now, is higher than the displacement in the Y-direction. The shape of the deformed mesh also indicates more displacement in the X-direction compared to the Y-direction. The material is now stiffer in the Y-direction.

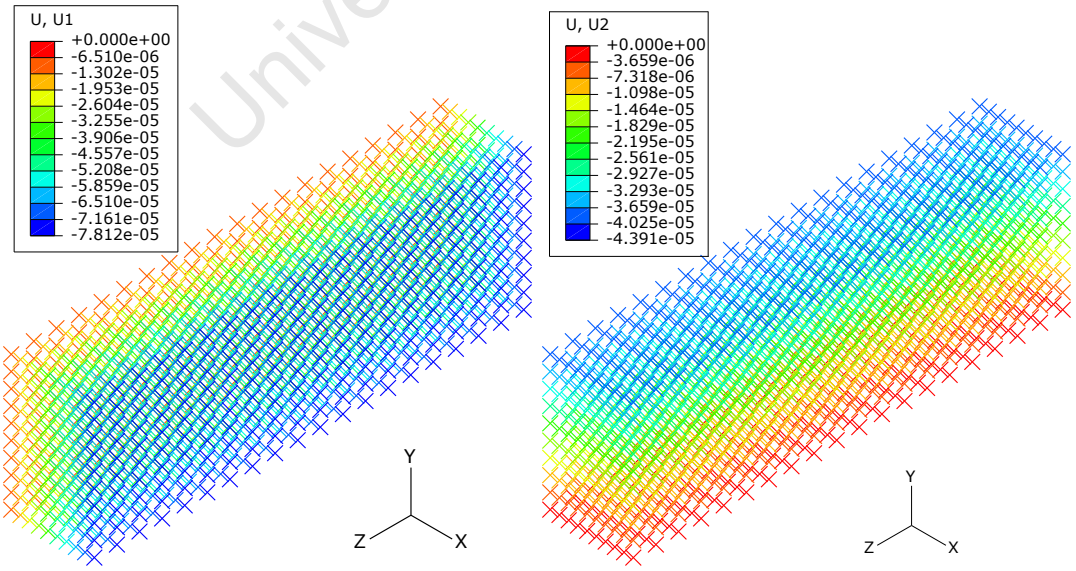

(a) X-displacement contour (b) Y-Displacement contour

Figure 7.6: Displacement contours with passive fibres in Y-direction, and load in Z-direction.

The displacement results for the test with fibre in the Z-direction are shown in Figure 7.7. It can be seen from these results that the displacement in the X-direction now, is identical to the displacement in the Y-direction. The material is now stiffer in the Z-direction, the direction in which the force is applied. From all of these results, it is evident that the passive fibres have a transverse isotropic effect on the behaviour of the model.

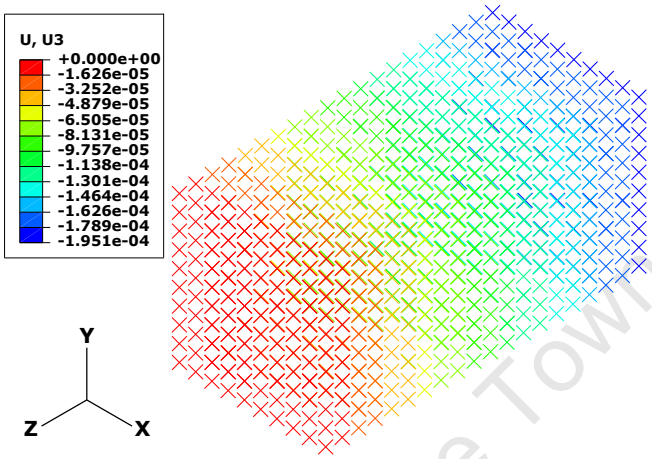

Figure 7.7: Displacement contours with passive fibres in Z-direction and load in Z-direction.

7.1.3 Body force test

A body force is a force that acts throughout the volume of a body, and includes forces such as gravity. The user element subroutine UEL does not allow the application of body force terms in the conventional manner in Abaqus. Instead, the body force term is programmed into the finite element formulation for the LMM UEL. A basic validation test is performed on the mesh of 2000 elements in uniaxial tension, the only force applied being the body force. The dimensions of the domain are $0.01\ m\ \times\ 0.01\ m\ \times\ 0.02\ m$, the longest length being in the Z-direction.

The results for the displacement of the LMM UEL under a body force are compared with the Abaqus standard C3D8 hexahedral element under a standard body force. The LMM UEL is set to be isotropic for this test, to closely match the standard element. Young's modulus is set to 26000 Pa, and Poisson's ratio is set to 0.45.

Results for the displacement of the mesh under application of a body force, simulating gravity, for the LMM UEL and C3D8 element types are shown to be identical. A displacement of $8.1 \times 10^{-5}\ m$ occurs under the application of a body force of $-9.81\ ms^{-2}$ in the Z-direction. The results for the displacements are shown as contours in Figure 7.8(a) for the Abaqus standard element, and Figure 7.8(b), for the LMM UEL. From these figures, it can be seen that the results are identical for each case.

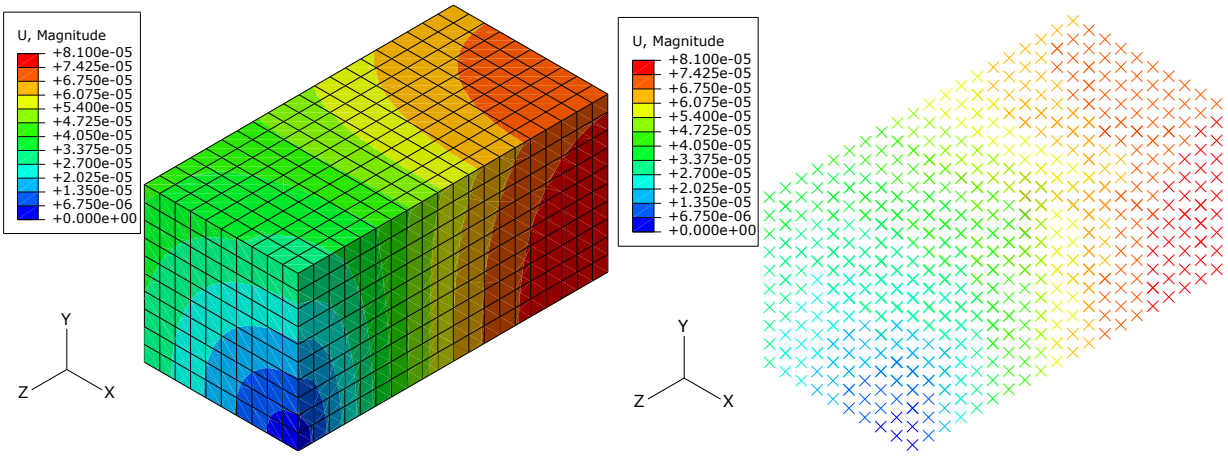

(a) Displacement contour of standard element isotropic uniaxial test with body force

(b) Displacement contour of UEL isotropic uniaxial test with body force

Figure 7.8: Displacement contour of isotropic uniaxial test with body force applied (2000 elements).

A test was done with a domain size of $1 \times 1 \times 2\,m$. The displacement effect of the body force on this domain is illustrated in Figure 7.9. It can be seen, that since the domain is larger, the volume is larger, and hence the body force increases proportionally, and hence the dramatic increase in displacement.

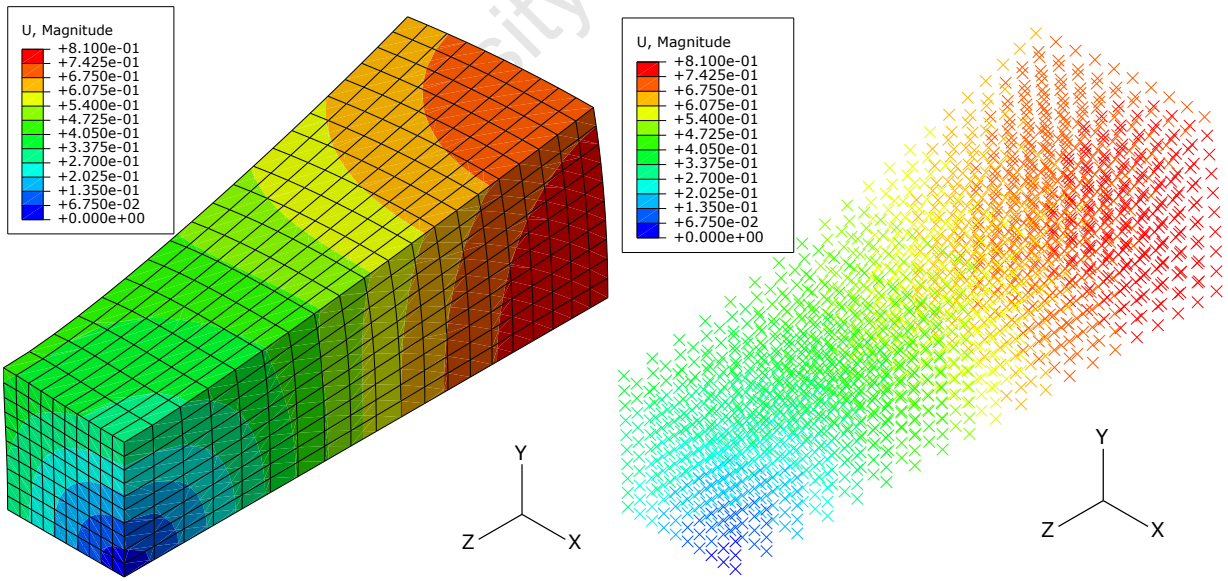

(a) Displacement contour of standard element isotropic uniaxial test with body force

(b) Displacement contour of UEL isotropic uniaxial test with body force

Figure 7.9: Displacement contour of isotropic uniaxial test with body force.

7.1.4 Active uniaxial test

In this test, the muscle fibres are aligned with the Z-direction and are activated according to the activation function in (5.131). $T_0 = 68.20\,gf/cm^2$ is scaled down to 1% of the value specified in Martins et. al. [88]. The domain, and boundary conditions are the same as the isotropic and passive tests. This activation test is carried out with and without the external load, and the respective results are then compared. The Z-displacement contour for the active uniaxial test with no external loading and 2000 elements is displayed in Figure 7.10.

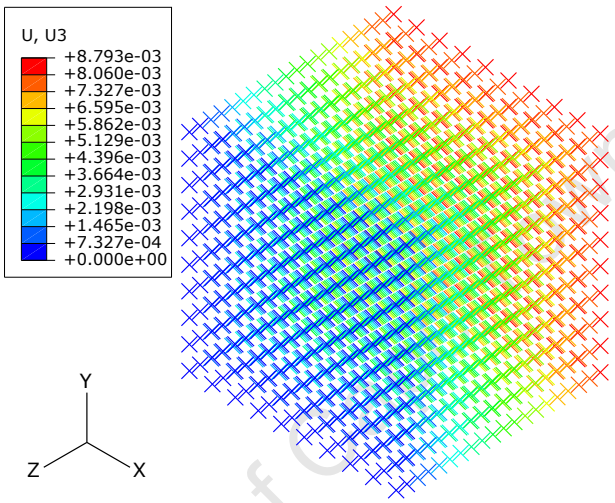

Figure 7.10: Displacement contour of UEL active uniaxial test with no external load (2000 elements).

The stress history of the active LMM UEL uniaxial test with no external load is displayed in Figure 7.11. It is evident that the stress response over time is directly related to the activation function applied in (5.131).

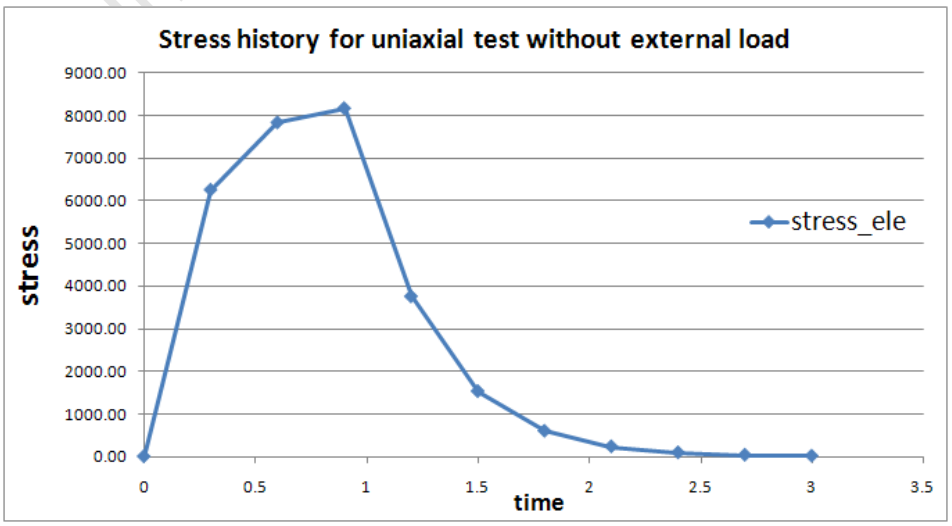

Figure 7.11: Stress history of active UEL uniaxial test with no external load.

The strain history of an active UEL uniaxial test with no external load is displayed in Figure 7.12. The strain in the CE is in direct opposition to the overall strain in the element, and the counteract each other, giving a net strain of approximately zero in the SE.

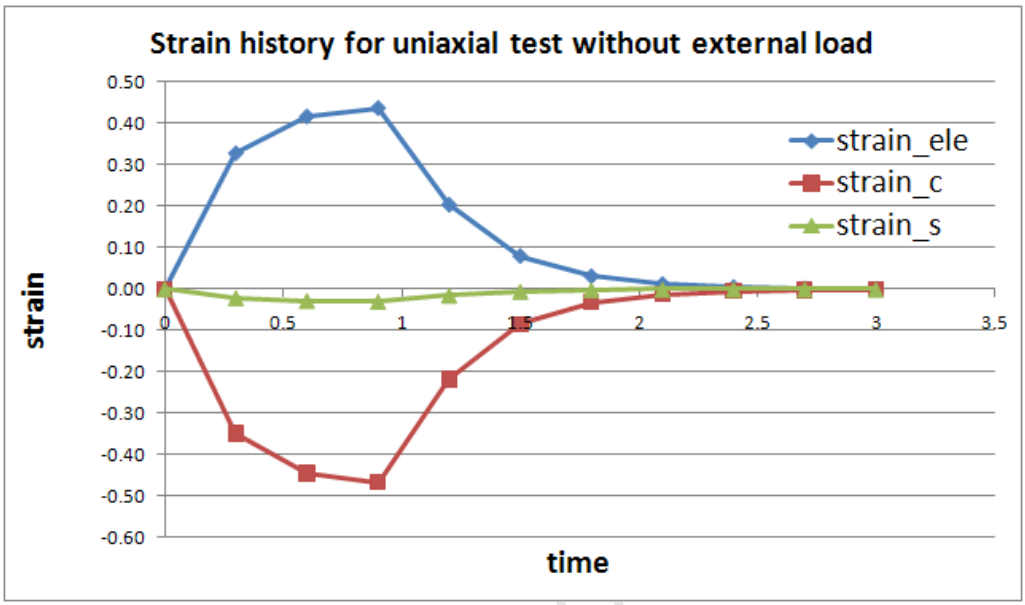

Figure 7.12: Strain history of active UEL uniaxial test with no external load.

The Z-displacement contour for the active uniaxial test with external contractile load and 2000 elements is displayed in Figure 7.13.

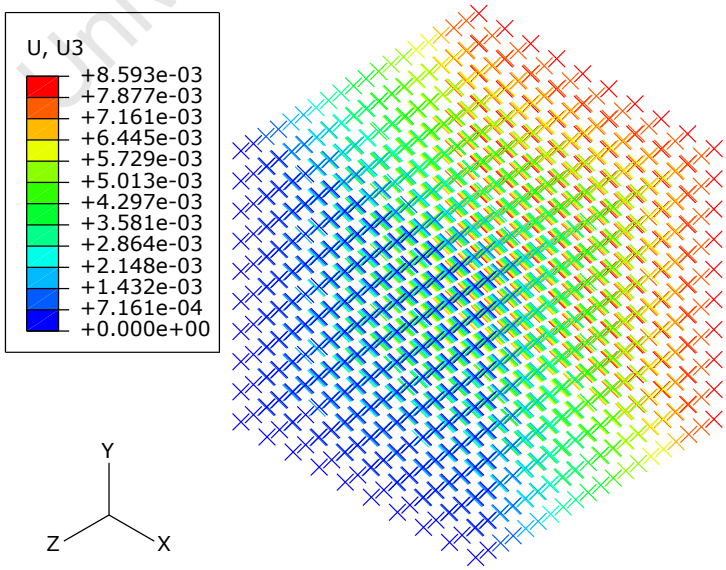

Figure 7.13: Displacement contour of UEL active uniaxial test with external load (2000 elements).

The stress history of an active UEL uniaxial test with and without external contractile load is displayed in Figure 7.14 along with passive and isotropic stress. Here, it appears that the stress from the activation and the external loads are additive. It should be noted that for this case, $T_0 = 68.2\, gf/cm^2$.

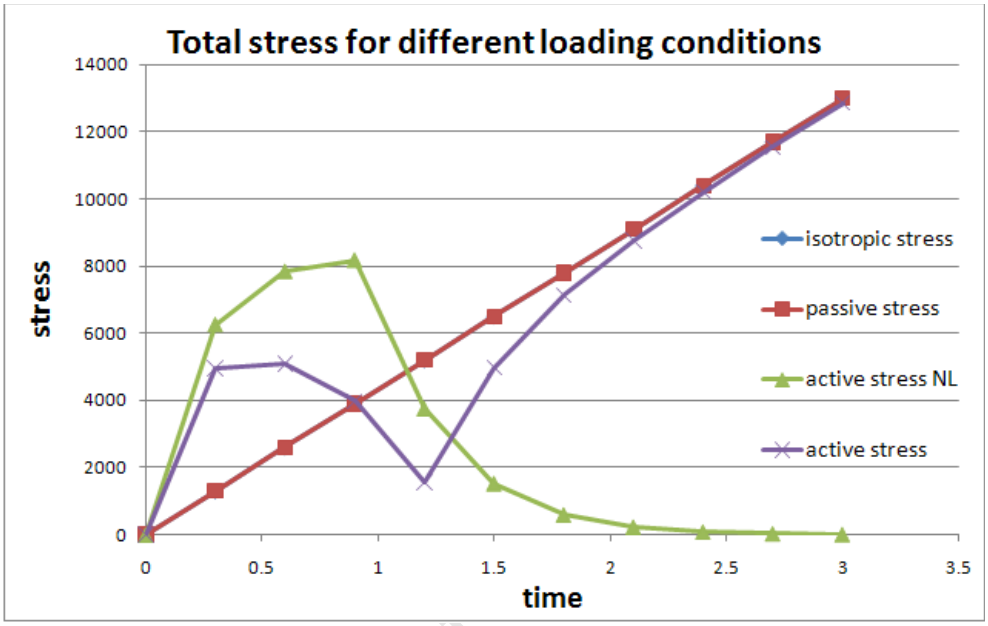

Figure 7.14: Active and passive stress history under combined external loading and muscle activation. Active stress NL is the stress history of an active muscle with no external load applied. The isotropic stress and the passive stress histories are similar.

The results of the uniaxial tests for the maximum displacements in the Z-direction are summarized in Table 7.3. From these results, it can be seen that loading cases 2 (passive externally loaded) and 3 (active with no load) add to give the same result as in loading case 1 (active with external load). These results are indicative of the additivity of the muscle activation force and the externally applied load.

Table 7.3: Summary of results for the uniaxial displacement tests.

Loading condition	case number	maximum Z-displacement (m)
active Z-fibre with external load	1	$+8.593 \times 10^{-3}$
active Z-fibre with no external load	2	$+8.793 \times 10^{-3}$
passive Z-fibre with external load	3	-1.951×10^{-4}
isotropic with external load	4	-1.000×10^{-3}
difference between cases 1 and 3	5	-8.778×10^{-3}

7.2 Cook's membrane test

The Cook's membrane problem is a standard model for testing combined bending and shear response with moderate distortion. It consists of a tapered panel of elements fixed for all degrees of freedom on the left face while a shear traction $\boldsymbol{P}$ is applied on the opposite face (see Figure 7.15).

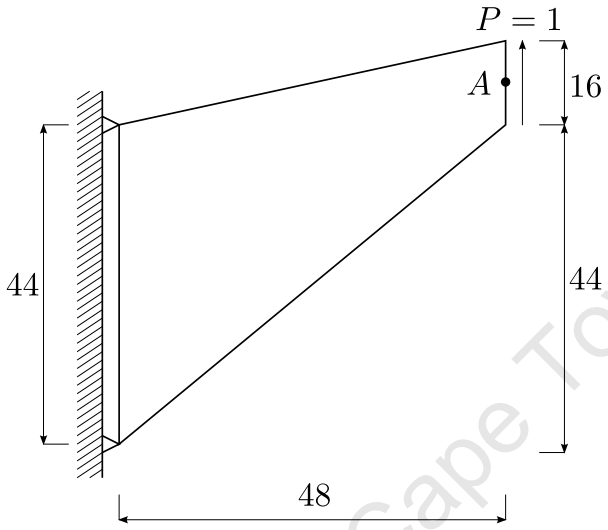

Figure 7.15: Illustration of Cook's membrane test geometrical setup.

Due to the limitation of Abaqus user element subroutines not allowing the application of surface tractions, the shear force is replaced with direct forces on individual nodes, of an accumulated equivalent value. For this test, Young's modulus is set to $1\,Pa$, and Poisson's ratio is set to 0.3. The panel measures 44 units on the left-hand side and 16 units on the right-hand side. The two sides are parallel and 48 units apart. The top right-hand corner is initially 16 units above the top left-hand corner. When solving the problem with three-dimensional elements, a thickness of 1 unit is assumed. The problem is solved for vertical displacement at point A in Figure 7.15, the middle node of the right face.

7.2.1 Results and discussion

This benchmark test was run for increasing mesh sizes as follows:

- size 2 implies $2 \times 2 \times 2$ elements,
- size 4 implies $4 \times 4 \times 2$ elements,
- size 8 implies $8 \times 8 \times 2$ elements,
- size 16 implies $16 \times 16 \times 2$ elements (Figure 7.16).

The boundary conditions and undeformed mesh for the size 16 mesh problem are illustrated in Figure 7.16.

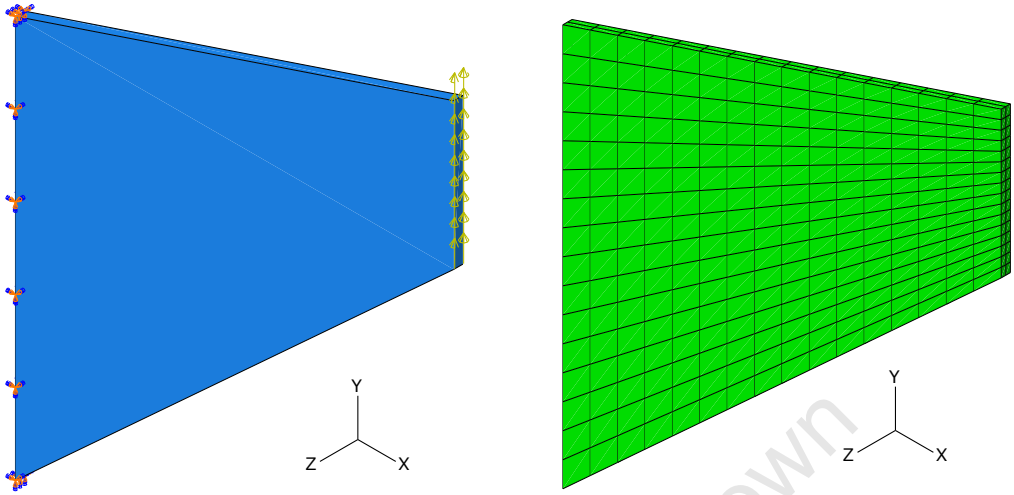

(a) Cook membrane with boundary conditions. (b) Cook membrane size 16 Mesh.

Figure 7.16: Cook membrane boundary conditions and mesh.

The Cook's membrane test was run on Abaqus standard element C3D8, and then also on the LMM UEL with isotropic behaviour (no passive muscle fibres or muscle activation). The results of the vertical displacement of point A of the Cook's membrane test are summarised in Table 7.4. The results obtained for the LMM UEL are comparable to those in the literature, and to standard element types available in Abaqus and deal.II.

Table 7.4: Vertical displacement results at point A (Figure 7.15) for Cook's membrane test.

Element type	mesh size $2 \times 2 \times 2$	mesh size $4 \times 4 \times 2$	mesh size $8 \times 8 \times 2$	mesh size $16 \times 16 \times 2$
LMM UEL (Isotropic)	6.990	11.875.70	17.123	20.454
Abaqus standard C3D8 hexahedral	13.571	18.751	20.979	21.668
HEXA8 hexahedral (used by Ooi [104])	11.21	17.64	21.70	23.24
deal.II standard hexahedral	10.97	17.33	21.55	23.21

Figure 7.17 shows convergence of the solution as the number of elements increases, for all element types tested. The HEXA8 hexahedral type element is an 8-noded hexahedral element developed by Ooi et. al. [104]. The C3D8 hexahedral type element is an 8-noded hexahedral element, with selective reduced integration, used for comparison of results in Abaqus. The reference solution is given as 23.9 units of vertical displacement at point A [104].

The LMM UEL converges at a slower rate (in number of elements) relative to the other elements tested. This difference in convergence rates can be explained by the fact that the Abaqus standard

element formulation uses selectively reduced integration, but the LMM UEL developed here does not. Selective reduced integration has a major effect on stiffness in bending. This explains why pure axial tests and also, pure shear tests give identical results, but the Cook's membrane test, which involves mainly bending differ for the various elements.

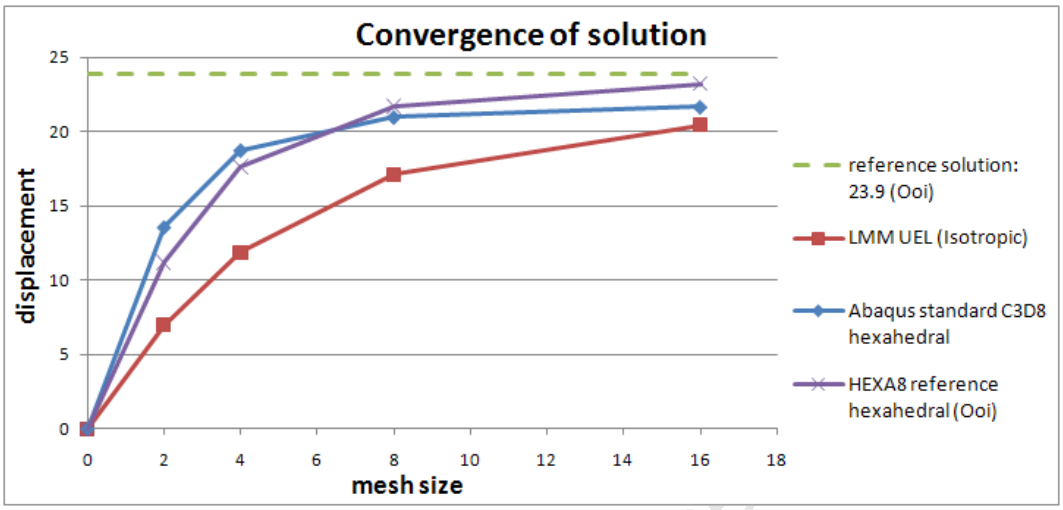

Figure 7.17: Convergence of solution to Cook's membrane test for various element types as the number of elements increases.

The displacement contours for the Cook's membrane problem using a size 16 mesh with Abaqus standard C3D8 elements and isotropic LMM UEL elements in Figure 7.18.

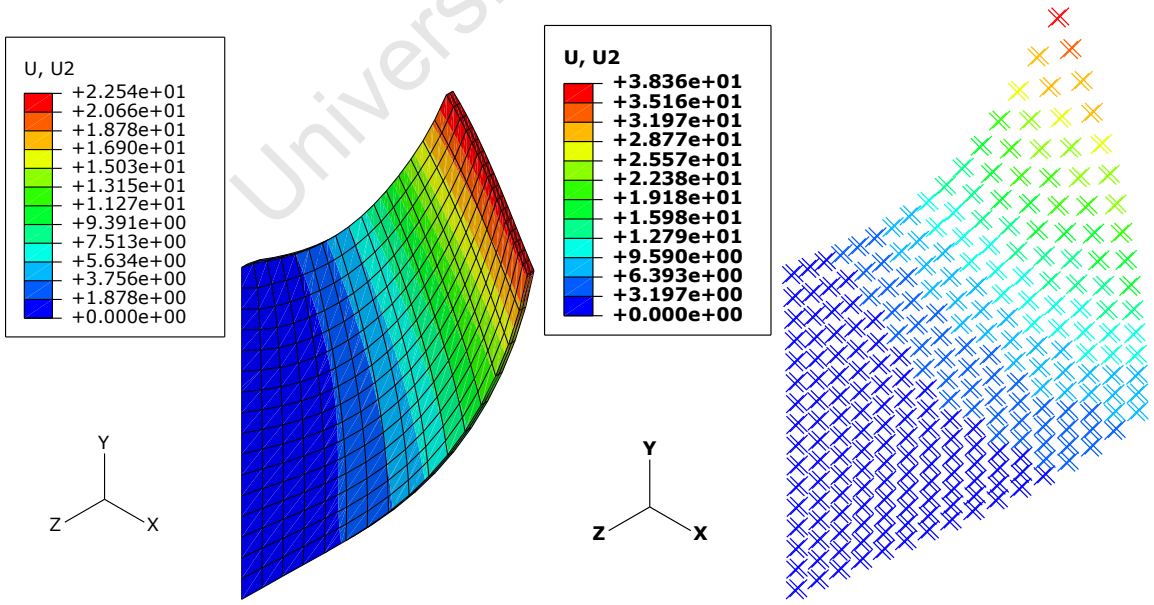

(a) Using Abaqus standard element

(b) Using LMM UEL

Figure 7.18: Displacement contours of Cook's membrane problem size 16 mesh.

7.3 Isometric contraction test

In the isometric contraction test, a square membrane is subjected to activation with all the boundaries the X- and Y-directions being fixed as illustrated in Figure 7.19(a). The size of the domain is $0.01m \times 0.01m$ and $0.001m$ thick. A complete neural excitation is applied for a period of $1\,s$ at $t = 0$ and then removed at $t = 1$. The isometric test presented in Martins [88], uses a size 14 mesh (i.e. $14 \times 14 \times 2$) of triangular elements, and is a planar problem. Since the LMM UEL is a hexahedral type element, and not planar as in the Martins' tests, the test setup is adapted for use with hexahedral type elements, by adjusting the boundary conditions.

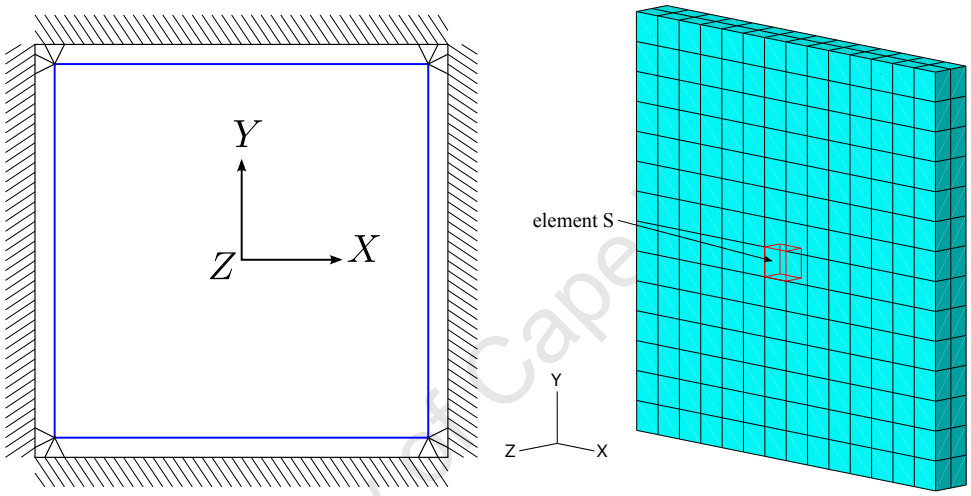

(a) Constraints for the isometric test. (b) The $14 \times 14 \times 2$ element mesh.

Figure 7.19: Illustration of the constraints and mesh used for the isometric test.

A fixed displacement constraint which prevents motion in the third direction is applied to the faces in the Z-direction, to make the problem one of plane stress (allowing motion only in the $X - Y$ plane). Also, since the LMM uses hexahedral elements, the size 14 mesh consists of fewer elements than the triangular size 14 mesh used by Martins. The $14 \times 14 \times 2$ element mesh used for the isometric test is illustrated in Figure 7.19(b). Since there are no external loads applied for an isometric test, only active tests are performed for this problem. The muscle fibres are set to the X-direction, and $T_0 = 6820\,gf/cm^2$, as in Martins' test.

7.3.1 Results and discussion

The results for the isometric tests are presented here. Since the length of the domain is fixed in the fibre direction, the displacement is zero, and the stress history result is found to be directly dependent on the activation function. This corresponds to the results obtained from the isometric test performed by Martins et. al. [88]. It is clear from their numerical values of the results that the displacements here are insignificant.

The active isometric stress history is given in Figure 7.20. It this graph, it can be seen that the stress is directly related to the activation function, just as in Martins' results.

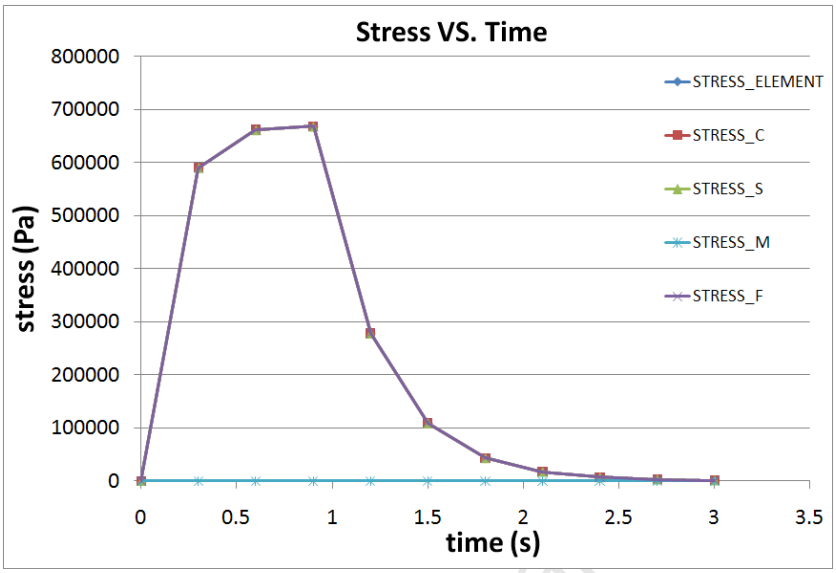

Figure 7.20: Active isometric stress history.

The active isometric strain history is given in Figure 7.21. It can be seen from this graph that the strains in the CE and SE are also directly related to the activation function, but the overall strain in the element is zero.

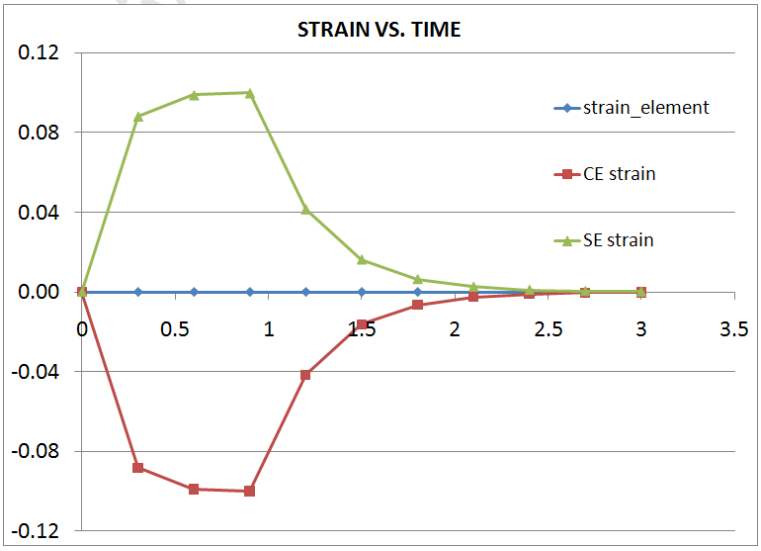

Figure 7.21: Active isometric strain history.

7.4 Isotonic contraction test

A square membrane is subjected to an isotonic contraction along the X-direction, and allowed to deform freely in the Y-direction. All the nodes on the left face are fixed in the X-direction, and the middle node on this face, is fully fixed in all directions. These constraints are illustrated in Figure 7.22(a). The muscle activation parameter is selected as $T_0 = 68.20\,gf/cm^2$, i.e. 1% of the value specified in Martins' work. The $14 \times 14 \times 2$ mesh illustrated in Figure 7.22(b), is used for the isotonic test, and is identical to the one used for the isometric test.

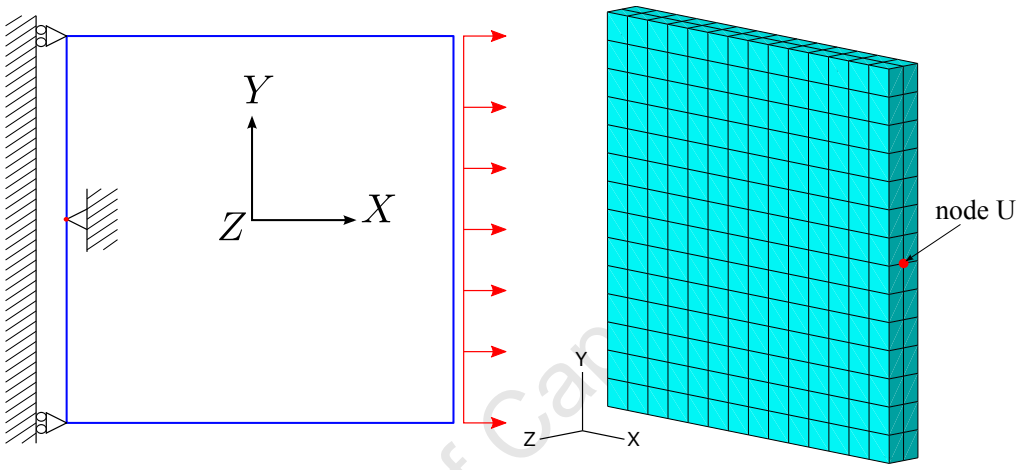

(a) Constraints for the isotonic test (b) Mesh used for isotonic test

Figure 7.22: Illustration of the constraints and mesh for the isotonic test.

The muscle fibres are set to be in the direction of the applied load, i.e., the X-direction. The activation function is the same as the one introduced in (5.131), but is applied at $t = 1\,s$. The start of the activation is hence applied at the moment when the tensile force reaches its maximum also at $t = 1\,s$, and stops $1\,s$ later at $t = 2\,s$. This isotonic activation history is illustrated in Figure 7.23.

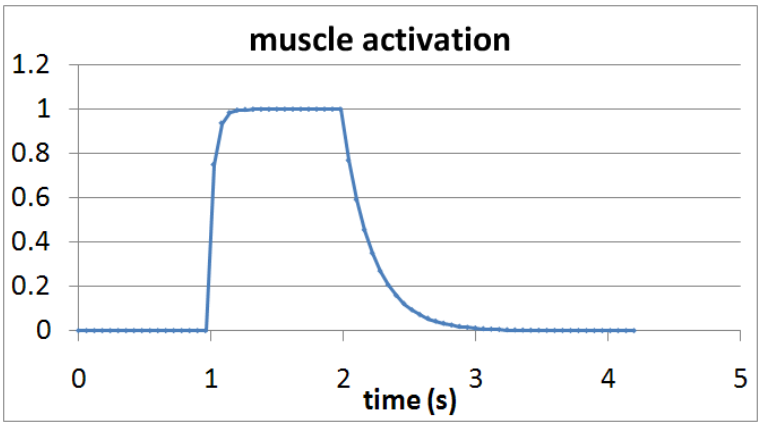

Figure 7.23: Isotonic muscle activation history.

The boundary conditions imposed on this domain are different, however. The displacement of Node U, indicated in Figure 7.22(b), is used for these results. A tensile force is applied in the X-direction to the right face. This tensile load grows linearly from zero over the first second until it reaches a maximum value equivalent to $4.9\,gf/cm$ used by Martins [88]. Thereafter, the load remains constant till the end of the test at $t = 4.2\,s$.

7.4.1 Results and discussion

The passive isotonic stress history for $T_0 = 68.2\,gf/cm^2$, for element S, highlighted in Figure 7.19(b), is illustrated in Figure 7.24 (a). The active isotonic displacement history for a test with reduced activation (0.1%), i.e. $T_0 = 6.82\,gf/cm^2$, and external load is illustrated in Figure 7.24 (b). This is indicative of eccentric muscle contraction, where the muscle lengthens under external loading and muscle contraction. The active isotonic displacement history for a test with reduced activation (1%), i.e. $T_0 = 68.2\,gf/cm^2$, and external load is illustrated in Figure 7.24 (c). This is indicative of concentric muscle contraction. For concentric muscle contraction, the length of a muscle reduces under external loading and muscle contraction. The concentric contraction occurs when the muscle is active, i.e., between $t = 1\,s$, and $t = 2\,s$. During this period, the stress in the muscle is reduced, and the muscle contracts. Immediately after the completion of the activation, the displacement increases back to the value obtained just before activation had started. The slopes of the curves, for the period up to 1 second, for case (b) is steeper than cases (a) and (c), due to the change in T_0, as the muscle is less stiff for smaller T_0 values.

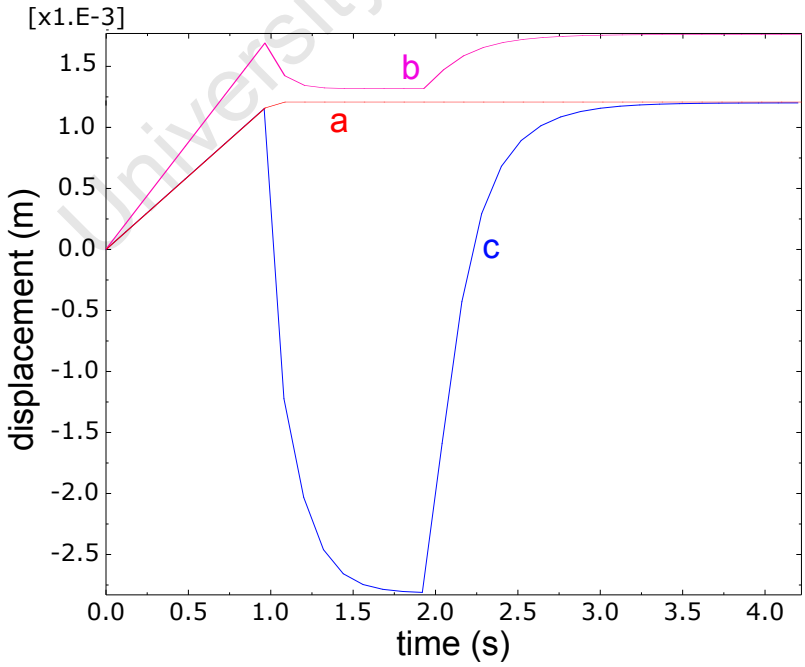

Figure 7.24: Isotonic stress history for (a) passive muscle, (b) 0.1% activated muscle with eccentric behaviour, and (c) 1% activated muscle with concentric behaviour.

The active isotonic displacement history for concentric muscle behaviour with full activation, (100%) i.e. $T_0 = 6820\,gf/cm^2$, is illustrated in Figure 7.25.

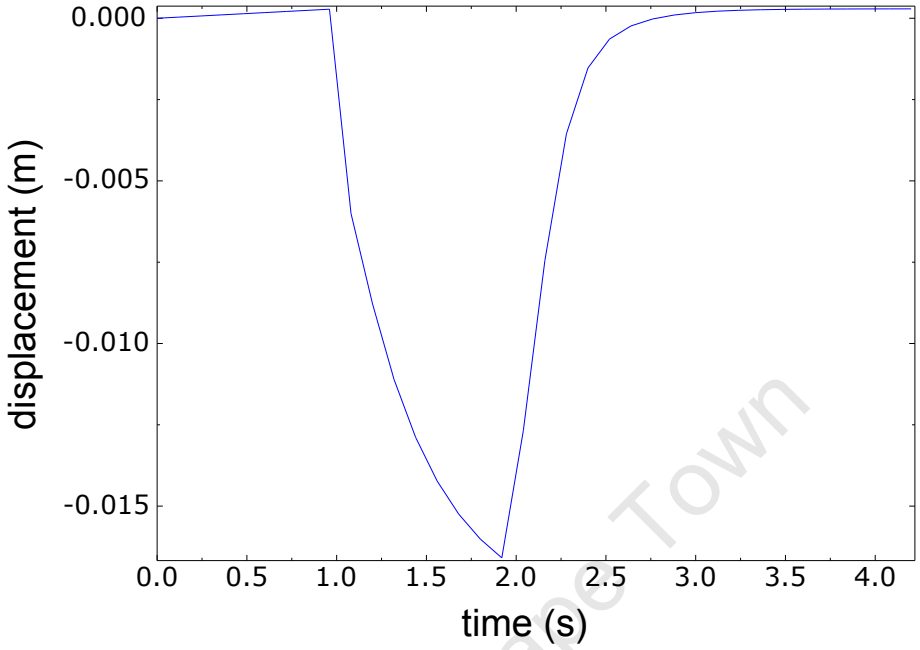

Figure 7.25: Isotonic displacement showing concentric muscle behaviour for 100% activation force.

The displacement contours for the isotropic C3D8 element under the same external loading as in the isotonic tests are displayed in Figure 7.26. This was compared to the isotropic LMM UEL under the same loading, and the results were found to be identical.

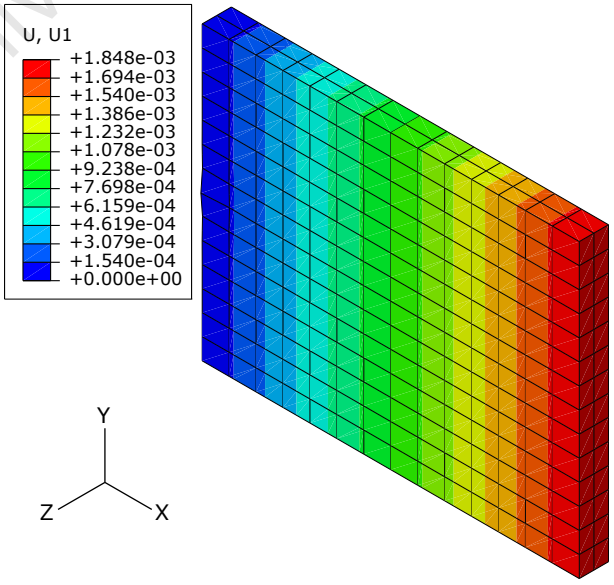

Figure 7.26: Displacement contour for C3D8 element with no active contraction.

The displacement contours for the LMM UEL under 100% isotonic contraction are displayed in Figure 7.27.

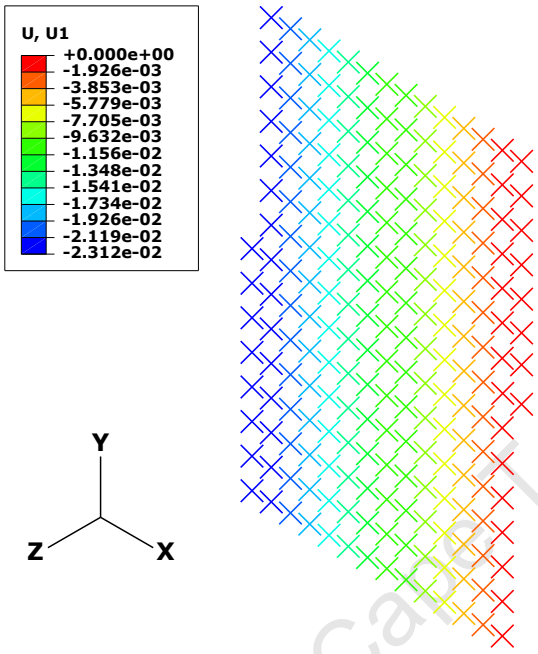

Figure 7.27: Displacement contour for LMM UEL with 100% active contraction (concentric).

The displacement contours for the LMM UEL under 1% isotonic contraction are displayed in Figure 7.28.

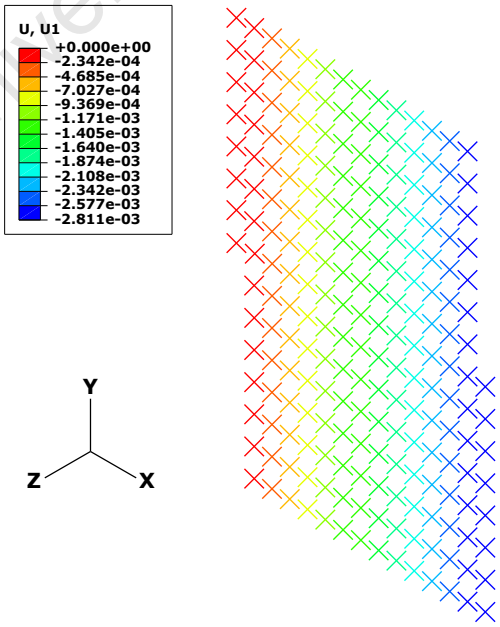

Figure 7.28: Displacement contour for LMM UEL with 1% active contraction (concentric).

The displacement contours for the LMM UEL under 0.1% isotonic contraction are displayed in Figure 7.29.

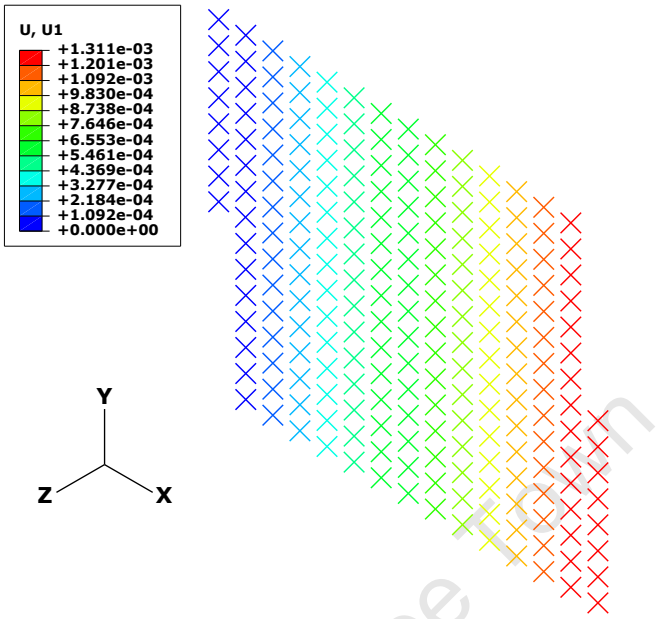

Figure 7.29: Displacement contour for LMM UEL with 0.1% active contraction (eccentric).

The results and behaviour for all of these isotonic tests are similar to those found in Martins' work. As the contractile activation force is reduced from 100% to 0.1%, the peak stress is reduced and the displacement at peak stress is also reduced.

8 FEA Results and Discussion

The results for the FEA of the model of the human tongue are presented in this chapter. It is widely believed that the OSA event is highly influenced by gravity, low airway pressure during inspiration, and reduced muscle tone, amongst others. Some of these effects are tested using the tongue geometry and linearized muscle model (LMM) presented in previous chapters. The LMM is tested in levels of increasing complexity, starting from the most basic isotropic (without fibres) case under gravitational load. The case with all muscle fibre groups being passive is then tested under the same gravitational loading condition. The muscle model parameters were given in 5.2.3, and for a selected Poisson's ratio of $\nu = 0.45$, Young's modulus is given as $E \approx 26000\ Pa$ according to the relationship given in 5.134.

The activation of individual muscle groups on the movement of the tongue are also tested, firstly without gravitational loading, then also under gravitational loading. The activation function used for these tests is the same as that introduced in Figure 7.23 for isotonic tests, and is based on the work of Martins [88, 89]. In addition, the activation stress parameter is given as $T_0 = 68.20\ gf/cm^2$, i.e. 1% of the activation level specified in Martins' work. The behaviour of the model can be qualitatively compared to the work on pelvic floor muscles presented by Martins. Although airway pressure is a significant contributor to OSA, it is not modelled in these simulations as the focus of this work is on muscle fibre directionality under gravitational loading and how this relates to OSA.

One of the main objectives of these simulations is to examine the effects of individual muscle fibre groups on OSA, or more specifically, on the constriction of the airway. This is done by monitoring a point on the back of the tongue model under various loading conditions and muscle activity, and comparing the results. Some of those muscle groups which have a significant effect on reducing the constriction are then combined and activated simultaneously. Another objective would be to observe, qualitatively, the behaviour of the tongue during activation of individual muscle fibre groups. This would give insight into the role of each muscle group in the kinematics of the tongue.

8.1 Smoothed mesh of the tongue

A mesh of the right sagittal half of the tongue, generated from the geometrical data of the VHP and smoothed and processed in ParaView, is illustrated in Figure 8.1. The tongue and loading conditions are assumed to be symmetrical about the mid-sagittal plane. This mesh of the tongue consists of 4800 hexahedral elements. The actual element type can be specified as standard Abaqus hexahedral elements, such as the C3D8, or the LMM UEL element type presented here.

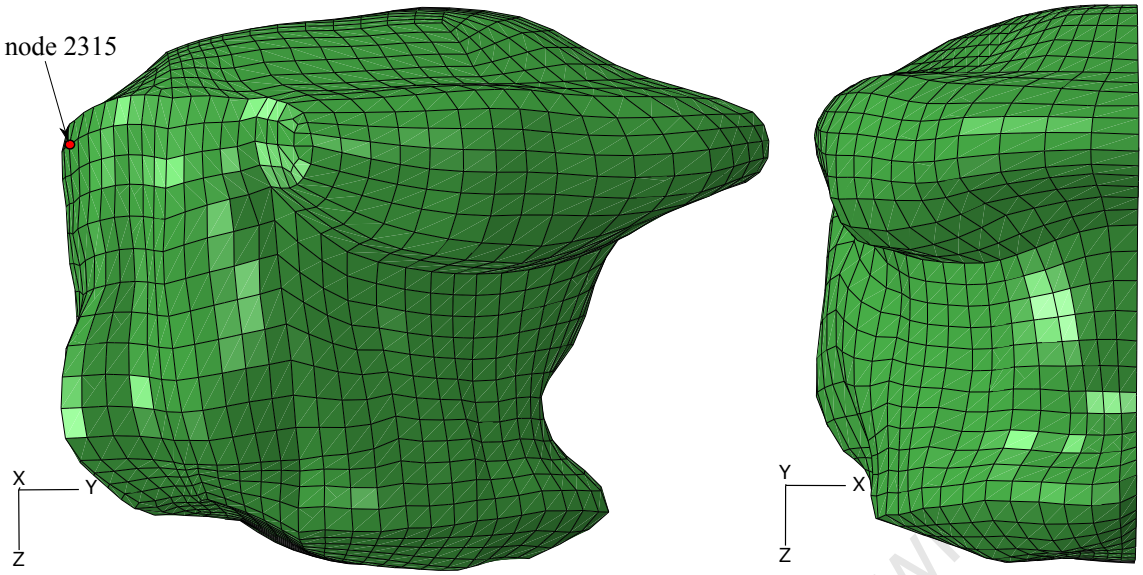

Figure 8.1: Smoothed mesh of the right half of the tongue (4800 elements).

8.1.1 Boundary conditions

The mid-plane of the tongue geometry is fixed in the X-direction for symmetry. This boundary condition is illustrated in Figure 8.2. A node (node number 2315) near the back of the tongue and highlighted in Figure 8.1, was selected for monitoring. This node was selected due to its location near the unconstrained posterior part of the tongue, where maximum displacement of tongue material might occur. All other nodes in the mesh are monitored as well.

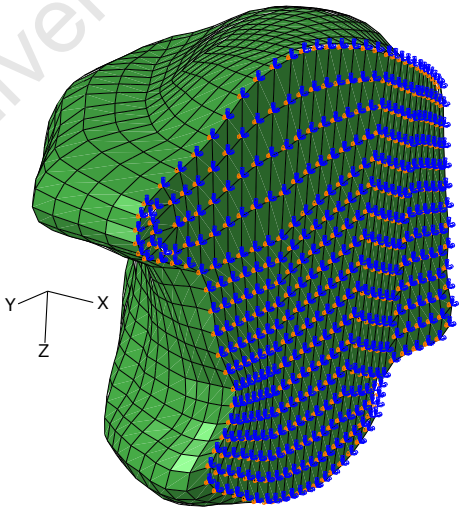

Figure 8.2: Symmetry boundary condition for the tongue mesh.

The attachment points of the tongue to the mandible and hyoid bones are fully fixed for all degrees of freedom. These boundary conditions are illustrated in Figure 8.3.

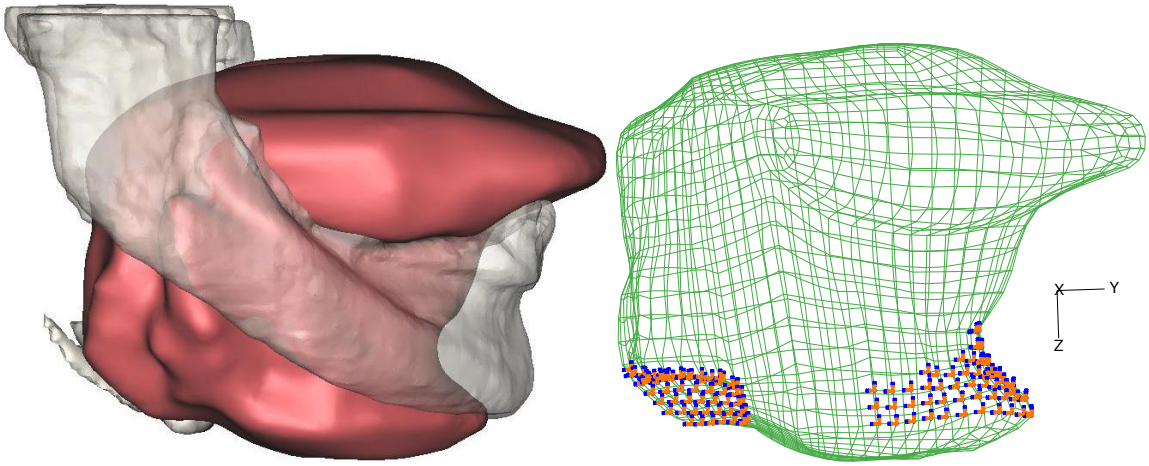

(a) Tongue with hyoid and mandible. (b) Fully constrained boundary nodes.

Figure 8.3: Muscle attachment boundary condition for the tongue mesh.

8.2 Isotropic and passive tongue under gravity

This test uses the tongue mesh, set to be isotropic (i.e. without the effect of muscle fibres), and under gravitational loading. There are two test cases, one simulating a person in the standing position with gravity in the Z-direction, and the other with the person lying on their back (supine position) with gravity in the negative Y-direction. The displacement contours for the isotropic tongue with gravity in the Z-direction with the person in the standing position for the LMM UEL element are displayed in Figure 8.4 (displacement plot scaled to 1000 %). It should be noted that in all displacement contour plots, the values at only one node per element are rendered during post-processing.

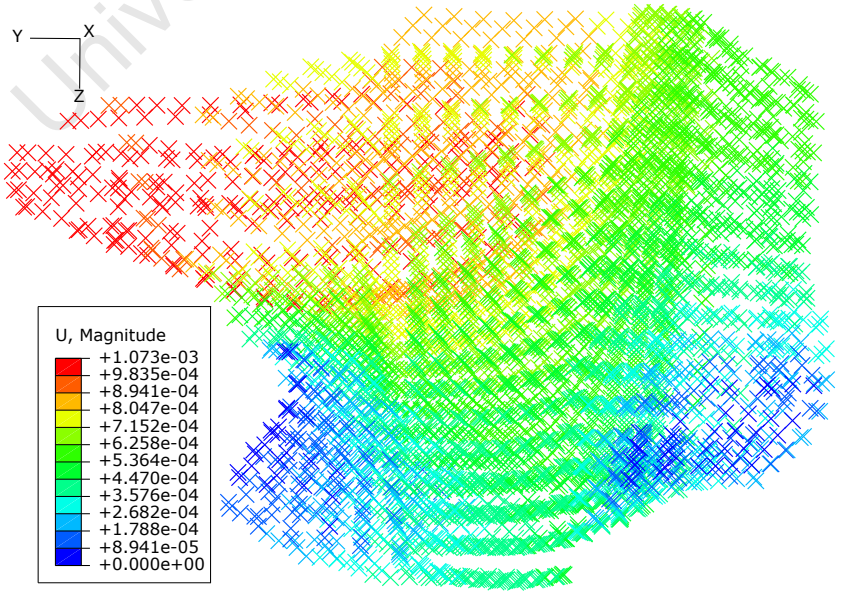

Figure 8.4: Isotropic tongue displacement contours for gravity in the Z-direction.

The displacement contours for the isotropic tongue with gravity in the negative Y-direction for the LMM UEL element type are displayed in Figure 8.5 (displacement plot scaled to 1000 %). This loading direction with the person in the supine position (on their back) is selected for muscle activation tests to follow.

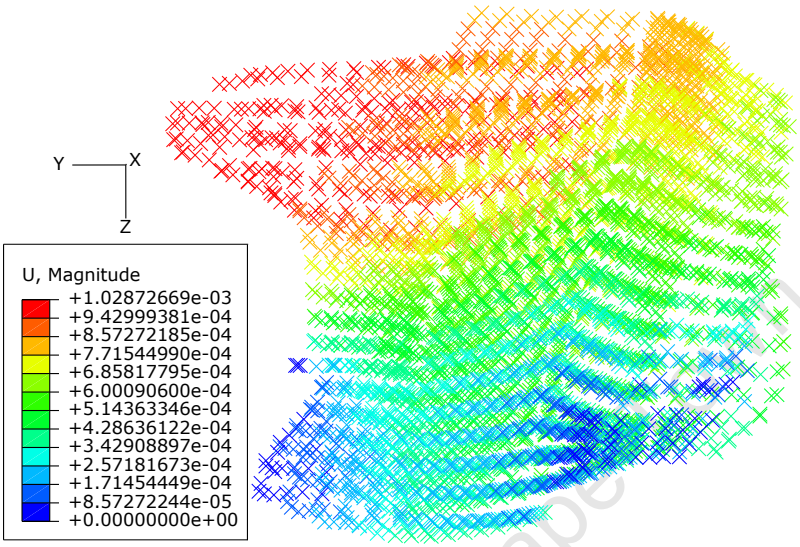

Figure 8.5: Isotropic tongue displacement contours for gravity in the negative Y-direction.

The displacement contours with all muscles being passive under gravitational loading in the negative Y-direction are shown in Figure 8.6 (displacement plot scaled to 1000 %). It should be noted that the tongue with passive fibres is only slightly stiffer than the isotropic case.

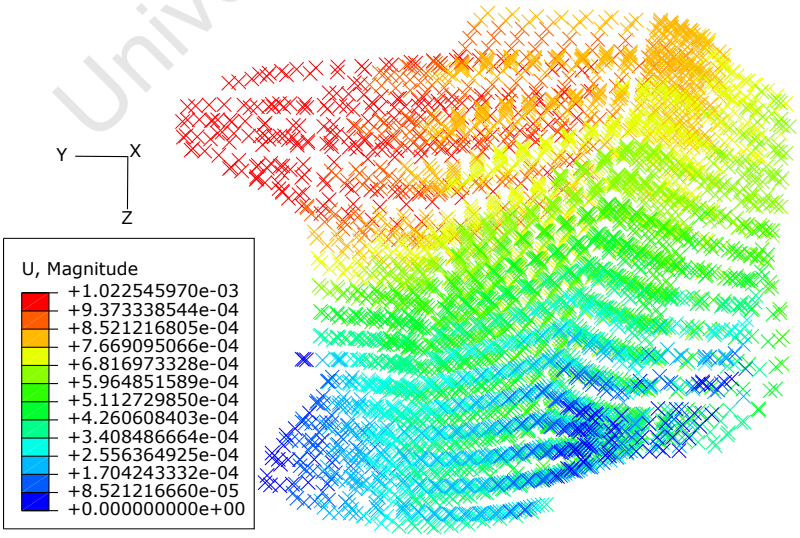

Figure 8.6: Passive tongue displacement contour for LMM UEL.

8.3 Active tongue muscles

The effects of individually activated tongue muscles without gravitational loading are examined here. All muscles besides the one being activated are set to be passive. The number of elements of the mesh containing fibres belonging to each muscle group was introduced in Table 4.1. The displacement contours for the results of each individually activated muscle are plotted at $t = 0.9\,s$, at the time increment nearest to the maximum muscle contraction which occurs at $t = 1\,s$. The maximum displacement magnitude results are summarized in Table 8.1, comparing the maximum displacement anywhere in the tongue for each muscle.

Table 8.1: Maximum displacement magnitude results for active tongue muscles.

muscle number	muscle name	$u_{\text{magnitude}}\ (mm)$
1	digastric	826×10^{-3}
2	genioglossus	845×10^{-3}
3	geniohyoid	950×10^{-3}
4	hyoglossus	884×10^{-3}
5	inferior longitudinal	1073×10^{-3}
6	mylohyoid	885×10^{-3}
7	superior longitudinal	1383×10^{-3}
8	transversalis	1913×10^{-3}
9	verticalis	1681×10^{-3}

The displacement of node 2315 in Figure 8.1 for each loading case is summarized in Table 8.2.

Table 8.2: Displacement results for node 2315 for active tongue muscles.

muscle number	active muscle	$u_x\ (mm)$	$u_y\ (mm)$	$u_z\ (mm)$	$u_{\text{magnitude}}\ (mm)$
1	DG	-3.636×10^{-3}	10.070×10^{-3}	-5.498×10^{-3}	12.035×10^{-3}
2	GG	16.200×10^{-3}	29.480×10^{-3}	-35.530×10^{-3}	48.991×10^{-3}
3	GH	1.945×10^{-3}	23.871×10^{-3}	-67.982×10^{-3}	72.078×10^{-3}
4	HG	-116.139×10^{-3}	81.402×10^{-3}	130.100×10^{-3}	192.459×10^{-3}
5	IL	48.909×10^{-3}	12.044×10^{-3}	-41.742×10^{-3}	65.419×10^{-3}
6	MH	-23.782×10^{-3}	-44.945×10^{-3}	22.958×10^{-3}	55.791×10^{-3}
7	SL	-195.280×10^{-3}	-148.830×10^{-3}	30.562×10^{-3}	247.420×10^{-3}
8	T	-144.310×10^{-3}	-804.180×10^{-3}	0.241×10^{-3}	817.030×10^{-3}
9	V	159.410×10^{-3}	941.950×10^{-3}	129.200×10^{-3}	964.040×10^{-3}
All	All active	-250.397×10^{-3}	121.992×10^{-3}	152.685×10^{-3}	317.637×10^{-3}
2+4+9	GG+HG+V	59.468×10^{-3}	1052.940×10^{-3}	223.771×10^{-3}	1078.090×10^{-3}

8.3.1 DG ACTIVE

The displacement contour for the active DG muscle is illustrated in Figure 8.7. Maximum displacement occurs near the base of the tongue in the DG muscle.

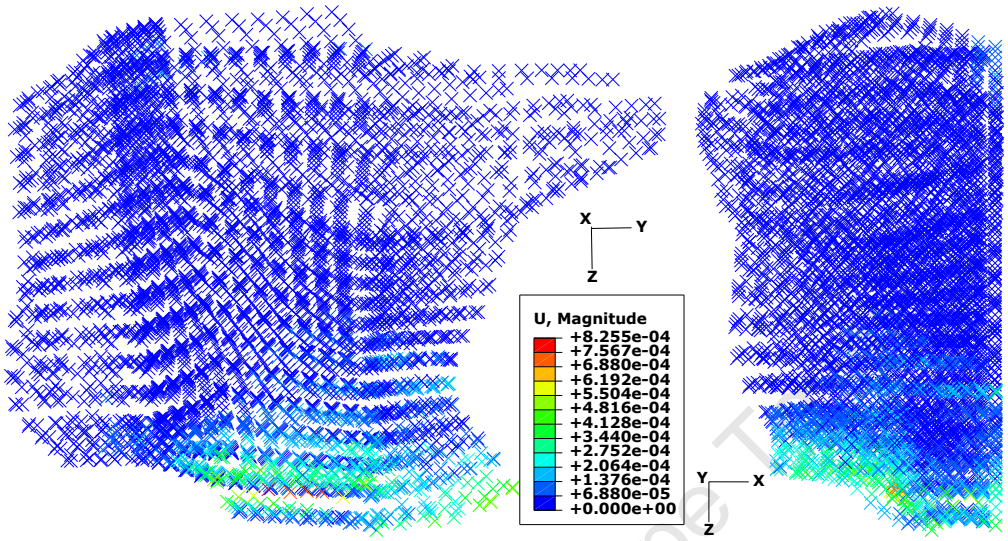

Figure 8.7: Tongue displacement contour for active DG muscle.

8.3.2 GG ACTIVE

The displacement contour for the active GG muscle is illustrated in Figure 8.8. Maximum displacement occurs near the mid-sagittal region of the tongue fanning out from front to back.

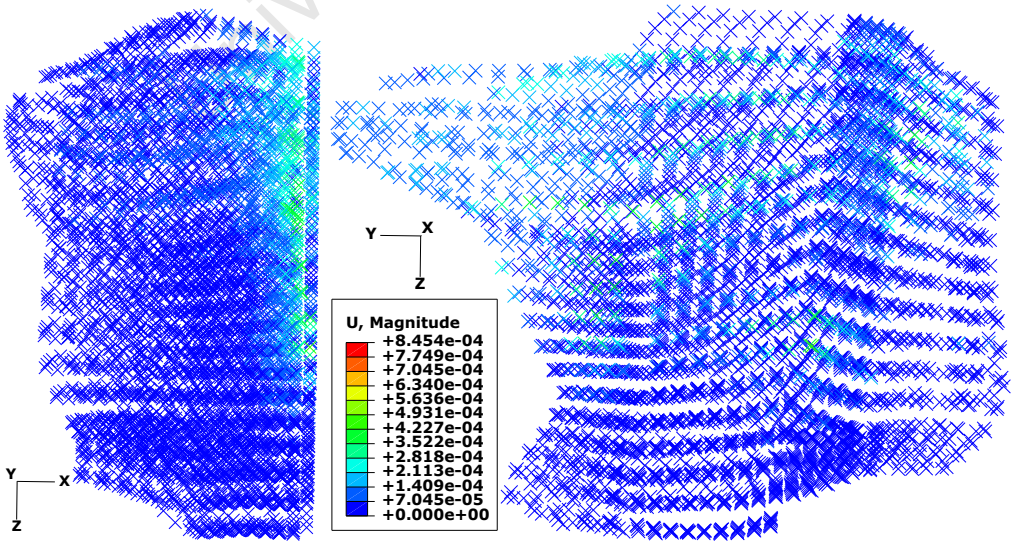

Figure 8.8: Tongue displacement contour for active GG muscle.

8.3.3 GH ACTIVE

The displacement contour for the active GH muscle is illustrated in Figure 8.9. Maximum displacement occurs mid-sagittally near the base of the tongue in the GH muscle.

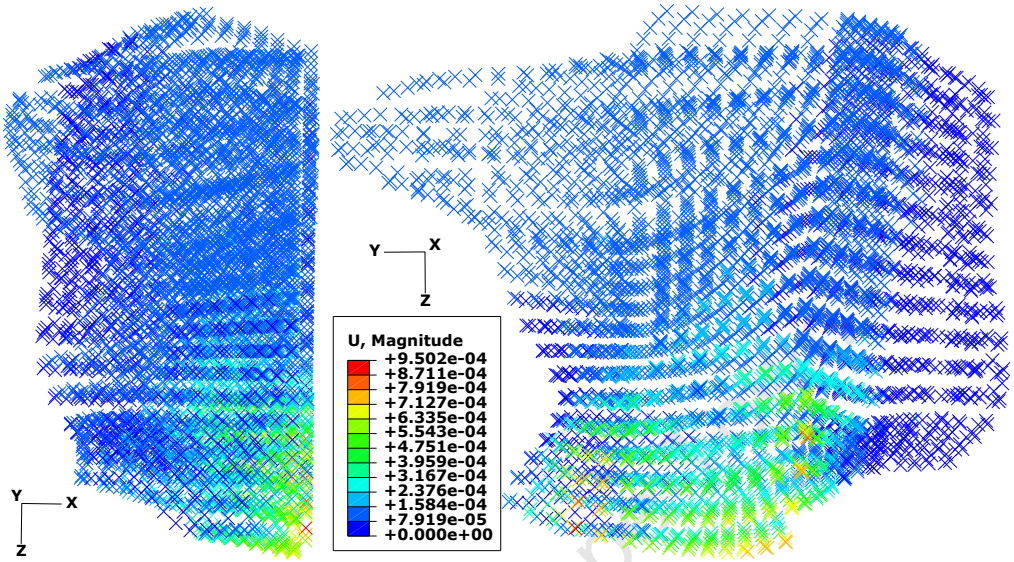

Figure 8.9: Tongue displacement contour for active GH muscle.

8.3.4 HG ACTIVE

The displacement contour for the active HG muscle is illustrated in Figure 8.10. Maximum displacement occurs near the back of the tongue in the HG muscle, pulling the top of the tongue downward and forward.

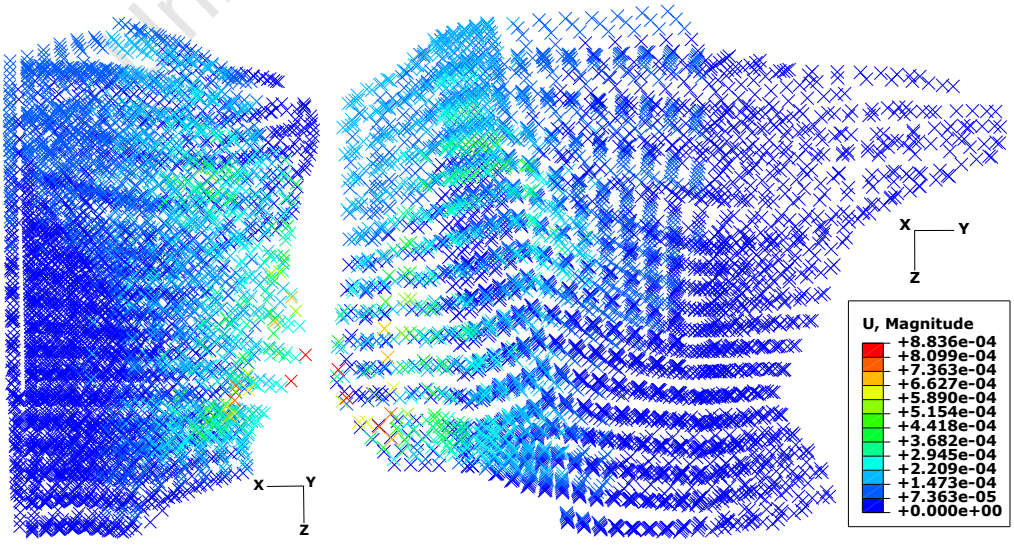

Figure 8.10: Tongue displacement contour for active HG muscle.

8.3.5 IL ACTIVE

The displacement contour for the active IL muscle is illustrated in Figure 8.11. Maximum displacement occurs under the tip and front outer portion of the tongue in the IL muscle.

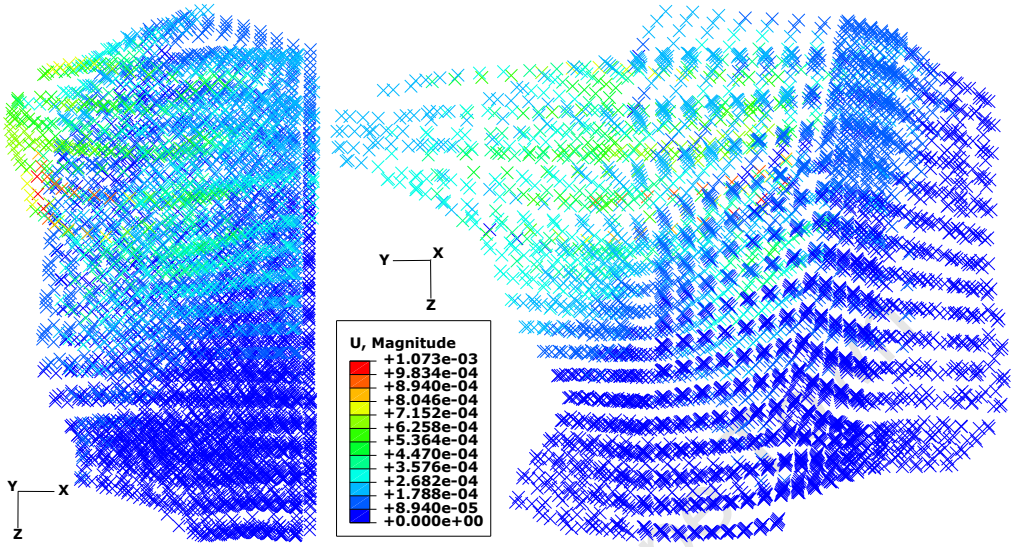

Figure 8.11: Tongue displacement contour for active IL muscle.

8.3.6 MH ACTIVE

The displacement contour for the active MH muscle is illustrated in Figure 8.12. The main region of displacement cradles the base of the tongue from side to side in the MH muscle.

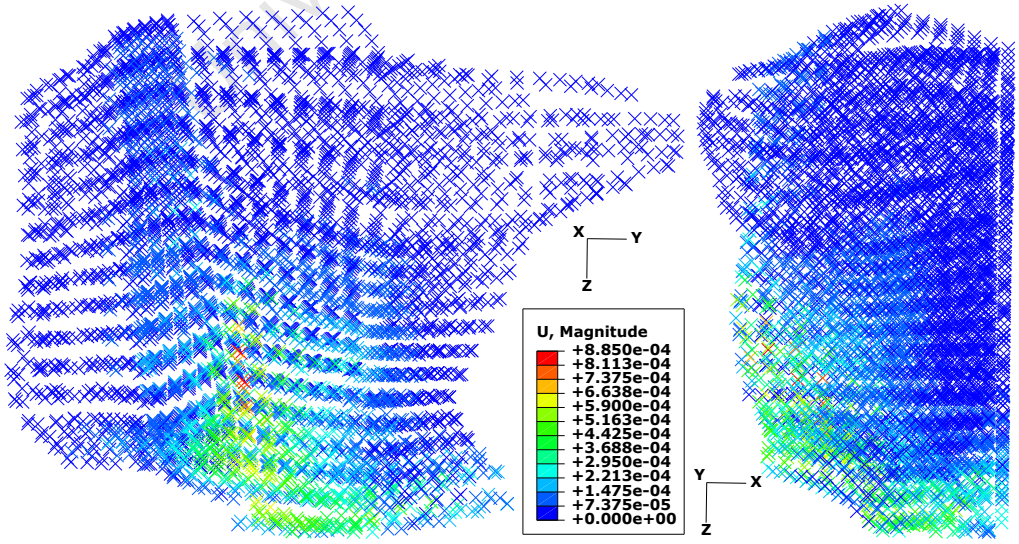

Figure 8.12: Tongue displacement contour for active MH muscle.

8.3.7 SL ACTIVE

The displacement contour for the active SL muscle is illustrated in Figure 8.13. Maximum displacement occurs at the tip of the tongue which is lifted up and towards the back of the mouth.

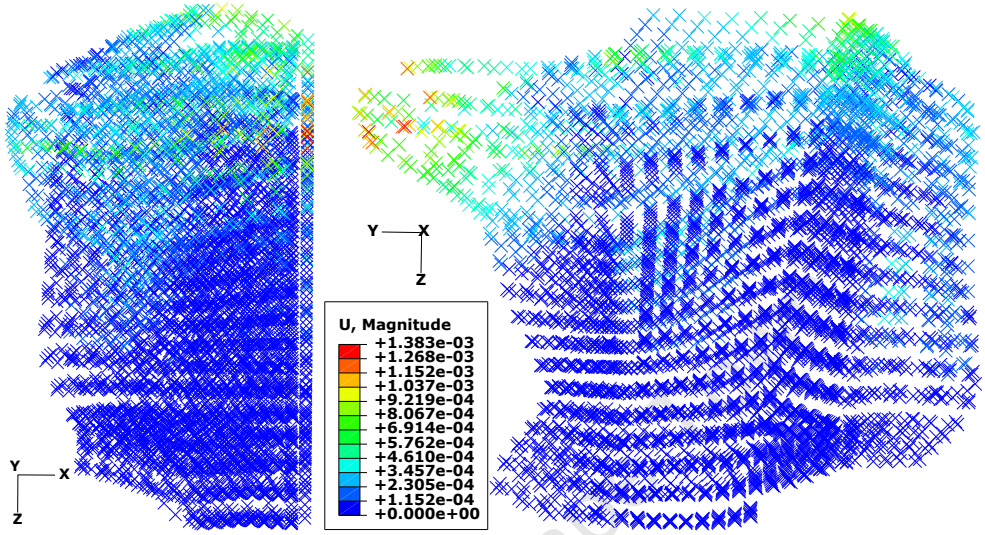

Figure 8.13: Tongue displacement contour for active SL muscle.

8.3.8 T ACTIVE

The displacement contour for the active transversalis muscle is illustrated in Figure 8.14. Maximum displacement occurs in the upper body of the tongue which is contracted in the sagittal plane. This sagittal contraction causes the upper body of the tongue to displace upwards and backwards.

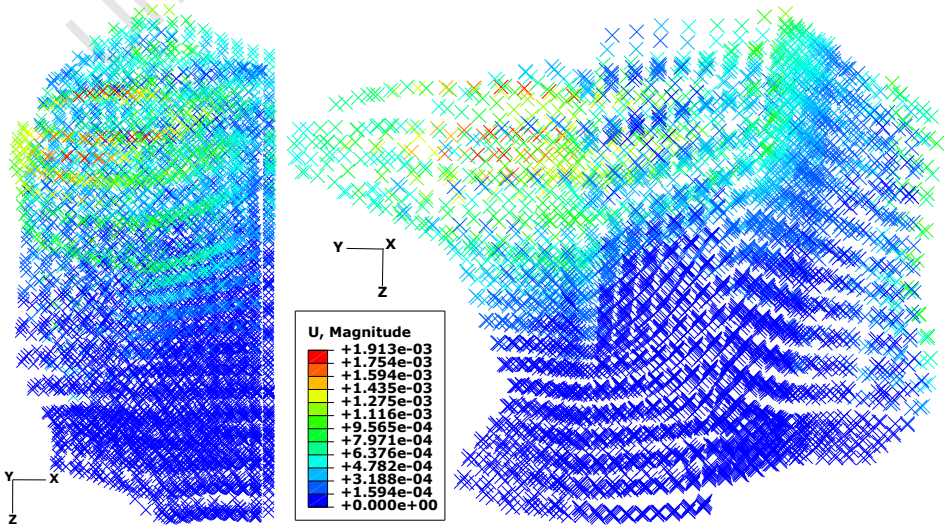

Figure 8.14: Tongue displacement contour for active T muscle.

8.3.9 V active

The displacement contour for the active verticalis muscle is illustrated in Figure 8.15. Maximum displacement occurs at the tip of the tongue but the back portion of the tongue is also drawn forward.

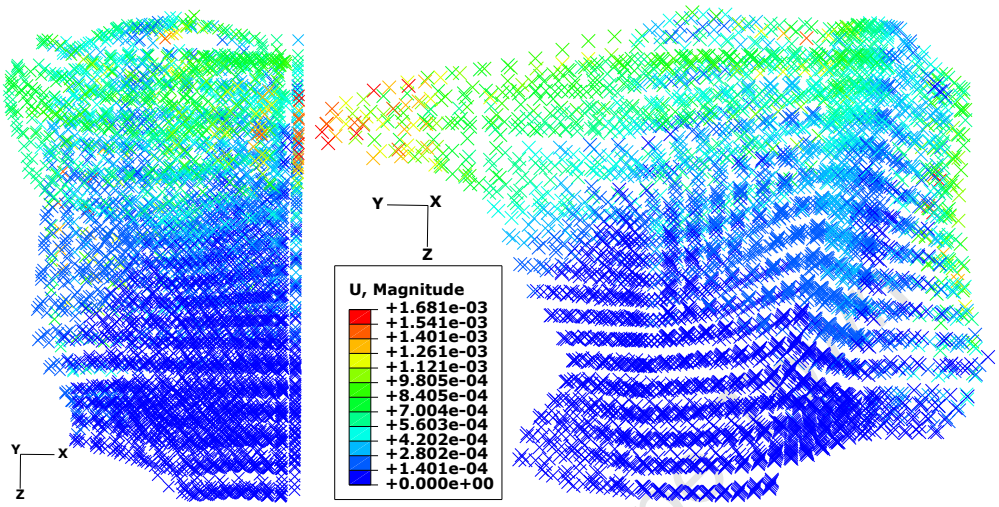

Figure 8.15: Tongue displacement contour for active V muscle.

8.3.10 All muscles active

The displacement contour for the case with all muscles activated simultaneously is illustrated in Figure 8.16. It appears that in this case, the maximum displacement occurs at the tip of the tongue.

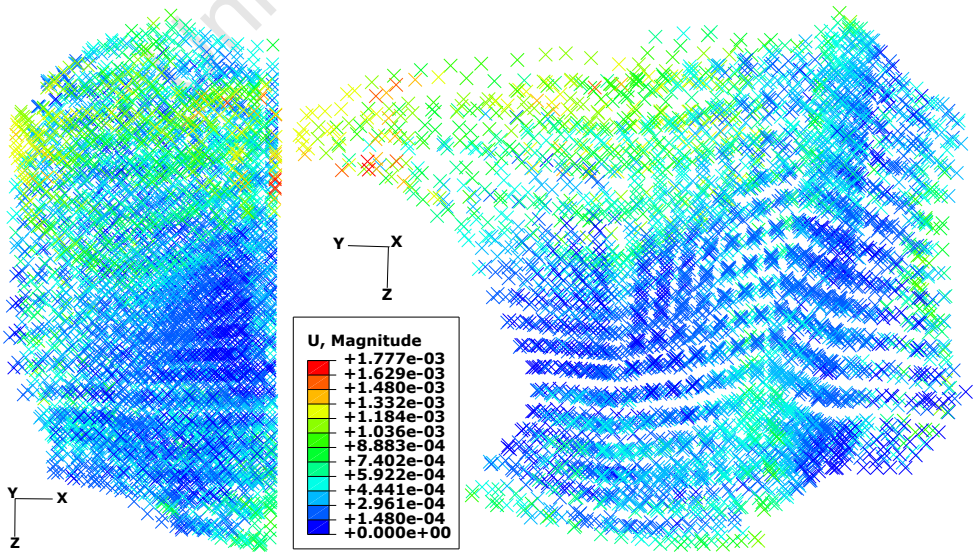

Figure 8.16: Tongue displacement contour for all active muscles.

8.3.11 Active GG, HG and V muscles

The displacement contour for active GG, HG and verticalis muscles is illustrated in Figure 8.17. Activating these muscles pulls the tip of the tongue as well as the back of the tongue forward.

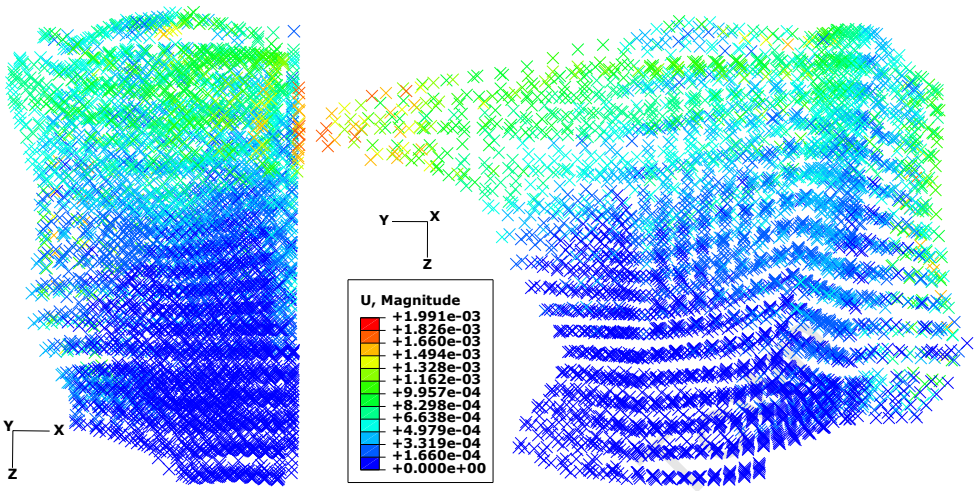

Figure 8.17: Tongue displacement contour for active GG, HG and V muscles.

8.4 Active tongue muscles under gravity

The effect of individual active tongue muscles under gravitational loading in the negative Y-direction are examined here. The displacement results are summarized in Table 8.3, where the maximum displacement magnitude anywhere in the tongue for each individually activated muscle is compared.

Table 8.3: Maximum displacement magnitude results for active tongue under gravity.

muscle number	muscle name	$u_{\text{magnitude}}$ (mm)
1	digastric	1222×10^{-3}
2	genioglossus	1373×10^{-3}
3	geniohyoid	989×10^{-3}
4	hyoglossus	1072×10^{-3}
5	inferior longitudinal	1980×10^{-3}
6	mylohyoid	1087×10^{-3}
7	superior longitudinal	2376×10^{-3}
8	transversalis	2022×10^{-3}
9	verticalis	1776×10^{-3}
-	isotropic	1028×10^{-3}
All	All passive	1022×10^{-3}

The displacement of node 2315 in Figure 8.1 for each load case is summarised in Table 8.4.

Table 8.4: Displacement results for node 2315 for active tongue muscles under gravity.

muscle number	active muscle	u_x (mm)	u_y (mm)	u_z (mm)	$u_{\text{magnitude}}$ (mm)
All	All passive	-13.69 $\times 10^{-3}$	-669.91 $\times 10^{-3}$	19.09 $\times 10^{-3}$	670.33 $\times 10^{-3}$
1	DG	-17.83 $\times 10^{-3}$	-663.70 $\times 10^{-3}$	14.09 $\times 10^{-3}$	664.09 $\times 10^{-3}$
2	GG	2.01 $\times 10^{-3}$	-644.18 $\times 10^{-3}$	-15.94 $\times 10^{-3}$	644.38 $\times 10^{-3}$
3	GH	-12.24 $\times 10^{-3}$	-649.90 $\times 10^{-3}$	-48.39 $\times 10^{-3}$	651.81 $\times 10^{-3}$
4	HG	-130.32 $\times 10^{-3}$	-592.36 $\times 10^{-3}$	149.69 $\times 10^{-3}$	624.73 $\times 10^{-3}$
5	IL	34.72 $\times 10^{-3}$	-661.72 $\times 10^{-3}$	-22.15 $\times 10^{-3}$	663.00 $\times 10^{-3}$
6	MH	-37.97 $\times 10^{-3}$	-718.71 $\times 10^{-3}$	42.55 $\times 10^{-3}$	720.97 $\times 10^{-3}$
7	SL	-209.47 $\times 10^{-3}$	-822.59 $\times 10^{-3}$	50.15 $\times 10^{-3}$	850.32 $\times 10^{-3}$
8	T	-158.50 $\times 10^{-3}$	-1477.94 $\times 10^{-3}$	22.00 $\times 10^{-3}$	1486.58 $\times 10^{-3}$
9	V	145.22 $\times 10^{-3}$	268.18 $\times 10^{-3}$	148.78 $\times 10^{-3}$	339.34 $\times 10^{-3}$
All	All active	-264.59 $\times 10^{-3}$	-551.77 $\times 10^{-3}$	172.27 $\times 10^{-3}$	635.72 $\times 10^{-3}$
2+4+9	GG+HG+V	45.28 $\times 10^{-3}$	379.17 $\times 10^{-3}$	243.36 $\times 10^{-3}$	452.82 $\times 10^{-3}$

8.4.1 DG ACTIVE

The displacement contour for the active DG muscle under gravitational loading is illustrated in Figure 8.18. Maximum displacement occurs near the base of the tongue in the DG muscle, and also in the main body of the tongue due to gravity which is largely unaffected by the muscle contraction.

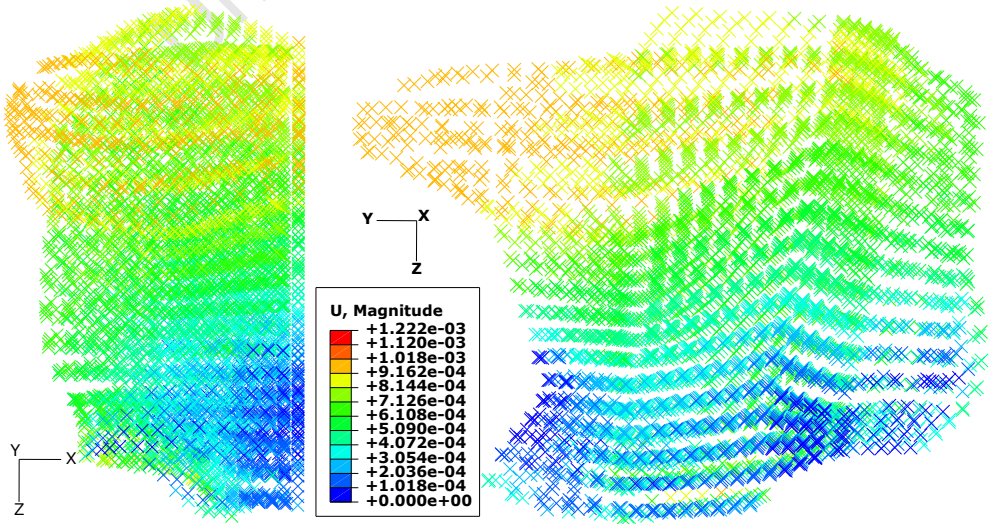

Figure 8.18: Tongue displacement contour for active DG muscle with gravity.

8.4.2 GG ACTIVE

The displacement contour for the active GG muscle under gravitational loading is illustrated in Figure 8.19. Maximum displacement occurs near the mid-sagittal region of the tongue, and counteracts the effect of gravity.

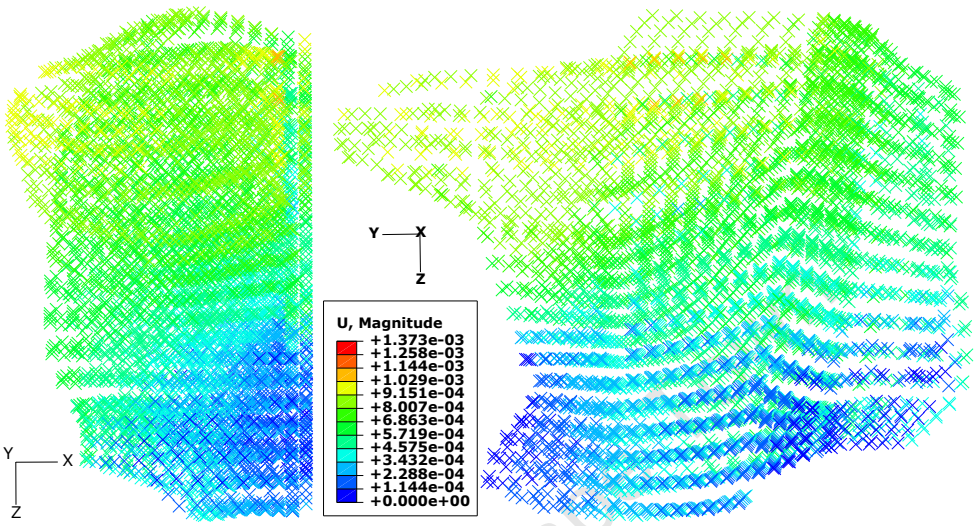

Figure 8.19: Tongue displacement contour for active GG muscle with gravity.

8.4.3 GH ACTIVE

The displacement contour for the active GH muscle under gravitational loading is illustrated in Figure 8.20. Maximum displacement occurs mid-sagittally near the base of the tongue due to GH muscle contraction, but also at the top portion of the tongue due to gravity.

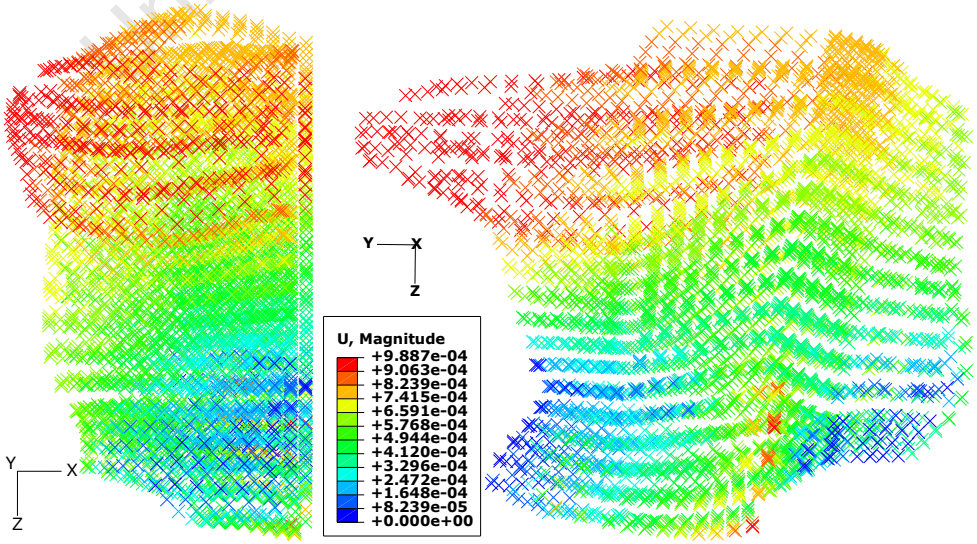

Figure 8.20: Tongue displacement contour for active GH muscle with gravity.

8.4.4 HG ACTIVE

The displacement contour for the active HG muscle under gravitational loading is illustrated in Figure 8.21. Maximum displacement occurs due to gravity but the HG muscle still pulls the top posterior part of the tongue downwards and forwards.

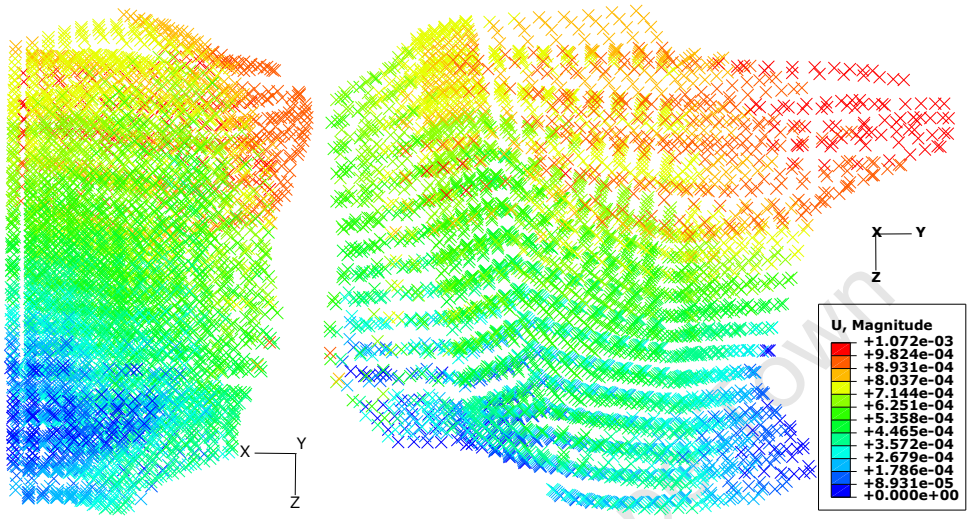

Figure 8.21: Tongue displacement contour for active HG muscle with gravity.

8.4.5 IL ACTIVE

The displacement contour for the active IL muscle under gravitational loading is illustrated in Figure 8.22. Maximum displacement occurs under the tip and front outer portion of the tongue in the IL muscle combining with gravity which pulls the body of the tongue backwards.

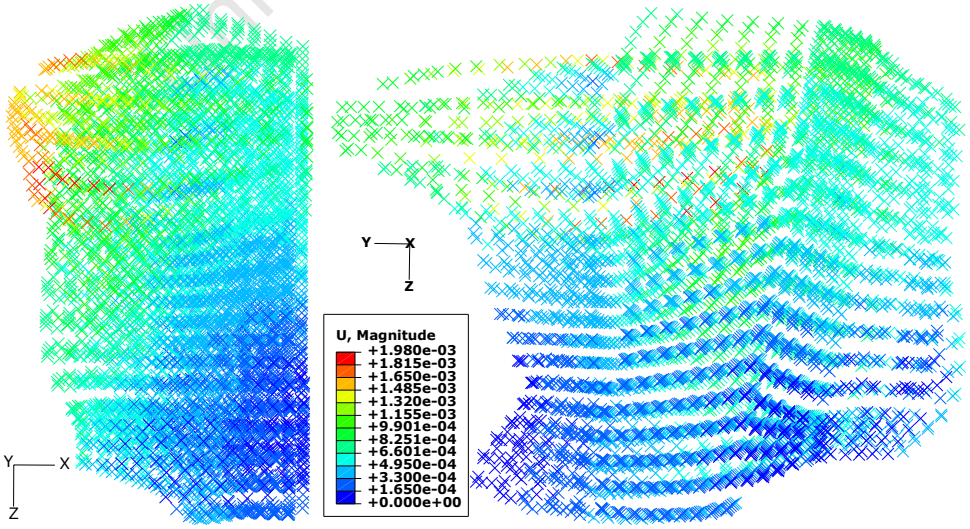

Figure 8.22: Tongue displacement contour for active IL muscle with gravity.

8.4.6 MH active

The displacement contour for the active MH muscle under gravitational loading is illustrated in Figure 8.23. Displacement due to gravity dominates, but a region of displacement cradling the base of the tongue from side to side in the MH muscle is also significant.

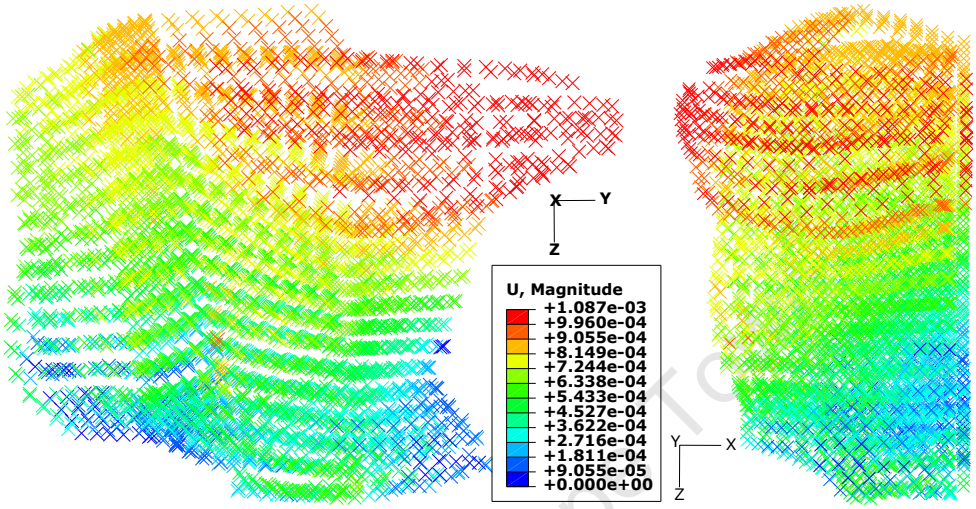

Figure 8.23: Tongue displacement contour for active MH muscle with gravity.

8.4.7 SL active

The displacement contour for the active SL muscle under gravitational loading is illustrated in Figure 8.24. Maximum displacement occurs at the tip of the tongue which is lifted up and towards the back of the mouth combining with gravity pulling the body of the tongue even further back.

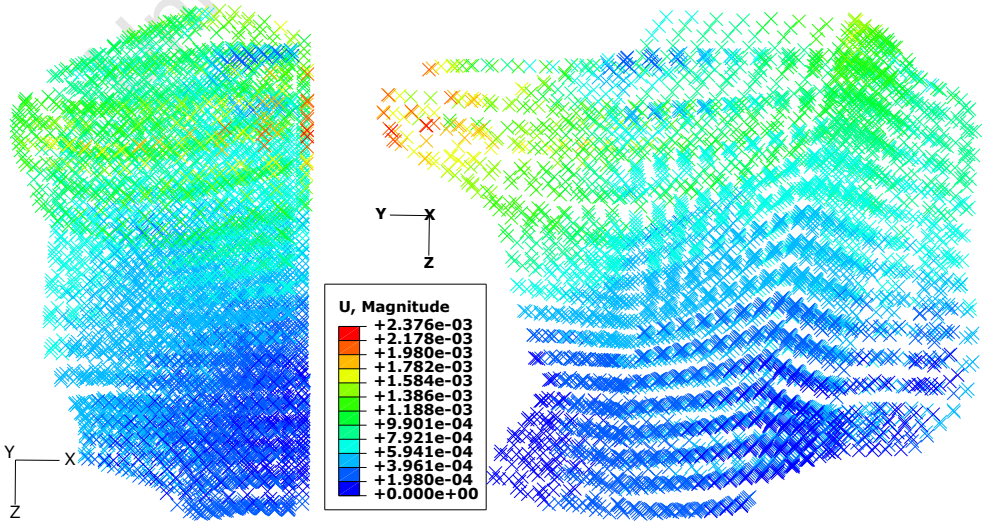

Figure 8.24: Tongue displacement contour for active SL muscle with gravity.

8.4.8 T ACTIVE

The displacement contour for the active transversalis muscle under gravitational loading is illustrated in Figure 8.25. Maximum displacement occurs in the upper body of the tongue which is contracted in the sagittal plane. This sagittal contraction causes the upper body of the tongue to displace upwards and backwards combining with gravity pulling the body of the tongue even further back.

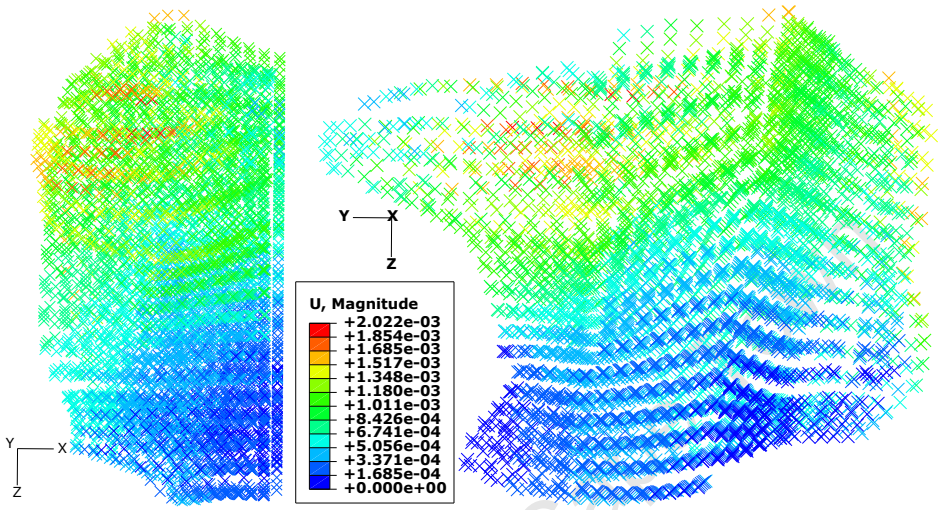

Figure 8.25: Tongue displacement contour for active T muscle with gravity.

8.4.9 V ACTIVE

The displacement contour for the active verticalis muscle under gravitational loading is illustrated in Figure 8.26. Maximum displacement occurs at the tip of the tongue but the back portion of the tongue is also drawn forward, counteracting the effect of gravity.

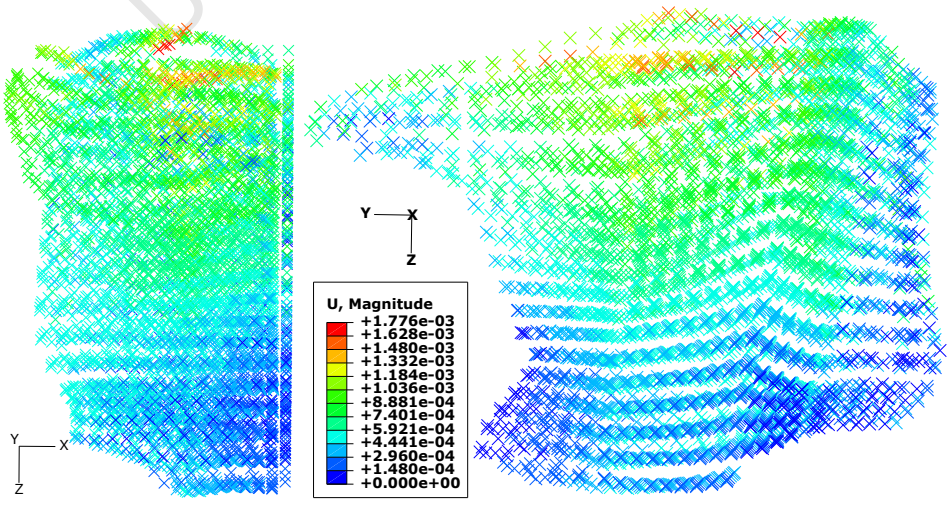

Figure 8.26: Tongue displacement contour for active V muscle with gravity.

8.4.10 All muscles active

The displacement contour for the case with all muscles active simultaneously under gravitational loading is illustrated in Figure 8.27. It appears in this case that the maximum displacement occurs at the outer top portion of the tongue, but not at the tip, nor the back of the tongue.

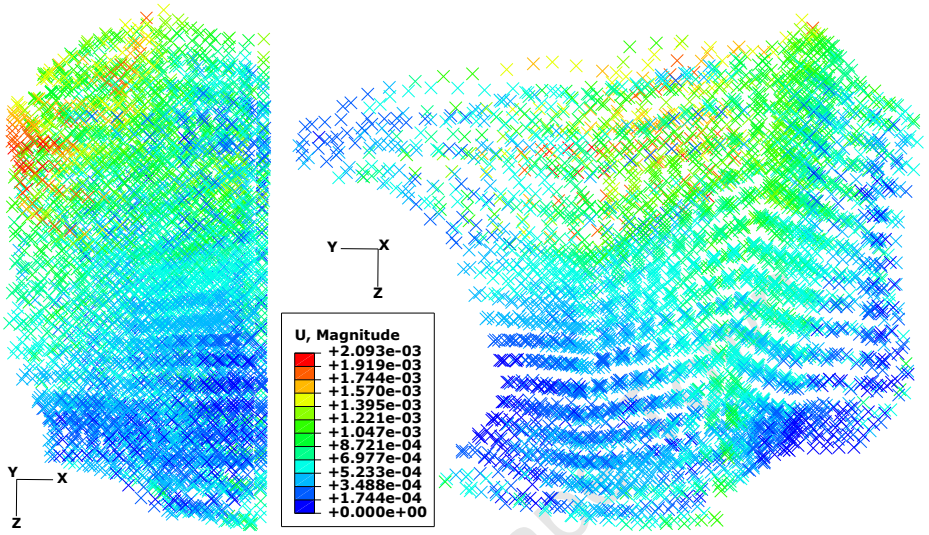

Figure 8.27: Tongue displacement contour for all active muscles.

8.4.11 Active GG, HG and V muscles

The displacement contour for the case with the GG, HG and verticalis muscles active simultaneously under gravitational loading is illustrated in Figure 8.28. Activating this set of muscles pulls the tip of the tongue, as well as the back of the tongue forward.

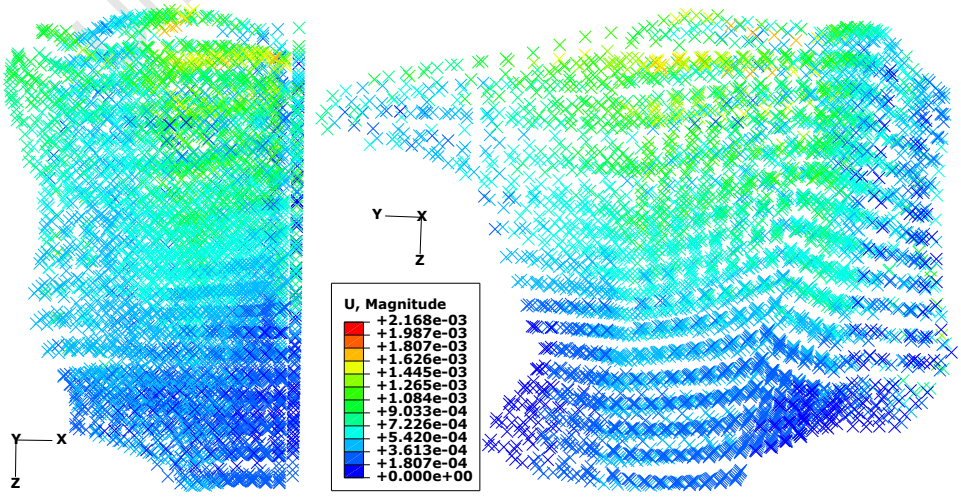

Figure 8.28: Tongue displacement contour for active GG, HG and V muscles.

8.5 Discussion

A finite element model on the passive and active behaviour of the human tongue has been presented and analysed with the Abaqus/Standard solver. The geometry of the human tongue is based on the assumption of symmetry. This is a reasonable assumption taking into account the direction of loading and the anatomy of the tongue. The high level of detail of the geometry extracted was deemed to be accurate enough for the purposes of this work. The voxel size of $\frac{1}{3} \times \frac{1}{3} \times \frac{1}{3}$ mm means that features as small as this could be captured.

This highly detailed geometry was used to generate a mesh of 4800 elements. This mesh size seemed reasonable for the size of the domain used. The entire body of the tongue could fit into a space of roughly $100 \times 100 \times 100$ mm. The mesh could have been refined, but this may have resulted in longer simulation times for a possibly small increase in accuracy.

The muscle fibre data of each muscle group within the tongue was successfully combined with the mesh. Activating specific muscle groups individually or simultaneously produces a wide range of results, as can be seen in this chapter. The main objective was to examine how activation of specific muscle groups, or combinations thereof, under gravitational loading influence the constriction of the human upper airway and hence OSA, by way of the tongue.

8.5.1 Passive and active contributions

In all the simulations presented using gravitational loading, the gravitational load was applied by ramping up from zero to its maximum value over a period of 1 second, starting at the beginning of the simulation, and maintaining this force until the end of the simulation. Once the gravitational load reached its peak value at $t = 1$ s, specific muscles were activated for a period of 1 second, and deactivated at $t = 2$ s (except in the passive and isotropic cases, where no muscles are activated).

The Y-displacement history of node 2315 for the case with all muscles being passive under gravitational loading is shown in Figure 8.29(a), and this corresponds to the displacement contour in Figure 8.6. The Y-displacement history of node 2315 for GG, HG and V muscle being activated simultaneously under gravitational loading is shown in Figure 8.29(b), and this corresponds to the displacement contour in Figure 8.28.

From these two figures, the difference between the active and passive behaviour is clear. The contribution of the activation load to the displacement behaviour can be superimposed on the contribution of the gravitational load in the passive case. In the passive case, only the gravitational load applies, and this results in a displacement in the negative Y-direction. In the active case, the three muscles being activated all contribute to pulling the body of the tongue towards the front of the mouth,

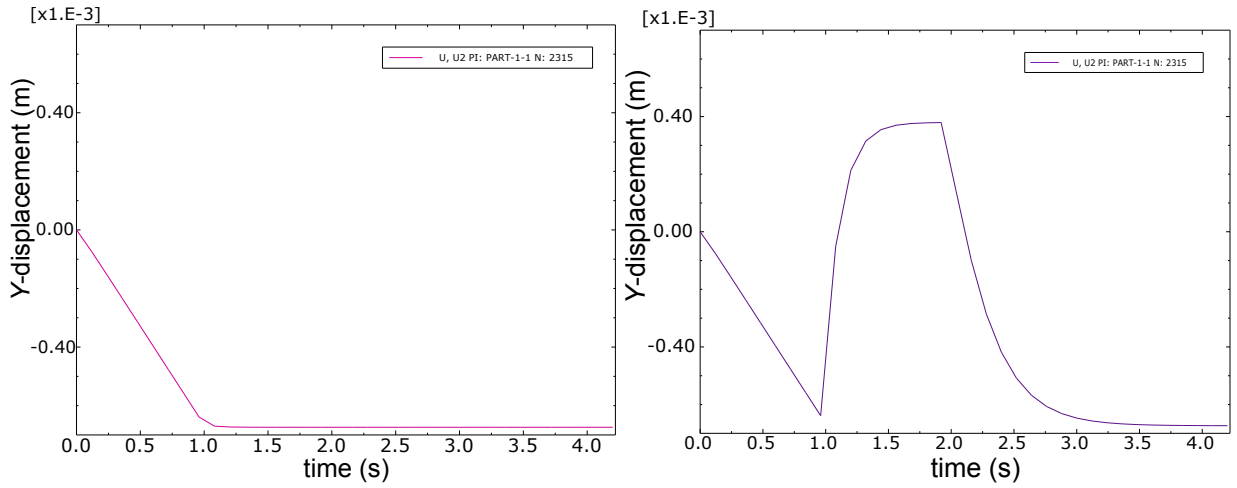

(a) Y-displacement history for node 2315 for all muscles passive under gravitational loading.

(b) Y-displacement history for node 2315 for active GG, HG and V muscles under gravitational loading.

Figure 8.29: Y-displacement history for node 2315 for passive and active muscles under gravity.

resulting in a positive displacement in the Y-direction for the duration of muscle activation. When the muscle is deactivated in this case, the tongue eventually returns to the position it held in the passive case (see Figure 8.29(b)).

The stress and strain histories for the passive case and for the case with the GG, HG and V muscles being active are displayed in Figure 8.30(a) and Figure 8.30(b), respectively. The magnitude of stress increases when the muscles are activated. The magnitude of strain decreases when the muscles are activated. This model in the passive and active cases shows similar behaviour to the model presented in Martins et. al. [88], and the results correlate well.

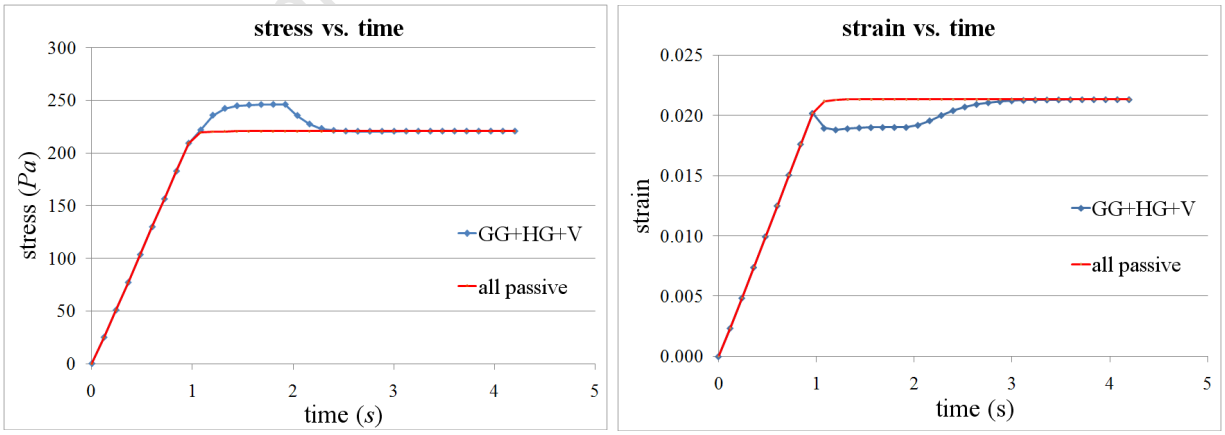

(a) Stress history for passive and active muscles.

(b) Strain history for passive and active muscles.

Figure 8.30: Stress and strain histories for node 2315 for passive and active muscles under gravitational loading.

8.5.2 Muscle activation without gravitational loading

From the results for the active tongue muscles without gravitational loading displayed in Tables 4.1 and 8.1, and the displacement contours in Figures 8.7 to 8.15, it can be seen that some muscles move the tongue away from the back of the mouth, while others move them towards the back of the mouth. Those that move the tongue away from the back of the mouth when activated, reduce the potential for an OSA event to occur, and show a positive displacement in the Y-direction. The muscle which moves the tongue furthest forward, is the verticalis muscle, as it has the largest positive displacement in the Y-direction. From highest to lowest positive displacement in the Y-direction, the HG, GG, GH, IL, and DG muscles also move the tongue forward, but less so than the verticalis muscle. The muscle which pulls the tongue toward the back of the mouth the most, is the transversalis muscle. The SL and MH muscles also pull the tongue backward, the SL more so than the MH.

Some of these muscles were activated simultaneously, and the resulting displacement shown as the last entry in Table 8.1. For this case, the GG, HG and V muscles were selected and activated. The combined activation moves the tongue even further forward than if they were individually activated. The displacement history of node 2315 in the Y-direction for the case with GG, HG and V muscles being activated simultaneously is shown in Figure 8.31(b), and this corresponds to the displacement contour presented in Figure 8.17.

Another test was done with all muscles being activated simultaneously. This result is shown as the second last entry in Table 8.1. The displacement history of node 2315 in the Y-direction for the case with all muscles being active is shown in Figure 8.31(a), and this corresponds to the displacement contour presented in Figure 8.16.

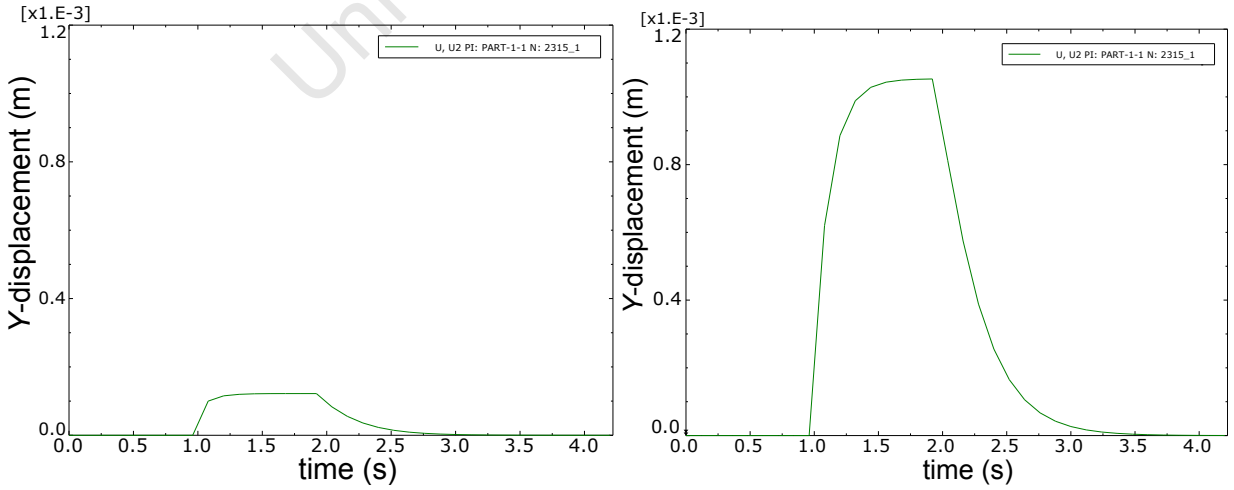

(a) Y-displacement history for node 2315 for all active muscles active

(b) Y-displacement history for node 2315 for active GG, HG and V muscles

Figure 8.31: Y-displacement history for node 2315 for different active muscles.

In these figures, it can be clearly seen that activation of all muscles simultaneously has a mixed effect on results, leads to a smaller positive displacement in the Y-direction, and hence is not as effective as activating selected muscles as in the case with GG, HG and V activation.

The stress histories for the case with all muscles being active is shown together with the case with the GG, HG and V muscles being active in Figure 8.32(a). The stress history for the case with the GG, HG and V muscles being activated is shown alone in Figure 8.32(b) (Note: change of scale).

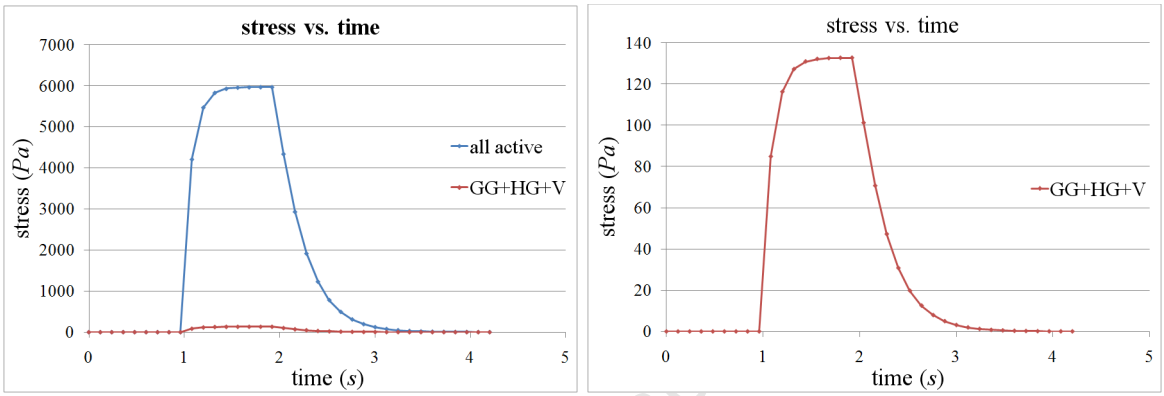

(a) Stress history for all active muscles and for active GG, HG and V muscles.

(b) Stress history for active GG, HG and V muscles.

Figure 8.32: Stress histories for node 2315 for all active muscles, and for active GG, HG and V.

The strain histories for all muscles being active, and for the case with the GG, HG and V muscles being active are displayed in Figure 8.33(a). The strain history for the case with the GG, HG and V muscles being activated is shown on its own in Figure 8.33(b) (Note: change of scale). Activation of all muscles simultaneously leads to stress and strain values higher than those obtained by only activating the GG, HG and V muscles.

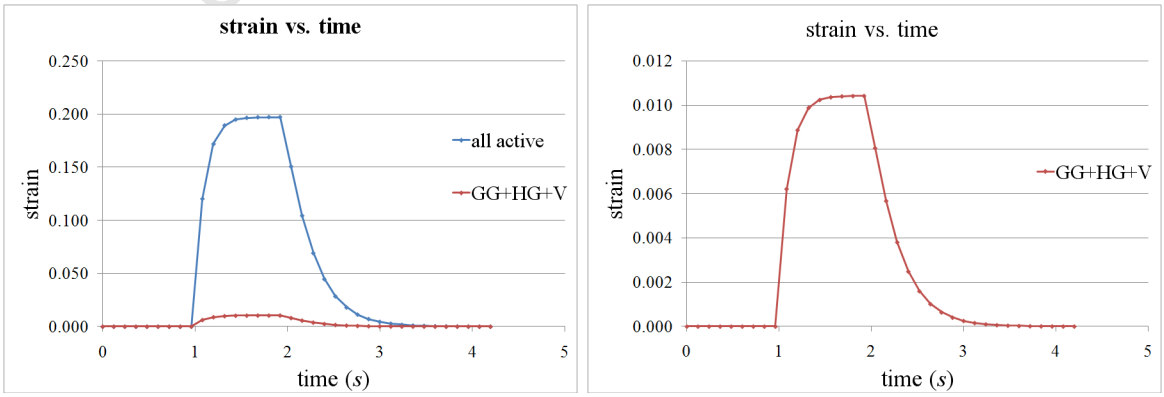

(a) Strain history for all active muscles and for active GG, HG and V muscles.

(b) Strain history for active GG, HG and V muscles.

Figure 8.33: Strain histories for node 2315 for all active muscles, and for active GG, HG and V.

8.5.3 Muscle activation with gravitational loading

The results for the active tongue muscles under gravitational loading is displayed in Tables 8.3 and 8.4, and in the displacement contours in Figures 8.18(a) to 8.26(a). In these simulation, the tongue was first loaded with gravitational loading, ramped up from zero to maximum value at $t = 1\ s$. Once the tongue is fully loaded, specific muscles, or combinations thereof, are activated. It was found that only the verticalis muscle had a positive displacement in the Y-direction. The DG, GH, GG, HG and the IL muscles also reduce the negative displacement caused by the gravitational load, but are not powerful enough to cause a positive displacement in the Y-direction when combined with the gravitational load. The T, SL and MH muscles combine with the force of gravity to pull the tongue further back.

A test was done combining the activation of the GG, HG and V muscles under gravitational loading. The Y-displacement history of node 2315 for the case with GG, HG and V muscle being activated simultaneously under gravitational loading is shown in Figure 8.34(b), and this corresponds to the displacement contour in Figure 8.28.

Another test with all muscles being active under gravitational loading was also run. The Y-displacement history of node 2315 for the case with all muscles being active under gravitational loading is shown in Figure 8.34(a), and this corresponds to the displacement contour in Figure 8.27. The muscle behaviour in the cases with gravitational loading was found to be similar as the cases without gravitational loading, i.e. the same muscles had similar effects either with or without gravitational loading.

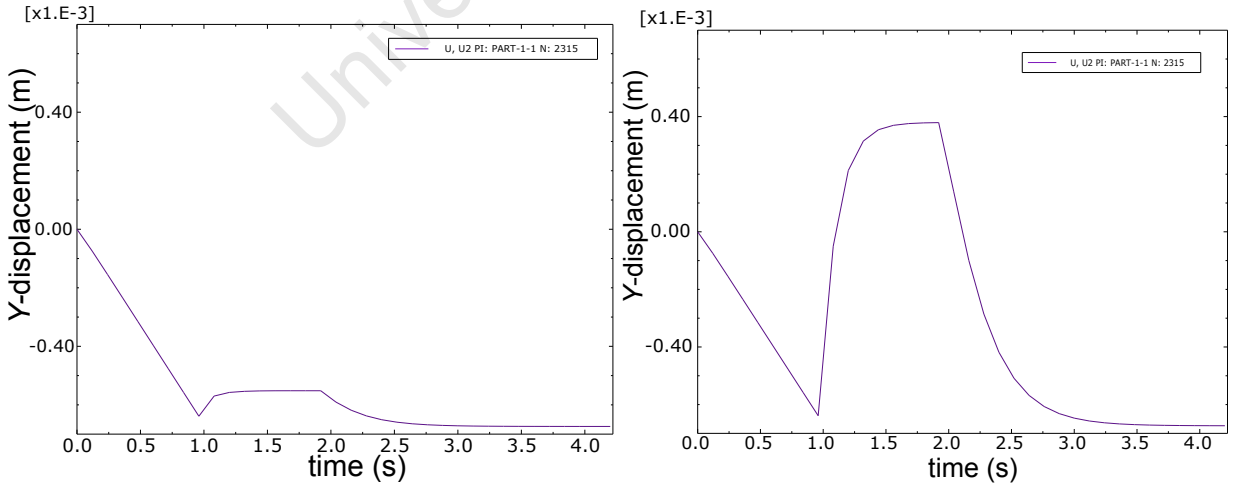

(a) Y-displacement history for node 2315 for all muscles active under gravitational loading

(b) Y-displacement history for node 2315 for active GG, HG and V muscles under gravitational loading

Figure 8.34: $Y-$displacement history for node 2315 for different active muscles under gravitational loading.

The effect of activating the GG, HG and V muscles on displacement, rather than all of the muscles simultaneously, can be seen in Figure 8.34. Negative displacement values in the Y-direction indicate a movement towards the back of the mouth, and positive displacement values away from the back of the mouth.

For the case with all muscles being activated simultaneously, the maximum value of displacement in the Y-direction after application of the gravitational load is -551.77×10^{-3} mm, whereas in the case with only the GG, HG and V being activated, the maximum value of displacement in the Y-direction after application of the gravitational load is $+379.17 \times 10^{-3}$ mm. By activating only a selected group of muscles, the gravitational load can be overcome, but activating all the muscles simultaneously leads to a much smaller effect.

The stress histories for all muscles being activated under gravitational loading is shown together with the case with the GG, HG and V muscles being activated under gravitational loading in Figure 8.35(a). The stress history for the case with the GG, HG and V muscles being activated under gravitational loading is shown on its own in Figure 8.35(b) (Note: change of scale). It can be seen from these figures that there is a larger stress in the tongue in the case where all muscles are active compared to the case with only the GG, HG and V muscles being active.

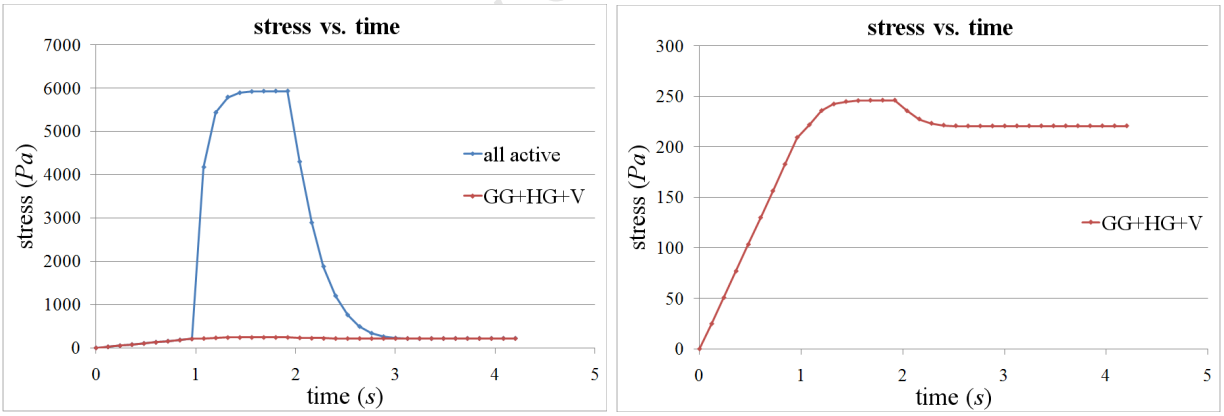

(a) Stress history for all active muscles and for active GG, HG and V muscles.

(b) Stress history for active GG, HG and V muscles.

Figure 8.35: Stress histories for node 2315 for all active muscles, and for active GG, HG and V muscles under gravitational loading.

The strain histories for all muscles being activated under gravitational loading is shown together with the case with the GG, HG and V muscles being activated under gravitational loading in Figure 8.36(a). The strain history for the case with the GG, HG and V muscles being activated under gravitational loading is shown on its own in Figure 8.36(b) (Note: change of scale). As with the

stress, it can be seen from these figures that there is a larger strain in the tongue in the case where all muscles are active compared to the case with only the GG, HG and V muscles being active.

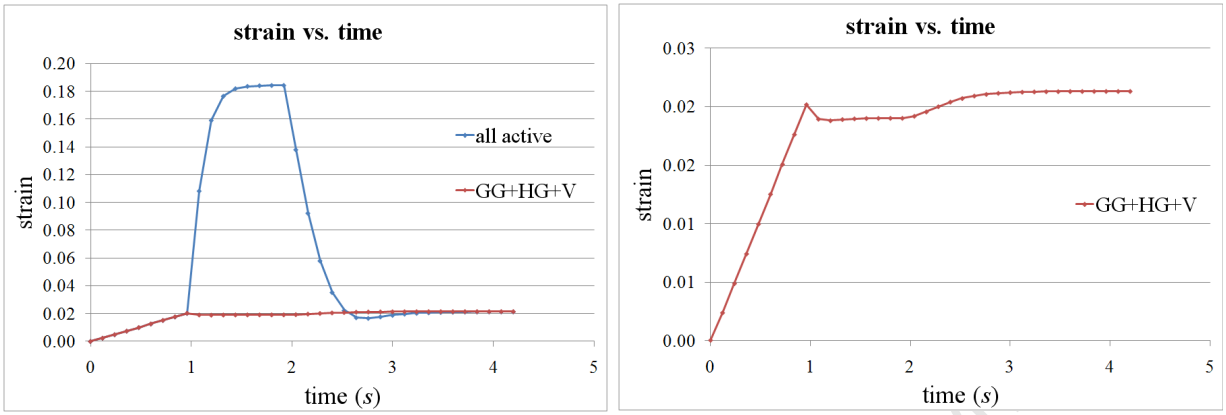

(a) Strain history for all active muscles and for active GG, HG and V muscles.

(b) Strain history for active GG, HG and V muscles.

Figure 8.36: Strain histories for node 2315 for all active muscles, and for active GG, HG and V muscles under gravitational loading.

In the case with all muscles activated, specific muscles counteract each other's effects, thus the resultant displacement is smaller, but the stresses and strains experienced are higher.

8.5.4 How do the simulation results relate to OSA?

The full finite element model, with defined muscle groups and muscle fibre orientations taken into account, has been developed. As mentioned previously, the focus of this work was to examine the behaviour of various muscles fibre groups of the tongue under gravitational loading, simulating some of the conditions in an OSA event. With this model, we were able to simulate the behaviour of the tongue with each muscle group individually activated and also with combinations of active muscle groups. We were also able to examine how different muscles contribute or counteract the OSA event when they are activated. These simulations allow insights into muscle behaviour which cannot be easily gained through physical testing. We have observed that activation of specific muscle groups of the tongue simultaneously leads to a reduction of airway constriction in this simulated OSA case. These are, in decreasing effect, the V, HG, GG, GH, IL, and DG muscle groups. It has also been noted that the activation parameter T_0 affects stiffness passively, but also more importantly, it affects the magnitude of the activation. This T_0 parameter affects the muscle model similarly to muscle tone in the tongue, which is also a contributing factor in OSA.

9 Concluding Remarks and Recommendations

"I hope that posterity will judge me kindly, not only as to the things which I have explained, but also to those which I have intentionally omitted so as to leave to others the pleasure of discovery." - Rene Descartes

The purpose of this project was to develop a realistic model able to simulate the movement of the tongue under internal loads, such as muscle activation, and external loads such as gravity and surface pressure. This linearized muscle model was a suitable step in the development and analysis of the model of the tongue. The muscle model is based on the works of Humphrey [62], Hill [53], and the recent work of Martins et. al. [88]. The results for the isometric and isotonic muscle activation tests are compared to those results found in the work of Martins et. al. [88].

Due to a limited timeframe, only a limited amount of research into the matter of muscle modelling can be done. With more time, a more realistic model can be developed. The work presented in this thesis is a necessary step to understanding muscle behaviour and its role in OSAS.

9.1 Full HUA modelling

The geometrical features of the human tongue were successfully obtained from the VHP dataset. This model was a necessary step in the development of a fully functional human upper airway model. Solid models of similar intricacy of other anatomical structures in the HUA will have to be formed. These include the soft palate, nasopharynx, epiglottis and any other soft tissues present, and also taking into account the hard tissues present.

9.2 Validation tests

The results were validated at relevant steps in development. Isotropic uniaxial testing, Cook's membrane test, passive fibre directionality testing, active fibre testing and body force testing were all done on varying mesh sizes. The results were found to correlate well for all tests. The isotropic tests were compared to standard element types available in Abaqus, deal.II, and relevant literature [104]. Results for the isotropic validation tests were in most cases 100 % accurate when compared to the results of Abaqus standard C3D8 elements under similar loading. Passive and active test results were compared to those results found in Martins' work [88], and were found to behave similarly.

The results for the isometric and isotonic tests are comparable to the results found in Martins' work [88]. The displacement solution for these tests display similar results. The difference in the numerical results are due to the limitations imposed on the model, i.e. linear elasticity, small strain assumptions. Even with these limitations, the results and behaviour prove to be similar.

9.3 OSA simulation results

Factors which influence OSA are self-weight of soft-tissues under gravitational loading, low airway pressure and reduced muscle patency. The focus of this study was on the muscle activation, and muscle behaviour under gravitational loading. The model of the human tongue was subjected to loading conditions simulating gravity and muscle activation, but not airway pressure. These loading conditions were used to examine the behaviour of the model. Future models will incorporate airway pressure.

Gravitational forces were applied in the standing and supine positions in successive tests. The effect of individually activated muscle groups on the displacement of the tongue in the gravitational field were examined. It was found that the tongue displaced less in the gravitational field when any muscles were present, even when only passive. The muscle fibres provide an additional stiffness to the material, even without active contraction. The parameter T_0 affects stiffness of fibres passively, not just actively. With active contraction, the stress experienced by the material increases, and there is also a chance that the material will decrease in length along the muscle fibre direction, depending on the external, or body force applied to it.

Individual muscle groups had the following effects on displacement:

- The DG, GG, GH, HG, IL, and V muscle groups pull the tongue away from the back of the airway, reducing the potential for airway constriction and an OSA event.
  - It should be noted that due to imposing a fixed hyoid bone boundary condition, the DG muscle had only a small effect on pulling the tongue away from the back of the mouth, but it would reduce constriction even more with a floating hyoid bone.
- The T, SL, and MH muscle groups pull the tongue toward the back of the airway, increasing the potential for airway constriction and an OSA event.

9.4 Improving the model

This model was developed using small strain theory so as to focus on the development of the muscle fibres directionality and muscle activation. The model is also limited to linear elasticity, near-

incompressibity and quasi-static analyses. Selectively reduced integration was used in standard element types in Abaqus. The LMM UEL did not make use of selectively reduced integration, thus explaining a difference in bending behaviour. Future models will incorporate this feature.

For the modelling of biological soft-tissue to be realistic, large strain, non-linear elasticity theory should be used. Muscle fibre directions, muscle activation and incompressibility were accounted for in this model, but the model itself has to be expanded to the finite strain domain. A hyperelastic relationship will have to be formulated.

If large displacements are considered, there is the likelihood of contact occurring between the tongue and the surrounding soft-tissues. Contact modelling should be used to handle these implications. In addition, mesh refinement could increase the accuracy and precision of the results.

9.5 FSI model

CFD and FSI models for the airflow will have to be implemented to give a more realistic representation of the pressure patterns in the airway, and the effect on the movement of the soft tissues of the HUA.

Positron Emission Particle Tracking (PEPT) can be used to track radioactive particles moving in a defined area. Combining this particle tracking method with a rapid-prototype model of the human upper airway (HUA), a great deal can be learned from the fluid flow within it. This would give experimental validation for CFD simulations on the HUA.

9.6 Biological material testing

Physical testing of important material properties of the tissue of the tongue may have to be carried out. Various material parameters were taken from literature. More appropriate parameters can be extracted by performing specific and relevant tests on the biological materials concerned. An example of this would be biaxial tensile test data on skeletal muscle tissue.

9.7 EMG reading of muscles of the tongue

The values for muscle activation were taken from the works of Martins' et. al. on pelvic floor muscles [88]. These in turn were derived from earlier works by Pandy et. al. [106]. An accurate level of activation will have to be recorded for each muscle in the tongue in-vivo using electromyogram (EMG) readings. This is currently the only way to accurately measure the activation history of the muscles of the tongue.

9.8 Acquiring OSAS patient data

The data used for this study was from the VHP. The cadaver specimen used was not that of a person who fits the profile of a typical sleep apnea patient. This data was chosen, due to its high detail, especially the detail of muscle fibres. The lack of data on in vivo human testing is another reason for using this dataset. Actual OSA Patient geometry should be used for future work.

In addition, post-mortem deformation of the VHP cadaver needs to be taken into account. The amount of blood present in the tongue could affect its shape, and rigidity. DTI (diffusion tensor imaging) could be used to extract exact muscle fibre architecture from an OSA patient, providing a highly accurate dataset of the muscles fibres.

9.9 Muscle fibre management

Muscle fibre directions were defined on an elemental basis. This means that each element in the mesh has one fibre direction associated with it. It would be more accurate to have the muscle fibres defined at integration points. This way, each integration point has a specific fibre direction assigned to it. It should be noted that as mesh size, and hence element count increases, the elemental fibres and the fibres at the integration points tend to converge to similar values.

9.10 Contribution of this thesis

In summary, a complete working finite element model of the human tongue has been developed. The geometry of the tongue has been successfully captured from the VHP image dataset. In addition, muscle fibre orientations of the tongue have also been captured from this dataset. From this geometry, a finite element mesh has been generated. This finite element mesh, together with the muscle fibre data, have been used to simulate the human tongue under gravitational loading. With this model and the simulations completed, we were able to examine the behaviour of the human tongue in a simplified simulated case of OSA, where gravity is assumed to be the main contributor. From these simulations we have observed that activation of specific muscles in the tongue simultaneously leads to a reduction in constriction of the airway in this OSA case. Future models will incorporate airway pressure, which is another significant contributor to OSA. It was found that the T_0 muscle parameter affects the muscle model similarly to muscle tone in the tongue, which is also a contributing factor in OSA. EMG data for the human tongue has to be obtained in order to determine a more suitable level of activation, or muscle tone.

References

[1] S. Abd-El-Malek. Observations on the morphology of the human tongue. *Journal of Anatomy*, 73(2):201–210, 1939.

[2] M. Aigner and J. Heegaard. One-dimensional quasi-static continuum model of muscle contraction as a distributed control system. Technical report, Center for Turbulence Research, 1999.

[3] T. L. Allinger, W. Herzog, and M. Epstein. Force-length properties in stable skeletal muscle fibers - theoretical considerations. *Journal of Biomechanics*, 29(9):1235–1240, 1996.

[4] R. Arens, J. M. McDonough, A. T. Costarino, S. Mahoubi, C. E. Tayag-Kier, G. Maislin, R. J. Schwab, and A. I. Pack. Magnetic resonance imaging of the upper airway structure of children with obstructive sleep apnea syndrome. *American Journal of Respiratory and Critical Care Medicine*, 164:698–703, 2001.

[5] J. J. Armstrong, M. S. Leigh, D. D. Sampson, J. H. Walsh, D. R. Hillman, and P. R. Eastwood. Quantitative upper airway imaging with anatomic optical coherence tomography. *American Journal of Respiratory and Critical Care Medicine*, 173:226–233, 2006.

[6] L. A. Barness, J. M. Opitz, and E. Gilbert-Barness. Obesity: Genetic, molecular, and environmental aspects. *American Journal of Medical Genetics*, 143A(24):3016–3034, 2007.

[7] T. Belytschko, W. Kam Liu, and B. Moran. *Nonlinear Finite Elements for Continua and Structures*. J. Wiley and Sons, 2000.

[8] S. S. Blemker and S. L. Delp. Rectus femoris and vastus intermedius fiber excursions predicted by three-dimensional muscle models. *Journal of Biomechanics*, 39:1383–1391, 2006.

[9] S. S. Blemker, P. M. Pinsky, and S. L. Delp. A 3d model of muscle reveals the causes of nonuniform strains in the biceps brachii. *Journal of Biomechanics*, 38:657–665, 2005.

[10] S. S. Blemker, J. Teran, E. Sifakis, R. Fedkiw, and S. Delp. Fast 3d muscle simulations using a new quasistatic invertible finite-element algorithm. In *10th International Symposium on Computer Simulation in Biomechanics*, 2005.

[11] E. M. H. Bosboom, M. K. C. Hesselink, C. W. J. Oomens, C. V. C. Bouten, M. R. Drost, and F. P. Baaijens. Passive transverse mechanical properties of skeletal muscle under in vivo compression. *Journal of Biomechanics*, 34(10):1365–8, 2001.

[12] K. Bradshaw. Imaging the upper airways. *Paediatric Respiratory Reviews*, 2:46–56, 2001.

[13] A. J. Brady. The three element model of muscle mechanics: Its applicability to cardiac muscle. *The Physiologist*, 10:75–86, 1967.

[14] M. J. Brennick, S. Pickup, L. Dougherty, J. R. Cater, and S. T. Kuna. Pharyngeal airway wall mechanics by MRI with tissue tagging during medial hypoglossal nerve stimulation in rats. *Journal of Physiology*, 561(2):597–610, 2004.

[15] P. Caballero, R. Alvarez-Sala, F. García-Río, C. Prados, M.A. Hernán, J. Villamor, and J.L. Alvarez-Sala. CT in the evaluation of the upper airway in healthy subjects and in patients with obstructive sleep apnea syndrome. *CHEST*, 113:111–116, 1998.

[16] A. Cassar, T. I. Morgenthaler, R. J. Lennon, C. S. Rihal, and A. Lerman. Treatment of obstructive sleep apnea is associated with decreased cardiac death after percutaneous coronary intervention. *Journal of the American College of Cardiology*, 50(14):1310–1314, 2007.

[17] F. Chouly, A. Van Hirtum, P. Lagrée, X. Pelorson, and Y. Payan. Fluid-structure interaction in obstructive sleep apnea: Validation of numerical simulations using in-vitro measurements. *Journal of Biomechanics*, 39:S441, 2006.

[18] F. Chouly, A. Van Hirtum, P. Lagrée, X. Pelorson, and Y. Payan. Reproduction of hypopnea phenomenon using a physical and numerical model. In *Proceedings of the 6th International Symposium on Computer Methods in Biomechanics and Biomedical Engineering*, 2006.

[19] F. Chouly, A. Van Hirtum, P. Lagrtee, J. Paoli, X. Pelorson, and Y. Payan. *Simulation of the retroglossal fluid-structure interaction during obstructive sleep apnea*. Springer-Verlag Berlin Heidelberg, m. harders and g. székely edition, 2006.

[20] M. A. Ciscar, G. Juan, V. Martínez, M. Ramón, T. Lloret, J. Mínguez, M. Armengot, J. Marín, and J. Basterra. Magnetic resonance imaging of the pharynx in OSA patients and healthy subjects. *European Respiratory Journal*, 17:79–86, 2001.

[21] R. W. Clough. The finite element method in plane stress analysis. In *Proceedings of the ASCE Conference on Electronic Computation*, 1960.

[22] R. W. Clough. Thoughts about the origin of the finite element method. *Computers and Structures*, 79:2029–2030, 2001.

[23] G. K. Cole, A. J. van den Bogert, W. Herzog, and K. G. M. Gerritsen. Modelling of force production in skeletal muscle undergoing stretch. *Journal of Biomechanics*, 29(8):1091–1104, August 1996.

[24] Dassault Systèmes Simulia Corp.©. Abaqus®. Version 6.8, 2008. Rising Sun Mills, 166 Valley Street, Providence, RI 02909, USA.

[25] J. Dang and K. Honda. Estimation of vocal tract shapes from speech sounds with a physiological articulatory model. *Journal of Phonetics*, 30:511–532, 2002.

[26] Dassault Systèmes Simulia Corp.©. *Abaqus® User Documentation*, 6.8 edition, 2008.

[27] D. J. Dattilo and M. Aynechi. Modification of the anterior mandibular osteotomy for genioglossus advancement with hyoid suspension for obstructive sleep apnea. *Journal oral maxillofacial surgery*, 65:1876–1879, 2007.

[28] D. d'Aulignac, J. A. C. Martins, T. Mascarenhas, R. M. Natal Jorgez, and E. B. Pires. A shell finite element model of the pelvic floor muscles. *Computer Methods in Biomechanics and Biomedical Engineering*, 8(5):339–347, 2005.

[29] T. M. Davidson. Sleep medicine for surgeons. *Laryngoscope*, 118:915–931, 2008.

[30] N. J. Douglas. Upper airway imaging. *Clinical Physics and Physiological Measurement*, 11(A):117–119, 1990.

[31] O. Engwall. Modeling of the vocal tract in three dimensions. *Proceedings of Eurospeech*, 99:113–116, 1999.

[32] O. Engwall and P. Badin. Collecting and analysing two- and three-dimensional MRI data for swedish. *Journal of Biomechanics*, 40:11–38, 1999.

[33] M. A. Epstein and M. Stone. The tongue stops here: Ultrasound imaging of the palate. *Journal of the Acoustical Society of America*, 118:2128–2131, 2005.

[34] M. E. Farrugiaa, G. M. Bydderb, J. M. Francisc, and M. D. Robson. Magnetic resonance imaging of facial muscles. *Clinical Radiology*, 62:1078–1086, 2007.

[35] S. M. Felton, T. A. Gaige, T. G. Reese, V. J. Wedeen, and R. J. Gilbert. Mechanical basis for lingual deformation during the propulsive phase of swallowing as determined by phase-contrast magnetic resonance imaging. *Journal of Applied Physiology*, 103:255–265, 2007.

[36] J. Fish and T. Belytschko. *A First Course in Finite Elements*. Wiley, 2007.

[37] W. W. Flemons. Obstructive sleep apnea. *New England Journal of Medicine*, 347(7):498–504, 2002.

[38] P. J. Flory. Thermodynamic relations for high elastic materials. *Transactions of the Faraday Society*, 57:829–38, 1961.

[39] R. B. Fogel, A. Malhotra, G. Pillar, J. K. Edwards, J. Beauregard, S. A. Shea, and D. P. White. Genioglossal activation in patients with obstructive sleep apnea versus control subjects: mechanisms of muscle control. *American Journal of Respiratory and Critical Care Medicine*, 164:2025Ű2030, 2001.

[40] M. Forcinito, M. Epstein, and W. Herzog. A numerical study of the stiffness of a sarcomere. *Journal of Electromyography and Kinesiology*, 8:133–138, 1998.

[41] S. Fujita, J. Dang, N. Suzuki, and K. Honda. A computational tongue model and its applications. *Oral Science International*, 4(2):97–109, 2007.

[42] Y. C. Fung. *Biomechanics: Mechanical Properties of Living Tissues*. Springer, second edition, 1993.

[43] T. A. Gaige, T. Benner, R. Wangn, V. J. Wedeen, and R. J. Gilbert. Three dimensional myoarchitecture of the human tongue determined in vivo by diffusion tensor imaging with tractography. *Journal of Magnetic Resonance Imaging*, 26:654–661, 2007.

[44] J. M Gerard, R. Wilhelms-Tricarico, P. Perrier, and Y. Payan. A 3d dynamical biomechanical tongue model to study speech motor control. *Recent Research Developments in Biomechanics*, 1:49–64, 2003.

[45] R. J. Gibert, T. G. Reese, S. J. Daftary, R. N. Smith, R. M. Weisskoff, and V. J. Wedeen. Determination of lingual myoarchitecture in whole tissue by NMR imaging of anisotropic water diffusion. *American Journal of Physiology – Gastrointestinal and Liver Physiology*, 275:363–369, 1998.

[46] A. W. J. Gielen, P. H. M. Bovendeerd, and J. D. Janssen. *DIANA Computational Mechanics '94*, chapter A finite element formulation of muscle contraction, page 139Ű148. Springer-Verlag New York, 1994. Editors: G.M.A. Kusters and M.A.N. Hendriks.

[47] R. J. Gilbert and V. J. Napadow. Three-dimensional muscular architecture of the human tongue determined in vivo with diffusion tensor magnetic resonance imaging. *Dysphagia*, 20:1–7, 2005.

[48] R. J. Gilbert, V. J. Napadow, T. A. Gaige, and V. J. Wedeen. Anatomical basis of lingual hydrostatic deformation. *The Journal of Experimental Biology*, 210:4069–4082, 2007.

[49] A. M. Gordon, A. F. Huxley, and F. J. Julian. The variation in isometric tension with sarcomere length in vertebrate muscle fibres. *Journal of Physiology*, 184(1):170–192, 1966.

[50] A. P. Grieve and C. G. Armstrong. Compressive properties of soft tissues. In *Biomechanics XI-A, International Series on Biomechanics*, 1988.

[51] W. Herzog and R. Ait-Haddou. Considerations on muscle contraction. *Journal of Electromyography and Kinesiology*, 12:425–433, 2002.

[52] K. M. Hiiemae, J. B. Palmer, S. W. Medicis, J. Hegener, B. S. Jackson, and D. E. Lieberman. Hyoid and tongue surface movements in speaking and eating. *Archives of Oral Biology*, 47:11–27, 2002.

[53] A. V. Hill. The heat of shortening and the dynamic constants of muscle. *Proceedings of the Royal Society*, 126:136–195, 1938.

[54] A. Van Hirtum, F. Chouly, A. Teulťe, Y. Payan, and X. Pelorson. In-vitro study of pharyngeal pressure losses at the origin of obstructive sleep apnea. *Engineering in Medicine and Biology Society*, 1:17–21, 2003.

[55] G. A. Holzapfel. *Nonlinear Solid Mechanics: A Continuum Approach for Engineering*. John Wiley & Sons, 2000.

[56] G. A. Holzapfel, R. Eberleinb, P. Wriggersb, and H. W. Weizsticker. Large strain analysis of soft biological membranes: Formulation and finite element analysis. *Computational Methods in Applied Mechanics and Engineering*, 132:45–61, 1996.

[57] L. Huang and J. E. F. Williams. Neuromechanical interaction in human snoring and upper airway obstruction. *Journal of Applied Physiology*, 86:1759–1763, 1999.

[58] Y. Huang, A. Malhotra, and D. P. White. Computational simulation of human upper airway collapse using a pressure-/state-dependent model of genioglossal muscle contraction under laminar flow conditions. *Journal of Applied Physiology*, 99:1138–1148, 2005.

[59] Y. Huang, D. P. White, and A. Malhotra. The impact of anatomic manipulations on pharyngeal collapse: results from a computational model of the normal human upper airway. *Chest*, 128(3):1324–1330, September 2005.

[60] Y. Huang, D. P. White, and A. Malhotra. Use of computational modeling to predict responses to upper airway surgery in obstructive sleep apnea. *Laryngoscope*, 117:648–653, 2007.

[61] T. J. R. Hughes. *The Finite Element Method: Linear Static and Dynamic Finite Element Analysis*. Prentice-Hall, 2000.

[62] J. D. Humphrey. *Cardiovascular Solid Mechanics - Cells, Tissues, and Organs*. Springer-Verlag New York, Inc., 2002.

[63] J. D. Humphrey, R. K. Strumpf, and F. C. P. Yin. Determination of a constitutive relation for passive myocardium: a new functional form. *Journal of Biomechanical Engineering*, 112:333–339, 1990.

[64] J. D. Humphrey and F. C. Yin. Constitutive relations and finite deformations of passive cardiac tissue ii: stress analysis in the left ventricle. *Circulation Research*, 65:805–817, 1989.

[65] J. D. Humphrey and F. C. P. Yin. On constitutive relations and finite deformations of passive cardiac tissue: I. a pseudostrain-energy function. *Journal of Biomechanical Engineering*, 109:298–304, 1987.

[66] A. F. Huxley. Muscle structure and theories of contraction. *Progress in Biophysics and Biophysical Chemistry*, 7:257–318, 1957.

[67] Kitware Inc. and Los Alamos National Laboratory. Paraview. Open-Source, 2000.

[68] S. Ishikawa, T. Nakayama, M. Watanabe, and T. Matsuzawa. Visualization of flow resistance in physiological nasal respiration. *Archives of Otolaryngology–Head and Neck Surgery*, 132:1203–1209, 2006.

[69] S. Jeong, W. Kim, and S. Sung. Numerical investigation on the flow characteristics and aerodynamic force of the upper airway of patient with obstructive sleep apnea using computational fluid dynamics. *Medical Engineering and Physics*, 29(6):637–651, 2007.

[70] A. S. Jordan, A. Wellman, J. K. Edwards, K. Schory, L. Dover, M. MacDonald, S. R. Patel, R. B. Fogel, A. Malhotra, and D. P. White. Respiratory control stability and upper airway collapsibility in men and women with obstructive sleep apnea. *Journal of Applied Physiology*, 99:2020–2027, 2005.

[71] G. C. Joyce and P. M. H. Rack. Isotonic lengthening and shortening movements of cat soleus muscle. *Journal of Physiology*, 204:475 – 491, 1969.

[72] G. C. Joyce, P. M. H. Rack, and D. R. Westbury. The mechanical properties of cat soleus muscle during controlled lengthening and shortening movements. *Journal of Physiology*, 204:461–474, 1969.

[73] K. Keyhani, P. W. Scherer, and M. M. Mozell. A numerical model of nasal odorant transport for the analysis of human olfaction. *Journal Theoretical Biology*, 186:168–290, 1997.

[74] M. Kojic, S. Mijailovic, and N. Zdravkovic. Modelling of muscle behaviour by the finite element method using hill's three-element model. *International Journal for Numerical Methods in Engineering*, 43:941–953, 1998.

[75] S. H. Kyung, Y. Park, and E. Pae. Obstructive sleep apnea patients with the oral appliance experience pharyngeal size and shape changes in three dimensions. *The Angle Orthodontist*, 75(1):15–22, 2004.

[76] W. Michael Lai, D. Rubin, E. Krempl, D. Rubin, and E. Krempl. *Introduction to Continuum Mechanics*. Elsevier Science Technology Books, 1996.

[77] W. Li, M. Perzl, G. A. Ferron, R. Batycky, J. Heyder, and D. A. Edwards. The macrotransport properties of aerosol particles in the human oral-pharyngeal region. *Journal of Aerosol Science*, 29(8):995–1010, 1998.

[78] W. Li, M. Perzl, R. Langer, J. D. Brain, K.-H. Engelmeier, R. Niven, and D. A. Edwards. Aerodynamics and aerosol particle deaggregation phenomena in model oral-pharyngeal cavities. *Journal of Aerosol Science*, 27(8):1269–1286, 1996.

[79] X. Liu, M. Stone, and J. Prince. Tracking tongue motion in three dimensions using tagged MRI. *Proceedings of the* IEEE ISBI, 1:1372–1375, 2006.

[80] X. Y. Luo, J. S. Hinton, T. T. Liew, and K. K. Tan. Les modelling of flow in a simple airway model. *Medical Engineering & Physics*, 26:403–413, 2004.

[81] L. Magnusson. Three dimensional mapping of lingual myoarchitecture. Master's thesis, Massachusetts institute of technology, 2005.

[82] A. Malhotra, R. B. Fogel, J. K. Edwards, S. A. Shea, and D. P. White. Local mechanisms drive genioglossus activation in obstructive sleep apnea. *American Journal of Respiratory and Critical Care Medicine*, 161:1746–1749, 2000.

[83] A. Malhotra, Y. Huang, R. B. Fogel, G. Pillar, J. K. Edwards, R. Kikinis, S. H. Loring, and D. P. White. The male predisposition to pharyngeal collapse: importance of airway length. *American Journal of Respiratory and Critical Care Medicine*, 166:1388–1395, 2002.

[84] A. Malhotra, G. Pillar, R. B. Fogel, J. Beauregard, J. K. Edwards, D. I. Slamowitz, S. A. Shea, and D. P. White. Genioglossal but not palatal muscle activity relates closely to pharyngeal pressure. *American Journal of Respiratory and Critical Care Medicine*, 162:1058–1062, 2000.

[85] A. Malhotra, G. Pillar, R. B. Fogel, J. K. Edwards, N. Ayas, T. Akahoshi, D. Hess, and D. P. White. Pharyngeal pressure and flow effects on genioglossus activation in normal subjects. *American Journal of Respiratory and Critical Care Medicine*, 165:71–77, 2002.

[86] A. Malhotra and D. P. White. Obstructive sleep apnoea. *The Lancet*, 360:237–245, July 2002.

[87] L. E. Malvern. *Introduction to the Mechanics of a Continuous Medium.* Prentice-Hall, 1997.

[88] J. A. C. Martins, M. P. M. Pato, and E. B. Pires. A finite element model of skeletal muscles. *Virtual and Physical Prototyping*, 1(3):159–170, September 2006.

[89] J. A. C. Martins, E. B. Pires, R. Salvado, and P. B. Dinis. A numerical model of passive and active behaviour of skeletal muscles. *Computer Methods in Applied Mechanics and Engineering*, 151:419–433, 1998.

[90] T. B. Martonen, Z. Zhang, G. Yue, and C. J. Musante. 3-d particle transport within the human upper respiratory tract. *Aerosol science*, 33:1095–1110, 2002.

[91] The Mathworks. MATLAB ®. R2007a, 2007.

[92] F. Medina and R. B. Wicker. Geometric modeling of the human aorta for rapid prototyping using patient data and commercial software packages. In *Summer Bioengineering Conference*, pages 25–29, University of Texas at El Paso, El Paso, Texas 79968-0521, June 2003. W.M. Keck Border Biomedical Manufacturing and Engineering Laboratory.

[93] M. Mihaescu, S. Murugappan, E. Gutmark, L. F. Donnelly, and M. Kalra. Computational modeling of upper airway before and after adenotonsillectomy for obstructive sleep apnea. *Laryngoscope*, 118:360–362, 2008.

[94] N. Mohsenin, M. T. Mostofi, and V. Mohsenin. The role of oral appliances in treating sleep apnea. *Journal American Dental Association*, 134:442–449, 2003.

[95] H. Moriwaki, Y. Inoue, K. Namba, Y. Suto, S. Chiba, and H. Moriyama. Clinical significance of upper airway obstruction pattern during apeic episodes on ultrafast dynamic magnetic resonance imaging. *Auris Nasus Larynx*, 36(2):187–191, 2009.

[96] A. T. Mulgrew, C. F. Ryan, J. A. Fleetham, R. Cheema, N. Fox, M. Koehoorn, J. M. FitzGerald, C. Marra, and N. T. Ayas. The impact of obstructive sleep apnea and daytime sleepiness on work limitation. *Sleep Medicine*, 9(1):42–53, 2007.

[97] V. J. Napadow, Q. Chen, V. Mai, P. T. C. So, and R. J. Gilbert. Quantitative analysis of three-dimensional-resolved fiber architecture in heterogeneous skeletal muscle tissue using NMR and optical imaging methods. *Biophysical Journal*, 80(6):2968–2975, 2001.

[98] V. J. Napadow, Q. Chen, V. J. Wedeen, and R. J. Gilbert. Intramural mechanics of the human tongue in association with physiological deformations. *Journal of Biomechanics*, 32:1–12, 1999.

[99] F. Netter. *The Netter Presenter ^{TM}Human Anatomy Collection.* Icon learning systems, 2003.

[100] Materialise NV. Mimics ®. Version 12.1, 2008. Leuven, Belgium.

[101] C. M. O'Connor. Design of surface electrode array for measuring conduction velocity in the human genioglossus muscle. *IEEE transactions on Biomedical Engineering*, 54(2):335–339, 2007.

[102] U.S. National Library of Medicine. The visible human project ®. http://www.nlm.nih.gov/research/visible, September 2009.

[103] T. Ono, A. A. Lowe, K. A. Ferguson, E. Pae, and J. A. Fleetham. The effect of the tongue retaining device on awake genioglossus muscle activity in patients with obstructive sleep apnea. *American Journal of Orthodontics and Dentofacial Orthopedics*, 110(1):28–35, July 1996.

[104] E. T. Ooi, S. Rajendran, J. H. Yeo, and B. R. Zhang. A mesh distortion tolerant 8-node solid element based on the partition of unity method with inter-element compatibility and completeness properties. *Finite Elements in Analysis and Design*, 43:771–787, 2007.

[105] C. W. Oomens, M. Maenhout, C. H. van Oijen, M. R. Drost, and F. P. Baaijens. Finite element modelling of contracting skeletal muscle. *Philosophical Transactions of the Royal Society B: Biological Sciences*, 358(1437):1453–60, 2003.

[106] M. G. Pandy, F. E. Zajac, E. Sim, and W. S. Levine. An optimal control model for maximum-height human jumping. *Journal of Biomechanics*, 23(12):1185–1198, 1990.

[107] U.S. Patent. System and method for x-ray fluoroscopic imaging cross references to related applications. *U.S. Patent*, -(09/990,880), 2001.

[108] G. Pillar, A. Malhotra, R. Fogel, J. Beauregard, R. Schnall, and D. P. White. Airway mechanics and ventilation in response to resistive loading during sleep: influence of gender. *American Journal of Respiratory and Critical Care Medicine*, 162:1627–1632, 2000.

[109] M. A Puhan, A. Suarez, C. Lo Cascio, A. Zahn, M. Heitz, and O. Braendli. Didgeridoo playing as alternative treatment for obstructive sleep apnoea syndrome: randomised controlled trial. *Biomedical Journal*, 332:266–270, 2006.

[110] K. Puvanendran and K. L. Goh. From snoring to sleep apnea in a singapore population. *Sleep Research Online*, 2(1):11–19, 1999.

[111] C. M. Ryan and T. D. Bradley. Pathogenesis of obstructive sleep apnea. *Journal of Applied Physiology*, 99:2440–2450, 2005.

[112] J. P. Saboisky, J. E. Butler, D. K. McKenzie, R. B. Gorman, J. A. Trinder, D. P.White, and S. C. Gandevia. Neural drive to human genioglossus in obstructive sleep apnoea. *Journal of Physiology*, 585:135–146, 2007.

[113] M. S. Sacks and W. Sun. Multiaxial mechanical behavior of biological materials. *Annu. Rev. Biomed. Eng.*, 5:251–84, 2003.

[114] H. Saito and I. Itoh. Three-dimensional architecture of the intrinsic tongue muscles, particularly the longitudinal muscle, by the chemical-maceration method. *Anatomical Science International*, 78:168–176, 2003.

[115] B. Shivalkar, C. Van De Heyning, M. Kerremans, D. Rinkevich, J. Verbraecken, W. De Backer, and C. Vrints. Obstructive sleep apnea syndrome. *Journal of the American College of Cardiology*, 47(7):1433–1439, 2006.

[116] J. C. Simo. *Topics on the numerical analysis and simulation of plasticity*, volume VI of Handbook of numerical analysis. Elsevier Science Publishers B.V. (North Holand), 1998.

[117] J. C. Simo and T. J. Hughes. *Computational Inelasticity*. Springer Verlag, 2000.

[118] J. C. Simo and R. L. Taylor. Quasi-incompressible finite elasticity in principal stretches. continuum basis and numerical algorithms. *Computer Methods in Applied Mechanics and Engineering*, 85(3):273–310, 1991.

[119] Vancouver Sleep and Breathing Center http://www.sleep breathing.bc.ca. Accessed: 02/06/2008.

[120] A. J. M. Spencer. Constitutive theory for strongly anisotropic solids. In *Continuum Theory of the Mechanics of Fiber-reinforced Composites. CISM Courses and Lectures*, volume 282, pages 1–32. Springer, Wien, 1984.

[121] M. L. Stanchina, A. Malhotra, R. B. Fogel, N. Ayas, J. K. Edwards, K. Schory, and D. P. White. Genioglossus muscle responsiveness to chemical and mechanical stimuli during nonŰrapid eye movement sleep. *American Journal of Respiratory and Critical Care Medicine*, 165:945Ű949, 2002.

[122] S. Sung, S. Jeong, Y. Yu, C. Hwang, and E. Pae. Customized three-dimensional computational fluid dynamics simulation of the upper airway of obstructive sleep apnea. *Angle Orthodontist*, 76(5):791–799, 2006.

[123] H. Takemoto. Morphological analyses of the human tongue musculature for three-dimensional modeling. *Journal of Speech, Language, and Hearing Research*, 44:65–107, 2001.

[124] American Sleep Apnea Association (ASAA). www.sleepapnea.org, 2008. 6856 Eastern Avenue, NW, Suite 203, Washington, DC 20012.

[125] Parametric Technology Corporation (PTC). Pro-engineer ®. Wildfire 2.0, 2007. Needham, Massachusetts, USA.

[126] G. J. Tortora and S. R. Grabowski. *Principles of Anatomy and Physiology*. Harper Collins College Publishers, eighth edition, 1996.

[127] A. J. Van den Bogert, K. G. M. Gerritsen, and G. K. Cole. Human muscle modelling from a user's perspective. *Journal of Electromyography and Kinesiology*, 8(2):119–124, April 1998.

[128] M. Van Loocke, C.G. Lyons, and C. Simms. *Topics in bio-mechanical engineering*, chapter VIII: The three-dimensional mechanical properties of skeletal muscle: experiments and modelling, pages 216–234. Dublin & Galway, 2007.

[129] M. Van Loocke, C.G. Lyons, and C.K. Simms. A validated model of passive muscle in compression. *Journal of Biomechanics*, 39:2999–3009, 2006.

[130] M. Van Loocke, C.G. Lyons, and C.K. Simms. Viscoelastic properties of passive skeletal muscle in compression: Stress-relaxation behaviour and constitutive modelling. *Journal of Biomechanics*, 41:1555–1566, 2008.

[131] F. Vogt. Finite element modeling of the tongue. In *Conference on Auditory and Visual Speech Processing*, 2005.

[132] W. Vos, J. De Backer, A. Devolder, O. Vanderveken, S. Verhulst, R. Salgado, P. Germonpre, B. Partoens, F. Wuyts, P. Parizel, and W. De Backer. Correlation between severity of sleep apnea and upper airway morphology based on advanced anatomical and functional imaging. *Journal of Biomechanics*, 40:2207–2213, 2006.

[133] J. H. Walsh, M. S. Leigh, A. Paduch, K. J. Maddison, D. L. Philppi, J. J. Armastrong, D. D. Sampson, D. R. Hillman, and P. R. Eeastwood. Evaluation of pharyngeal shape and size using anatomical optical coherence tomography in individuals with and without obstructive sleep apnoea. *Journal of Sleep Research*, 17(2):230–238, 2008.

[134] I. Weinhold and G. Mlynski. Numerical simulation of airflow in the human nose. *European Archives of Oto-Rhino-Laryngology*, 261:452–455, 2004.

[135] J. A. Weiss, B. N. Makerc, and S. Govindjee. Finite element implementation of incompressible, transversely isotropic hyperelasticity. *Computer Methods in Applied Mechanics and Engineering*, 135:107–128, 1996.

[136] R. Wilhelms-Tricarico. Physiological modeling of speech production: Methods for modeling soft-tissue articulators. *Journal Acoustical Society America*, 97(5):3085–3098, 1995.

[137] R. Wilhelms-Tricarico. A biomechanical and physiologically-based vocal tract model and its control. *Journal of Phonetics*, 24:23–28, 1996.

[138] J. Z. Wu, W. Herzog, and G. K. Cole. Modeling dynamic contraction of muscle using the cross-bridge theory. *Mathematical Biosciences*, 139:69–78, 1997.

[139] M. C. Wu, J. C. Han, O. Röhrle, W. Thorpe, and P. Nielsen. Using three-dimensional finite element models and principles of active muscle contraction to analyse the movement of the tongue. In *Australian International Conference on Speech Science and Technology*, 2006.

[140] C. Xu, S. Sin, J. M. McDonough, J. K. Udupa, A. Guez, R.Arens, and D. M. Wootton. Computational fluid dynamics modeling of the upper airway of children with obstructive sleep apnea syndrome in steady flow. *Journal of Biomechanics*, 39:2043–2054, 2006.

[141] G. I. Zahalak. Non-axial muscle stress and stiffness. *Jounal of Theoretical Biology*, 182:59–84, 1996.

[142] G. I. Zahalak and S. Ma. Muscle activation and contraction: constitutive relations based directly on cross-bridge kinetics. *Journal of Biomechanical Engineering*, 112:52–62, February 1990.

[143] F. E. Zajac. Muscle and tendon: properties, models, scaling, and application to biomechanics and motor control. *Critical Reviews in Biomedical Engineering*, 17(4):359–411, 1989.

[144] R. Zeng, J. A. Fessler, and J. M. Balter. Estimating 3–dimensional respiratory motion from orbiting views by tomographic image registration. *IEEE transactions on Medical Imaging*, 26(2):153–163, 2007.

[145] K. Zhao, P. W. Scherer, S. A. Hajiloo, and P. Dalton. Effect of anatomy on human nasal air flow and odorant transport patterns: implications for olfaction. *Chemical Senses*, 29(5):365–379, 2004.

[146] X. Zhao, Y. Liu, and Y. Gaoc. Three-dimensional upper-airway changes associated with various amounts of mandibular advancement in awake apnea patients. *American Journal of Orthodontics and Dentofacial Orthopedics*, 133:661–668, 2008.

[147] O.C. Zienkiewicz. *The Finite Element Method*. McGraw-Hill Book Company (UK) Limited, 3 edition, 1977.

[148] M. A. Zulliger, A. Rachev, and N. Stergiopulos. A constitutive formulation of arterial mechanics including vascular smooth muscle tone. *American Journal Physiology - Heart and Circulation Physiology*, 287(3):1335–1343, September 2004.